

American University in Cairo

AUC Knowledge Fountain

Theses and Dissertations

Student Research

Winter 1-31-2021

A Computational Study of CoCrFeNiTi High Entropy Alloys: Phase Diagrams, Thermodynamics, and Mechanical Properties from CALPHAD and First Principles

Geraldine Anis
girawael@aucegypt.edu

Follow this and additional works at: <https://fount.aucegypt.edu/etds>



Part of the [Engineering Science and Materials Commons](#)

Recommended Citation

APA Citation

Anis, G. (2021). *A Computational Study of CoCrFeNiTi High Entropy Alloys: Phase Diagrams, Thermodynamics, and Mechanical Properties from CALPHAD and First Principles* [Master's Thesis, the American University in Cairo]. AUC Knowledge Fountain.

<https://fount.aucegypt.edu/etds/1515>

MLA Citation

Anis, Geraldine. *A Computational Study of CoCrFeNiTi High Entropy Alloys: Phase Diagrams, Thermodynamics, and Mechanical Properties from CALPHAD and First Principles*. 2021. American University in Cairo, Master's Thesis. *AUC Knowledge Fountain*.

<https://fount.aucegypt.edu/etds/1515>

This Master's Thesis is brought to you for free and open access by the Student Research at AUC Knowledge Fountain. It has been accepted for inclusion in Theses and Dissertations by an authorized administrator of AUC Knowledge Fountain. For more information, please contact thesisadmin@aucegypt.edu.

A Computational Study of CoCrFeNiTi High Entropy Alloys:
Phase Diagrams, Thermodynamics, and Mechanical Properties
from CALPHAD and First Principles

By

Geraldine Anis

B.Sc. Mechanical Engineering, AUC

A thesis submitted in partial fulfillment of the requirements for the degree of
Master of Science in Nanotechnology

Supervisor

Dr. Hanadi Salem

Professor of Materials & Manufacturing
Department of Mechanical Engineering,
The American University in Cairo

Co-Advisor

Dr. Mostafa Youssef

Assistant Professor of Computational Materials Science and Engineering
Department of Mechanical Engineering
The American University in Cairo

External Co-Advisor

Dr. Moataz Attallah

Professor of Advanced Materials Processing
University of Birmingham, UK

Acknowledgements

First, I would like to express my extreme gratitude to God for the privilege of pursuing this degree. This experience has transformed me, and I am grateful to have been given this opportunity to grow and learn. I am especially thankful to have made it here despite the difficult and stressful circumstances imposed on us by the Covid-19 pandemic. This has been a hectic and worrisome experience and at times, it seemed like it was impossible to make it, but God gave me the strength to persevere.

I would like to thank Dr. Hanadi Salem for helping me start this journey and for all the support she has given me throughout the years I have worked with her. Dr. Hanadi has been a true mentor and has guided me through multiple stages of my academic journey, which have led to where I am today. I am truly grateful for all the knowledge, motivation, and encouragement you have offered me. Dr. Hanadi, I will continue to apply everything you have taught me as I take my next steps in academia and will always cherish everything you have done for me.

I would also like to extend a special thanks to Dr. Mostafa Youssef. Your continuous support has been extremely encouraging and motivating. You have helped me navigate the world of computational materials science as a complete beginner up to being able to complete this project. I am particularly thankful for your time and effort throughout the Covid-19 pandemic, which has made it possible to complete my MSc thesis project in a timely manner during these especially difficult times. Thank you for everything.

I would like to thank Dr. Moataz Attallah for introducing me to this interesting project. This has been an incredible learning experience and has afforded me the opportunity to vastly expand my knowledge. Thank you for all your help and technical expertise, which has helped shape the scope of this project to be interesting and relevant.

Thank you to all the organizations, research groups, and individuals who have helped secure any resources needed to complete this work. Thank you for your prompt cooperation, which has greatly facilitated the completion of this project.

Finally, to my dearest parents, Wael and Myriam and my sister Joy, thank you for everything you have endured. You have been with me since the start of this journey and have supported me in every step. Words cannot express my gratitude. You have always pushed me to be the best that I can in all aspects of life, and it has shaped me into the person I am today. To Jan, thank you for always being there. Your unconditional support is a major part of why I was able to persevere and finally make it. Thank you to all the wonderful friends who have helped me along the way and a special thanks to George, Amira, and Jaylan, who has additionally provided continuous technical help and support.

Abstract

High entropy alloys (HEAs) are multi-component alloys, which are often defined as those consisting of at least 5 principal elements with concentrations ranging between 5 and 35 atomic weight percent (at.%). Since their introduction by Yeh et al. and Cantor et al. in 2004, HEAs have been found to possess many important properties and have become prime candidates for several high-performance applications such as high-temperature and biomedical applications. Despite their multi-principal element nature, many HEAs favor the formation of solid solution phases as opposed to the intermetallic phases expected for such systems. This was originally only attributed to their high configurational entropy. However, as more studies emerged, it became evident that the stabilization of solid solution phases in HEAs is contingent on many interdependent factors in addition to configurational entropy. One of the main obstacles that hinder HEA research is the vast compositional space available for a given HEA system, especially when non-equiatomic compositions are considered. For that reason, computational methods such as the calculation of phase diagrams (CALPHAD) have become central to the HEA field as they allow the efficient exploration of this massive search space.

In the present work, a systematic framework for pinpointing single-phase HEAs and studying their properties from first principles was developed. First, the CALPHAD method was used to construct extensive phase diagrams of four CoCrFeNiTi sub-systems, namely $\text{Co}_x\text{CrFeNiTi}_{2-x}$, $\text{CoCr}_x\text{FeNiTi}_{2-x}$, $\text{CoCrFe}_x\text{NiTi}_{2-x}$, and $\text{CoCrFeNi}_x\text{Ti}_{2-x}$. CALPHAD was also used to calculate several thermodynamic quantities, including the mixing enthalpies and entropies of the alloys, which were related to the phase stabilities obtained in the phase diagrams. In all our analyses, a special focus was placed on the single face-centered cubic (FCC) solid solution phase and the different factors that underly its stabilization. From the generated phase diagrams, an alloy with the composition $\text{CoCrFeNi}_{1.75}\text{Ti}_{0.25}$ and single-phase FCC structure was selected for a computational characterization of its mechanical properties.

A special quasirandom structure (SQS), which facilitates the modeling of random alloys, was used for studying the $\text{CoCrFeNi}_{1.75}\text{Ti}_{0.25}$ alloy. An 80-atom $5 \times 2 \times 2$ FCC supercell was generated, and first principles density functional theory (DFT) calculations were used to determine its mechanical properties. Computational tensile stress-strain diagrams were computed for the alloy SQS as well as its individual constituent elements their ideal tensile strengths were determined. An analysis of the alloy and element elastic constants was also carried out using DFT. The determined elastic constants were used to calculate the bulk, shear, and Young's modulus as well as the Poisson's ratio. The calculated element properties were compared to available experimental data and were used to benchmark the methods and analysis techniques employed. The calculated properties of the alloy SQS were compared to their corresponding weighted elemental averages. The coupled CALPHAD-DFT approach adopted in this work provides a methodical study of the phase stabilities and mechanical properties of non-equiatomic CoCrFeNiTi HEAs. The developed framework can also be extended to other HEA systems.

Table of Contents

Acknowledgements.....	i
Abstract.....	ii
Table of Contents.....	iii
List of Figures.....	v
List of Tables.....	viii
List of Abbreviations.....	ix
List of Symbols.....	xi
Chapter 1. Introduction.....	1
Chapter 2. Background and Thermodynamic Theory of Alloys.....	4
2.1. Phase Diagrams.....	4
2.1.1. Phases and Microstructures.....	4
2.2. Thermodynamics of Alloys and Solid Solutions.....	6
2.2.1. Definitions of the Gibbs Free Energy, Enthalpy, and Entropy.....	6
2.2.2. Mixing.....	7
Chapter 3. Literature Review.....	10
3.1. Overview of High Entropy Alloys.....	10
3.1.1. The Significance of HEAs and the Four Core Effects.....	11
3.1.2. Current Definitions of HEAs.....	13
3.2. Alloy Design.....	14
3.2.2. The Calculation of Phase Diagrams (CALPHAD) Method.....	21
3.3. The CoCrFeNiTi System.....	29
3.3.1. Dendritic Microstructures, Elemental Segregation, and Anisotropic Properties....	29
3.3.2. Intermetallic Phases in the CoCrFeNiTi System.....	30
3.3.3. Computational Phase Diagrams of the CoCrFeNiTi System.....	37
3.4. HEA Properties from First Principles.....	39
3.4.1. Special Quasirandom Structures (SQSs).....	39
3.4.2. Current State of HEA SQS First Principles Studies.....	40
3.5. Research Aims and Objectives.....	44
Chapter 4. Computational Methods.....	45
4.1. CALPHAD.....	45
4.1.1. Single-Point Calculations in OpenCalphad.....	45

4.1.2.	Phase Diagram Construction.....	47
4.1.3.	Thermodynamic Calculations	50
4.2.	Density Functional Theory (DFT).....	51
4.2.1.	DFT Setup.....	51
4.2.2.	Alloy Formation Enthalpy, Lattice Distortion, and Magnetism	54
4.2.3.	Mechanical Properties.....	54
Chapter 5.	Results and Discussion	57
5.1.	Phase Diagrams and Computational Thermodynamics	57
5.1.1.	Computational Phase Diagrams of the CoCrFeNiTi System.....	57
5.1.2.	Thermodynamic Analysis	64
5.2.	First Principles Properties	74
5.2.1.	Relaxed Lattice Constants.....	74
5.2.2.	Computational Stress-Strain, Young's Modulus, and Poisson's Ratio.....	75
5.2.3.	Elastic Constants Analysis.....	78
5.2.4.	Other HEA Properties from the CoCrFeNi _{1.75} Ti _{0.25} SQS.....	79
Chapter 6.	Conclusions and Future Work	83
6.1.	Conclusions	83
6.1.1.	Computational Phase Diagrams.....	83
6.1.2.	Thermodynamic Property Calculation.....	83
6.1.3.	First Principles Alloy Properties.....	84
6.2.	Recommendations and Future Work.....	85
References	87
Appendix A:	CALPHAD Files	A1
Appendix B:	Phase Diagram Construction	B1
Appendix C:	Raw Output.....	C1
Appendix D:	Density Functional Theory Data	D1

List of Figures

Fig. 2.1.1. A comparison of a substitutional solid solution (SSS) to an interstitial solid solution (ISS) [21].	5
Fig. 2.1.2. Comparing the structures of solid solutions to that of an intermetallic compound [24].	5
Fig. 2.1.3. Possible structures that result from mixing three elements: Single solid solution structure with random mixing; Mixed solid solution (random) and intermetallic compound (ordered); Multiple solid solutions with random mixing in each; Solid solution with spinodal decomposition (phase separation) [8].	6
Fig. 3.1.1. (a) The number of publications per year on high entropy materials (HEMs) (b) The number of citations per year for HEM papers since between 2004 and 2017 [3].	10
Fig. 3.1.2. The number of publications per year on high entropy alloys (HEAs) between 2004 and 2015 [36].	10
Fig. 3.1.3. (a) An example of a lattice in a 10-element system. The nearest neighbors of a given atom mostly consist of different elements. (b) A comparison between a BCC unit cell for a 1-element system and a 5-element system illustrating the resulting lattice distortion on varying the elements and its effect on the unit cell structure [38].	12
Fig. 3.1.4. (a) ΔG_{mix} vs. T of a $\text{Pt}_{0.5}\text{-Ru}_{0.5}$ binary alloy with an increasing slope for $-\text{T}\Delta S_{\text{vib}}$ indicating it destabilizes the solid solution phase (b) a convex hull plot for the Pt-Ru alloy system (c) ΔG_{mix} vs. T of a $\text{Ni}_{0.5}\text{-Cu}_{0.5}$ binary alloy also with a destabilizing $-\text{T}\Delta S_{\text{vib}}$ contribution (d) ΔG_{mix} vs. T of a $\text{Ni}_{0.5}\text{-Rh}_{0.5}$ binary alloy with a decreasing slope for $-\text{T}\Delta S_{\text{vib}}$ indicating it stabilizes the solid solution phase [40].	14
Fig. 3.2.1. Structural dependence on ΔH_{mix} and δ for (a) as cast [41] and (b) annealed HEAs [51]	21
Fig. 3.2.2. Thermodynamic database development and optimization process [59].	24
Fig. 3.2.3. Preferential occupation of the body-center and corner sublattice sites in a sublattice phase with a BCC structure [23].	26
Fig. 3.2.4. The Gibbs energy reference surface for a $(\text{A,B})_a(\text{C,D})_b$ reciprocal solution phase. The composition space is the square defined by the endmember AC, AD, BC, and BD [65].	28
Fig. 3.3.1. SEM microstructure image of as-cast (a) CoCrFeNiTi_0 (ie. CoCrFeNi) [9] and (b) SEM microstructure image of $\text{CoCrFeNiTi}_{0.3}$ showing the alloy's dendritic microstructure. The dendritic region is labeled as D and the interdendrite as ID [17].	30
Fig. 3.3.2. The crystal structures of some geometrically close-packed (GCP) phases of the A_3B type. Each structure is labeled with its Strukturbericht designation and its prototype phase. The white circles correspond to the Ni atoms in the prototype phase, while the black circles correspond to the phase's other element [73].	36
Fig. 3.3.3. Partial phase diagram of the $\text{Al}_x\text{Co}_{1.5}\text{CrFeNi}_{1.5}\text{Ti}_y$ ($x + y = 0.5$) system produced by Thermo-Calc and the TCNI5 database [77].	38
Fig. 3.3.4. Phase amounts calculated using CALPHAD for a $\text{CoCrFeNiTi}_{0.4}$ HEA using the JMatPro software and the TTNi8 database [79].	38

Fig. 3.3.5. Partial computational phase diagram of the CoCrFeNiTi _x HEA system, where x is the mole fraction of Ti. The diagram covers the region of the system from 0 (ie. equiatomic CoCrFeNi) to 0.15 mole fraction Ti and 750°C – 1500 °C [65].	39
Fig. 3.4.1. Vibrational and electronic entropies and Helmholtz vibrational and electronic free energies of mixing for 64-atom FCC CoCrFeNi; BCC MoNbTaW; and HCP CoOsReRu alloy SQSs [83].	42
Fig. 3.4.2. The procedure used for calculating the elastic constants and moduli of a give structure using the ElaStic package [90].	43
Fig. 4.1.1. Output obtained from an OpenCalphad single-point equilibrium calculation for a CoCrFeNi _{1.75} Ti _{0.25} alloy at 1500 K. The red boxes highlight the different types of data available pertaining to the equilibrium state of the system. These are: general system information; system component information; and phase equilibrium information.	46
Fig. 4.1.2. The CoCrFeNi _x Ti _{2-x} phase diagram produced by (a) the MAP function in OpenCalphad (b) the approach developed in the present study. This is the raw data output from the process, where each color represents an equilibrium phase combination (b) using an image processing software to trace and label the different phase regions.	48
Fig. 4.1.3. Sample of the compiled output from the CoCrFeNi _x Ti _{2-x} automated calculations.	49
Fig. 4.2.1. Visualization of the generated CoCrFeNi _{1.75} Ti _{0.25} SQS	53
Fig. 5.1.1. The CoCrFeNi _x Ti _{2-x} computational phase diagram generated by the CALPHAD method. The values of x range from 1 to 2, where the diagram starts at equiatomic CoCrFeNiTi (x=1) and ends at CoCrFeNi ₂ (x=2). The diagram spans a temperature range of 300 K to 2000 K.	58
Fig. 5.1.2. The Co _x CrFeNiTi _{2-x} computational phase diagram generated by the CALPHAD method. The values of x range from 1 to 2, where the diagram starts at equiatomic CoCrFeNiTi (x=1) and ends at Co ₂ CrFeNi (x=2). The diagram spans a temperature range of 300 K to 2000 K.	59
Fig. 5.1.3. The CoCrFe _x NiTi _{2-x} computational phase diagram generated by the CALPHAD method. The values of x range from 1 to 2, where the diagram starts at equiatomic CoCrFeNiTi (x=1) and ends at CoCr ₂ FeNi (x=2). The diagram spans a temperature range of 300 K to 2000 K.	60
Fig. 5.1.4. The CoCr _x FeNiTi _{2-x} computational phase diagram generated by the CALPHAD method. The values of x range from 1 to 2, where the diagram starts at equiatomic CoCrFeNiTi (x=1) and ends at CoCrFe ₂ Ni (x=2). The diagram spans a temperature range of 300 K to 2000 K.	61
Fig. 5.1.5. Phase fractions of the eta (η) and sigma (σ) phases in the FCC+ETA+SIG phase region at 1100 K as a function of (a) Ni content in CoCrFeNi _x Ti _{2-x} (b) Co content in Co _x CrFeNi _x Ti _{2-x} and (c) Fe content in CoCrFe _x Ni _x Ti _{2-x} (d) Total amount of the eta and sigma phases ie. η + σ in each system. The phase amounts are calculated using CALPHAD.	63
Fig. 5.1.6. Mixing Enthalpy, ΔH _{mix} , as a function of element concentration, x, in (a) CoCrFeNi _x Ti _{2-x} (b) Co _x CrFeNiTi _{2-x} (c) CoCrFe _x NiTi _{2-x} (d) CoCr _x FeNiTi _{2-x}	69
Fig. 5.1.7. Mixing Entropy, ΔS _{mix} , as a function of element concentration, x, in (a) CoCrFeNi _x Ti _{2-x} (b) Co _x CrFeNiTi _{2-x} (c) CoCrFe _x NiTi _{2-x} (d) CoCr _x FeNiTi _{2-x}	69

Fig. 5.1.8. The ratio of ΔH_{mix} to $T\Delta S_{\text{mix}}$, as a function of element concentration, x , in (a) $\text{CoCrFeNi}_x\text{Ti}_{2-x}$ (b) $\text{Co}_x\text{CrFeNiTi}_{2-x}$ (c) $\text{CoCrFe}_x\text{NiTi}_{2-x}$ (d) $\text{CoCr}_x\text{FeNiTi}_{2-x}$	70
Fig. 5.1.9. The deviation of $T\Delta S_{\text{mix}}$, from the ideal solid solution behavior as a function of element concentration, x , in (a) $\text{CoCrFeNi}_x\text{Ti}_{2-x}$ (b) $\text{Co}_x\text{CrFeNiTi}_{2-x}$ (c) $\text{CoCrFe}_x\text{NiTi}_{2-x}$ (d) $\text{CoCr}_x\text{FeNiTi}_{2-x}$	70
Fig. 5.2.1. Lattice constants for Co, Cr, Fe, Ni, and Ti calculated using DFT (relaxed structures); experimental values from Ref. [106]; and calculated values from Ref. [108].....	74
Fig. 5.2.2. Computational stress-strain curves for Co, Cr, Fe, Ni and Ti under uniaxial tension.	75
Fig. 5.2.3. Ideal strength of Co, Cr, Fe, Ni, and Ti determined from computational tensile stress-strain diagrams.	76
Fig. 5.2.4. Stress-strain curve of the weighted average by at.% of the $\text{CoCrFeNi}_{1.75}\text{Ti}_{0.25}$ elements (black) and that of the alloy SQS (red).	77
Fig. 5.2.5. Calculated elastic properties of the $\text{CoCrFeNi}_{1.75}\text{Ti}_{0.25}$ HEA SQS: (a) Young's modulus; (b) Poisson's ratio; (c) Bulk modulus; and (d) Shear modulus.....	78
Fig. 5.2.6. Average atom displacement for each element in the $\text{CoCrFeNi}_{1.75}\text{Ti}_{0.25}$ SQS. This is a means of quantifying the lattice distortion in the relaxed SQS cell. The error bars represent standard deviation within a given element.	82
Fig. 5.2.7. The average magnetic moments for the atoms of each element in the $\text{CoCrFeNi}_{1.75}\text{Ti}_{0.25}$ SQS. The error bars indicate the standard deviation within a given element.	82

List of Tables

Table 3.2.1. The different thresholds for maximum allowable deviation of ΔH_{mix} from $\Delta H_{mixideal}$ for a solid solution to still be able to form a multi-principal element alloy system	16
Table 3.2.2. VEC criteria for structure prediction as determined by Guo et al. [47]	17
Table 3.2.3. Difference in phase selection rules between as cast and annealed HEAs [52]	20
Table 4.1.1. OpenCalphad input example for $\text{CoCrFeNi}_{1.75}\text{Ti}_{0.25}$ at 1500 K	46
Table 4.2.1. Element pseudopotentials for DFT calculations and the recommended energy and charge density cutoffs.	53
Table 4.2.2. Summary of structure, magnetism, and calculated optimal k-points used to treat each of Co, Cr, Fe, Ni, and Ti.	53
Table 5.1.1. Summary of the single FCC phase region limits in the $\text{Co}_x\text{CrFeNiTi}_{2-x}$, $\text{CoCr}_x\text{FeNiTi}_{2-x}$, $\text{CoCrFe}_x\text{NiTi}_{2-x}$, and $\text{CoCrFeNi}_x\text{Ti}_{2-x}$ alloy systems. T_{min} and T_{max} are the lower and upper temperature bounds. x_{min} and x_{max} are the lower and upper composition bounds.	63
Table 5.1.2. Enthalpy of mixing (kJ/mol) of element pairs in the CoCrFeNiTi HEA system [9]	64
Table 5.1.3. Maximum enthalpy and entropy deviation of single FCC solid solution in the Ni, Co, Fe, and	73
Table 5.2.1. final cell parameters (in Å) of the relaxed $\text{CoCrFeNi}_{1.75}\text{Ti}_{0.25}$ 80-atom SQS	75
Table 5.2.2. Young's modulus, Poisson's ratio, and ideal strength as determined from computational tensile stress-strain diagrams. Experimental values and their respective references are also included for comparison.	76
Table 5.2.3. $\text{CoCrFeNi}_{1.75}\text{Ti}_{0.25}$ Young's modulus, Poisson's ratio, and ideal strength determined from the SQS elastic constants analysis and the ideal strength obtained from alloy stress-strain curve.	79
Table 5.2.5. Zero Kelvin energies of the relaxed $\text{CoCrFeNi}_{1.75}\text{Ti}_{0.25}$ SQS and the individual elements: Co; Cr; Fe; Ni; and Ti; and the calculated zero Kelvin alloy formation enthalpies.	80

List of Abbreviations

at. %	Atomic weight percentage
APT	Atomic probe tomography
BCC	Body-Centered Cubic
BCT	Body-Centered Tetragonal
BPR	Ball-to-Powder Ratio
CALPHAD	Calculation of Phase Diagrams
CEF	Compound Energy Formalism
DFT	Density Functional Theory
DR	Dendrite
DOS	Density of States
EOS	Equation of State
FCC	Face-Centered Cubic
GCP	Geometrically Close-Packed
GS	System Gibbs energy in OpenCalphad software output
HCP	Hexagonal Close-Packed
HS	System enthalpy in OpenCalphad software output
IM	Intermetallic
ISS	Interstitial Solid Solution
MA	Mechanical Alloying
MC	Monte Carlo
PCA	Process Control Agent
PM	Powder Metallurgy
QE	QUANTUM ESPRESSO
ROM	Rule of Mixtures
RPM	Revolutions Per Minute
SAD	Selected Area Diffraction

S	System entropy in OpenCalphad software output
SEM	Scanning Electron Microscope
SS	Solid Solution
SSS	Substitutional Solid Solution
SOEC	Second Order Elastic Constants
SPS	Spark Plasma Sintering
SQS	Special Quasirandom Structure
SRO	Short-range ordering
TCP	Topologically Close-Packed
TEM	Transmission Electron Microscope
UTS	Ultimate Tensile Strength
VEC	Vacancy Electron Concentration
wt.%	Weight percent
XRD	X-Ray Diffraction

List of Symbols

ΔG_{mix}	Gibbs free energy of mixing
G_{mix}^{excess}	Excess Gibbs free energy of mixing
ΔG_{mix}^{ideal}	Ideal Gibbs free energy of mixing
G_m^φ	Molar Gibbs energy function of a phase with structure φ
$G_{m,ref}^\varphi$	Elemental reference of the Gibbs energy of a phase with structure φ
$G_{m,id}^\varphi$	Ideal molar Gibbs energy of a phase with structure φ
$G_{m,ex}^\varphi$	Non-magnetic excess molar Gibbs energy of a phase with structure φ
$G_{m,mag}^\varphi$	Magnetic excess molar Gibbs energy of a phase with structure φ
ΔH_{mix}	Enthalpy of mixing
ΔH_{mix}^{ideal}	Ideal enthalpy of mixing
H_{mix}^{excess}	Excess enthalpy of mixing
$H_{f,0k}$	Zero Kelvin Formation Energy
ΔH_{IM}	Enthalpy of formation of an intermetallic phase
ΔS_{mix}	Entropy of mixing
ΔS_{mix}^{ideal}	Ideal entropy of mixing
ΔS_{conf}	Configurational entropy
ΔS_{elec}	Electronic entropy
ΔS_{vib}	Vibrational entropy
S_{mix}^{excess}	Excess entropy of mixing
ΔS_{IM}	Entropy of formation of an intermetallic phase
$\vec{r}_{i,initial}$	Initial Position of an Atom of Element i
$\vec{r}_{i,final}$	Final Position of an Atom of Element i
σ	Sigma – an intermetallic phase
δ	The comprehensive atomic size difference parameter or the Delta Intermetallic phase

γ	Gamma – a disordered face-centered cubic (FCC) solid solution phase
γ'	Gamma Prime – an intermetallic phase
ν	Poisson's Ratio
ϵ	Strain
$\mu_{i,avg}$	Average Magnetic Moment of Atoms of Element i in an SQS
$\mu_{i,SQS}$	Magnetic Moment of an Atom of Element i in an SQS
μ_i	Magnetic Moment of an Atom of Element i in the Relaxed Structure
ϵ_{trans}	Transverse Strain
ϵ_{long}	Longitudinal Strain
E_{cut}	Energy cut-off value for DFT calculations
ρ_{cut}	Charge density cut-off value for DFT calculations
\AA	Angstrom
B	Bulk Modulus
$D_{i,avg}$	Average Displacement of Atoms of Element i
D_{avg}	Average displacement of All Atom Types
$E_{SQS,relax}$	Total Energy of the SQS Relaxed Structure
$E_{i,relax}$	Total Energy of the Relaxed Structure of Element i
K	Kelvin
$n_{i,cell}$	Number of Atoms in a Unit Cell of Element i
$n_{i,SQS}$	Number of Atoms of Element i in the SQS
P	Pressure
Pa	Pascal
R	The gas constant = $8.3145 \text{ J K}^{-1}\text{mol}^{-1}$
Ry	Rydberg
T	Temperature
x_i	Mole fraction of element i
Y	Young's Modulus

ΔX	The comprehensive electronegativity difference of a multi-principal element system
μ_B	Bohr Magneteton

Chapter 1. Introduction

High entropy alloys (HEAs) were first formally introduced by Yeh et al. [1] in 2004 as a new class of alloys based on the concept of multiple principal elements. This contradicted the way in which alloys had been conventionally made, where they typically consist of a single principal element (the solvent) with minor additions of secondary alloying elements (solute) for property enhancement. According to conventional metallurgical principals, alloys with multiple principal elements are expected to form numerous secondary intermetallic phases, which in some cases can lead to unfavorable mechanical properties. However, the authors of Ref. [1] argued and showed that simple solid solution microstructures were possible for HEAs rather than the intermetallic-rich structures originally expected. Shortly after, this was also confirmed by Cantor et al. [2]. During these early stages of HEA research, they were commonly defined as alloys consisting of five or more elements, the concentration of each ranging between 5 and 35 by atomic weight percent (at.%), such that all the constituents are principal elements. It was also proposed that the high configurational entropy, resulting from the presence of multiple principal elements, was the main reason for favoring solid solution phases over intermetallics. It was argued that when the configurational entropy of an alloy is sufficiently high, it would favor the formation of single solid solution over an intermetallic phase [1].

While the field of HEAs has evolved greatly since 2004, they remain the focus of many studies due to the interesting phenomena that arise as a result of their multi-principal element nature. These have made it possible for HEAs to possess important properties, such as high-temperature stability and extreme corrosion resistance, to the extent that they can potentially outperform conventional alloys in many applications. Turbine blades, thermal coatings, and structural components for nuclear reactors are only some examples of areas where HEAs are being used to overcome the shortcomings of conventional materials [3].

One of the biggest obstacles in the study of HEAs, is the massive compositional search space of a given HEA system. Originally equiatomic compositions were a major focus of HEA studies under the assumption that such a composition would possess the highest configurational entropy. However, the importance of exploring non-equiatomic compositions has been made clear by the progress made in the field. This enlarges the compositional space that requires exploration even further making the problem even more severe. Since alloy compositions have a direct effect on their resulting thermodynamic phases, which consequently affect their properties, this highlights the importance of composition selection as an integral part of the alloy design process.

Phase diagrams are essential tools for the exploration of the phase stabilities in alloys under different conditions [4]. However, the large search space of HEA compositions makes it impossible to produce experimental phase diagrams, an already resource-intensive task, and accordingly, computational methods become the only feasible option. The Calculation of Phase Diagrams (CALPHAD) method is one such approach that has become central to HEA research.

The CALPHAD method makes use of computational thermodynamics to model alloys and calculate their equilibrium states and, as its name suggests, it makes it possible to produce computational phase diagrams of different alloy systems. One major advantage of the CALPHAD method is its ability to extrapolate phase information for higher-order alloy systems, such as HEAs, using experimental and computational data of binary and ternary systems of the same elements, which tend to be more readily available and easier to obtain. Consequently, CALPHAD offers a promising means of efficiently exploring HEAs, which would otherwise be too time-consuming and expensive to achieve experimentally [5].

Although HEA research was initially motivated by the search for single solid solution phase alloys, many multi-phase HEAs are now being studied for use in various applications. This shift in interest came after the realization that achieving a single solid solution phase in HEAs is no simple task, contrary to the original theories put forth [6]. One example is precipitation hardened HEAs [7], which are an attempt to take advantage of the intermetallic phases that inevitably form. Such attempts have been met with varying degrees of success and while significant increases in alloy strength can often be achieved, this is usually accompanied by a severe deterioration in alloy ductility. Accordingly, this suggests that the pursuit of single-phase HEAs is still a valid endeavor.

Regardless of the type of phases sought, much of the underlying theory and reasons behind phase stabilities in HEAs remain unknown [8]. One interesting problem in this regard is the link between HEA composition and the resulting phase stabilities. In this study a thermodynamic approach is followed by applying the CALPHAD method to the CoCrFeNiTi HEA system to explore the link between alloy composition and thermodynamic behavior, which affect the equilibrium phases produced. Moreover, the ideas originally proposed by Yeh et al. [1] with regards to the stabilization of single solid solution phases are revisited.

The choice of the CoCrFeNiTi system was based on its current significance in the HEA field [9]–[16], which stems from its potential to form alloys with good strength and ductility, an important yet often difficult combination to achieve. Furthermore, understanding its phase stabilities would aid with the effective design of its alloys such that favorable structures and consequently desirable properties are achieved. Moreover, its non-equiatomic compositions have been found to consist of predominantly face-centered cubic (FCC) solid solution structures [9], [17]. This makes it a good candidate for studying the thermodynamic behavior of HEAs, especially in the stabilization of single solid solution phases as opposed to multi-phase ones.

This study aims at contributing to the thermodynamic understanding of phase stabilities in HEAs and especially those of the CoCrFeNiTi system. Extensive computational phase diagrams covering large composition and temperature ranges for subsystems of the CoCrFeNiTi system are presented for the first time (to the best of our knowledge). Thermodynamic state functions such as enthalpy and entropy are calculated, and their functional dependence on temperature and composition is used to explain the equilibrium phases obtained in the phase diagrams. Finding

possible links between such thermodynamic functions and phase diagram results is important for developing the necessary knowledge for the advancement of the thermodynamic modelling of HEAs, and more generally multi-component alloys. Robust predictive models are essential for the effective and efficient design of HEAs, since their systematic experimental exploration is often a tedious, and sometimes impossible, task.

In addition to the thermodynamic analysis, a first principles computational characterization of the mechanical properties of an alloy consisting of a single FCC solid solution phase is presented. The structure of the selected alloy was modelled using a special quasirandom structure (SQS) and the properties were calculated using density functional theory (DFT). The present work offers a framework for combining both CALPHAD and first principles approaches for the successful design of HEAs.

Chapter 2. Background and Thermodynamic Theory of Alloys

2.1. Phase Diagrams

Phase diagrams are considered roadmaps for alloy design. A phase diagram shows the equilibrium phases of a system under varying conditions of composition, temperature, and pressure. Due to the close link between the structure of an alloy and its mechanical properties, phase diagrams are essential tools for material scientists to be able to design alloys by selecting suitable compositions and processing techniques to achieve targeted properties [18].

Traditionally, phase diagrams have been constructed by carrying out equilibration experiments, in which various samples of an alloy are fabricated and allowed to reach equilibrium while undergoing structural and thermal testing. However, this approach requires extensive material and time resources if a comprehensive phase diagram is to be produced. Nevertheless, due to their importance, many experimental phase diagrams have been developed and are now available for numerous binary and ternary alloy systems, while computational methods are usually needed for higher-order systems [19].

In the present study, the CALPHAD method is used to construct computational phase diagrams of the CoCrFeNiTi quinary HEA system, with a focus on alloy compositions that form single solid solution structures. Accordingly, some of the basic concepts relating to phase diagrams and the formation of different phases are reviewed in this section.

2.1.1. Phases and Microstructures

A phase is a region of a material with a homogeneous structure, composition, and properties, that are distinguishable from those of surrounding regions. Alloys can have single- or multi-phase structures and the number, types, amounts, and distribution of phases of an alloy play a major role in determining its mechanical properties [20]. Accordingly, a good understanding of the different types of phases and the underlying reasons for their formation is necessary to be able to target and produce favorable alloy microstructures.

2.1.1.1. *Random Solid Solution Phases*

Solid solution phases form when atoms of one element, which acts as the solute, dissolve within the crystal lattice of another element, which acts as the solvent. Two types of solid solutions can form depending on the types of elements of the solute and solvent atoms. The first is a substitutional solid solution (SSS), in which the solute atoms replace (or substitute) those of the solvent in the lattice. The other type of solid solution is an interstitial solid solution (ISS), where the solute atoms occupy the spaces in between the solvent atoms, known as interstitial sites. Interstitial sites in metallic elements tend to be small, which limits the types of solute elements that can form ISSs to elements with atomic size that are much smaller than the size of the solvent atoms [18], [21]. Fig. 2.1.1 illustrates the difference between both types of solid solutions.

The types of solid solutions discussed above are random solid solutions, in that they exhibit a random distribution of the solute and solvent atoms in their crystal lattice with no preferential

occupation of lattice sites. Moreover, for the purposes of studying CoCrFeNiTi HEAs, we are primarily interested in random substitutional solid solutions, since the atoms are of similar sizes and an ISS is therefore unlikely to form. For simplicity, random substitutional solid solutions will therefore be referred to as merely solid solutions.

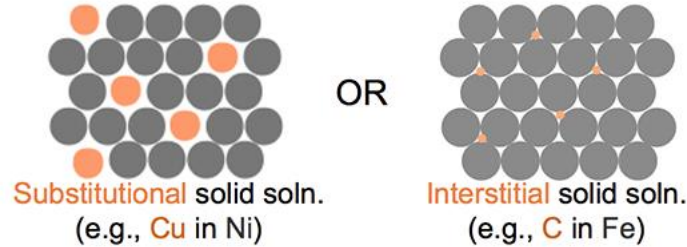


Fig. 2.1.1. A comparison of a substitutional solid solution (SSS) to an interstitial solid solution (ISS) [21].

2.1.1.2. Intermetallic Compounds

Intermetallic compounds are phases that form between chemically dissimilar metals, meaning when one metal is strongly metallic and the other is weakly metallic. The bonding in such compounds is not strictly metallic and can exhibit covalent and/or ionic characters depending on the elements present. This type of bonding influences the properties of intermetallic compounds, which tend to be hard and brittle and exhibit other non-metallic properties [22].

In contrast to random solid solutions, intermetallic compounds exhibit ordered structures, meaning atoms of different elements occupy lattice sites preferentially based on factors such as atomic size and electronegativity [23]. Intermetallic compounds also vary in structural complexity and properties depending on the number and types of their constituents. Fig. 2.1.2 compares the structures of solid solutions to that of an intermetallic compound [24].

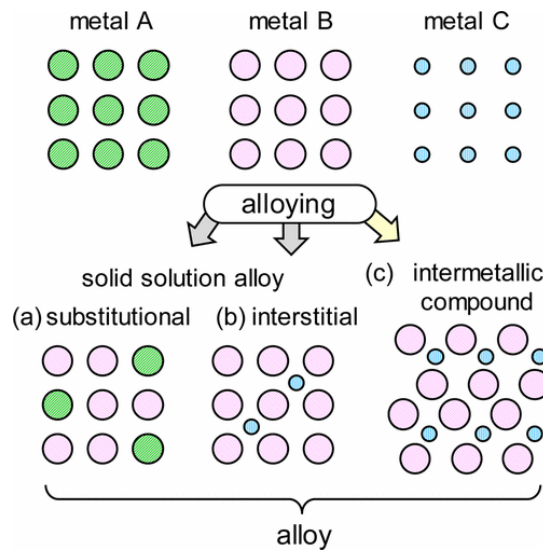


Fig. 2.1.2. Comparing the structures of solid solutions to that of an intermetallic compound [24].

2.1.1.3. Mixed Microstructures

Multi-phase alloys with microstructures consisting of combinations of solid solution and intermetallic phases are commonly encountered. Under certain composition and processing conditions, the intermetallic phases can precipitate out of the solid solution phase. This can impart favorable properties to the alloy, as in the case of the γ' phase in Ni-superalloys. On the other hand, it can also lead to a deterioration of alloy properties such in the case of the precipitation of the sigma (σ) and Laves phases in the same alloys [25]. This emphasizes the influence of the alloy microstructure on its mechanical properties and performance. Fig. 2.1.3 illustrates the different alloy structures that can form in a three-element alloy system [8].

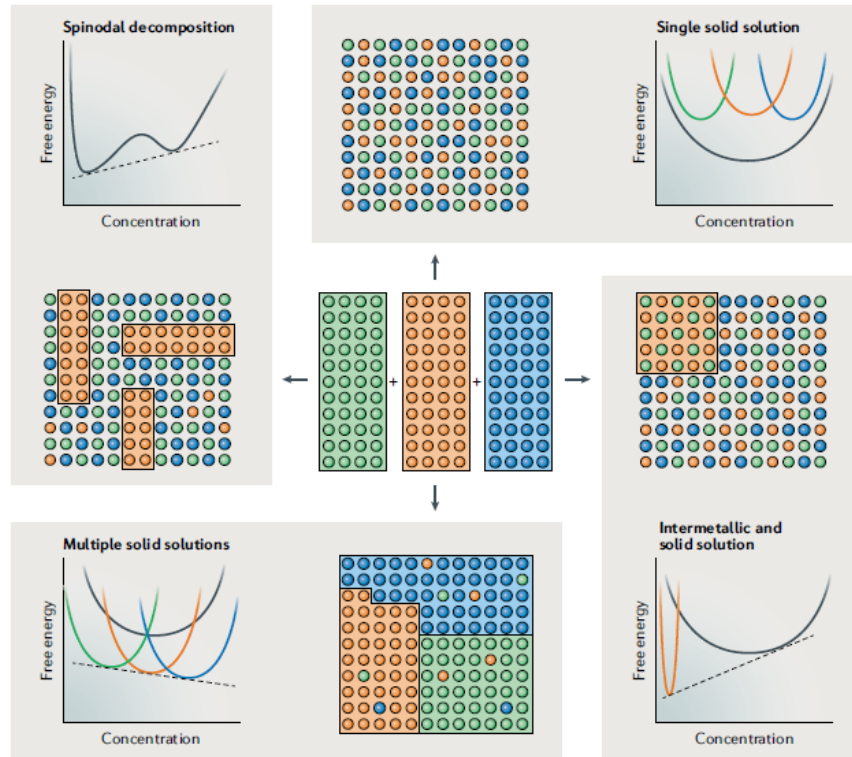


Fig. 2.1.3. Possible structures that result from mixing three elements: Single solid solution structure with random mixing; Mixed solid solution (random) and intermetallic compound (ordered); Multiple solid solutions with random mixing in each; Solid solution with spinodal decomposition (phase separation) [8].

2.2. Thermodynamics of Alloys and Solid Solutions

2.2.1. Definitions of the Gibbs Free Energy, Enthalpy, and Entropy

The CALPHAD method is based on calculating the equilibrium state of a system through a minimization of its Gibbs energy. This is because, under constant temperature and pressure, equilibrium is achieved in a system when it reaches its minimum Gibbs energy. It is often referred to as the Gibbs free energy as it is the amount of energy in the system that is free to do work [26].

The Gibbs energy is among the most commonly used functions in materials thermodynamics and has been central to the explanation of phase stabilities in alloy systems. It is

given by Equation 2.2.1, where H is the enthalpy of the system T is the temperature and S is its entropy [27].

$$G = H - T.S \quad \text{Equation 2.2.1}$$

Roughly speaking, the enthalpy of a system is a measure of its internal energy in addition to any pressure-volume contributions, while its entropy is a measure of its disorder. Systems tend to undergo changes that decrease their enthalpies and increase their entropies, which collectively leads to minimizing their Gibbs energy. By examining changes in G, H, and S, information regarding the driving forces of a reaction, its spontaneity, and its equilibrium condition can be known [28].

2.2.2. Mixing

When the Gibbs energy equation is applied to alloy systems, the subscript “mix” is usually used. This is because from a thermodynamic standpoint, alloy systems can be regarded as mechanical mixtures. The primary interest of this study is to gain an understanding of the thermodynamic stabilization of single solid solution phases in HEAs, specifically the single FCC phase in CoCrFeNiTi HEAs. It is therefore important to review the thermodynamic principles of solid solution alloys. It should also be emphasized that the following discussion pertains only to the thermodynamics of the formation of alloys and their final equilibrium states and does not consider any kinetic contributions.

2.2.2.1. The Gibbs Energy of Mixing

When mixing elements together to form solid solutions, the final phase stabilities are governed by changes in the system’s Gibbs free energy of mixing, ΔG_{mix} , which are dependent on the interactions that occur between the mixed elements. More specifically, ΔG_{mix} depends on the enthalpy of mixing, ΔH_{mix} , and entropy of mixing, ΔS_{mix} . These quantities are related by Equation 2.2.2.

$$\Delta G_{mix} = \Delta H_{mix} - T\Delta S_{mix} \quad \text{Equation 2.2.2}$$

It should be noted that the above quantities refer to system values. It is possible to calculate the same properties for each elemental component in the system, called a partial molar quantity. At constant pressure and temperature, for an arbitrary extensive thermodynamic property Y, Y_i is the partial molar quantity (which is an intensive quantity), where

$$dY|_{p,T} = \sum_i^n Y_i dn_i \quad \text{Equation 2.2.3}$$

and

$$Y_i = \left(\frac{\delta Y}{\delta n_i} \right)_{p,T,n_{j \neq i}} \quad \text{Equation 2.2.4}$$

Where n_i is the number of moles of element i present and n_j is the number of moles of the remaining species. As an example, for the system of interest, which consists of Co, Cr, Fe, Ni, and Ti

$$dG|_{p,T} = \mu_{Co}dn_{Co} + \mu_{Cr}dn_{Cr} + \mu_{Fe}dn_{Fe} + \mu_{Ni}dn_{Ni} + \mu_{Ti}dn_{Ti}$$

where,

$$\mu_{Co} = \left(\frac{\delta G}{\delta n_{Co}} \right)_{p,T, n_{Cr}, n_{Fe}, n_{Ni}, n_{Ti}}, \mu_{Cr} = \left(\frac{\delta G}{\delta n_{Cr}} \right)_{p,T, n_{Co}, n_{Fe}, n_{Ni}, n_{Ti}}, \dots \text{ etc.}$$

At a given pressure, temperature, and composition, a phase (or phases) will be stable in an alloy if it (they) minimizes (minimize) the ΔG_{mix} of the system, where typically $\Delta G_{mix} < 0$. It is clear from Equation 2.2.2. that this minimization is dependent on the values of both ΔH_{mix} and ΔS_{mix} .

2.2.2.2. Ideal Solutions

Before discussing the significance of each of the above terms, the concept of an ideal solution should be introduced. While most solutions do not fall under this category, it is still a useful model since it can often be applied to some real solutions after some modifications, and after all it is the easiest model to compute with. Moreover, single solid solution phases in real alloys can sometimes approach this ideal behavior [29].

An ideal solution can be described as one in which changes in the interatomic (or intermolecular) interactions resulting from the mixing are negligible. Additionally, atoms are supposed to be distributed randomly over lattice site. Accordingly, it follows that ΔH_{mix}^{ideal} should be zero, which means that no heat is absorbed or released on mixing. On the other hand, for non-ideal solutions ΔH_{mix} can be either a positive or negative value. For solid solution phases, a large positive enthalpy of mixing between elements indicates that they will likely repel each other in the solution leading to elemental segregation and can therefore destabilize the solid solution phase. On the other hand, large negative enthalpies of mixing can lead to short-range ordering (SRO) but can also play an important role in stabilizing the solid solution phase [30].

Similarly, on mixing elements to form an ideal solution, acceptable entropic changes are only those attributed to the positions or configuration of the atoms in the solution. Therefore, we see from Equation 2.2.6 that ΔS_{mix}^{ideal} is equal to the configurational entropy of a system of n components. ΔS_{mix}^{ideal} is maximized for random mixing, meaning the elements substitute freely in the solution, and also when the available atomic positions are equivalent. This has two important consequences for forming solid solutions. First, maximizing ΔS_{mix}^{ideal} should theoretically suppress the separation of elements and in turn favor the formation of a single phase solution and second, simple lattice structures in which lattice sites are equivalent, such as FCC and BCC, are also favored [13].

$$\Delta H_{mix}^{ideal} = 0 \quad \text{Equation 2.2.5}$$

$$\Delta S_{mix}^{ideal} = \Delta S_{mix,conf} = -R \sum_i^n x_i \ln x_i \quad \text{Equation 2.2.6}$$

$$\Delta G_{mix}^{ideal} = RT \sum_i^n x_i \ln x_i \quad \text{Equation 2.2.7}$$

where x_i is the mole fraction component i , n is the number of components, and R is the gas constant equal to $8.3145 \text{ J K}^{-1}\text{mol}^{-1}$. The above equations and their exact derivations can be found in ref. [1] and [2].

2.2.2.3. Deviation from Ideal Behavior and Excess Quantities

Excess quantities of the above thermodynamic functions are a measure of the deviation of a real solution from ideal behavior. This is important for several reasons. First, the magnitude of the deviation and its sign (positive or negative deviation) can give information about the interatomic interactions introduced on mixing, which help explaining the obtained equilibrium structures. Developing an understanding of such interactions and changes can help greatly in the design of alloys by providing criteria for structure prediction based on which elements are added together. The excess quantities for the Gibbs free energy, enthalpy, and entropy of mixing are given by the following equations

$$G_{mix}^{excess} = \Delta G_{mix} - \Delta G_{mix}^{ideal} \quad \text{Equation 2.2.8}$$

$$H_{mix}^{excess} = \Delta H_{mix} - \Delta H_{mix}^{ideal} = \Delta H_{mix} \quad \text{Equation 2.2.9}$$

$$S_{mix}^{excess} = \Delta S_{mix} - \Delta S_{mix}^{ideal} \quad \text{Equation 2.2.10}$$

In the present work, the above quantities are calculated using CALPHAD and are thoroughly analyzed and related to phase diagrams of CoCrFeNiTi HEAs also constructed using the CALPHAD method. Moreover, some quantities such as the alloy formation energy are additionally evaluated from first principles using density functional theory (DFT).

Chapter 3. Literature Review

3.1. Overview of High Entropy Alloys

As their name suggests, HEAs are alloys with configurational entropy significantly larger than that of conventional alloys. This increase in configurational entropy is a direct result of increasing the number of principal elements in the alloy system and the realization of a disordered solid solution, which leads to the interesting properties of HEAs. In recent years, this concept has also been applied to other material classes such as ceramics[33], [34] and composites [35], which has led to the conception of a new research area termed high entropy materials (HEMs). The main advantage of such materials is the massive number of possible compositions, which corresponds to a large variety of resulting structures and properties that can be employed for improved material performance for different service conditions. The importance and potential of HEMs, including

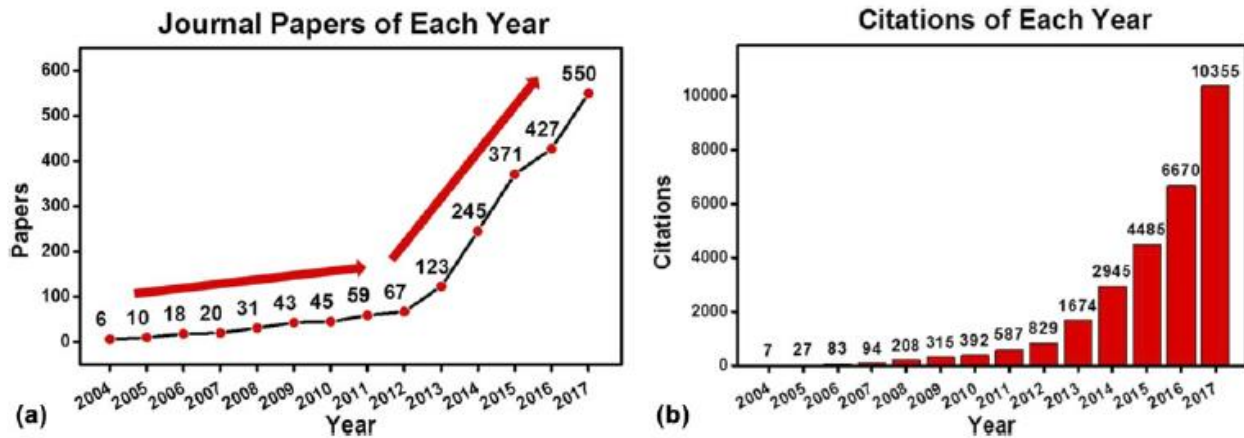


Fig. 3.1.1. (a) The number of publications per year on high entropy materials (HEMs) (b) The number of citations per year for HEM papers since between 2004 and 2017 [3].

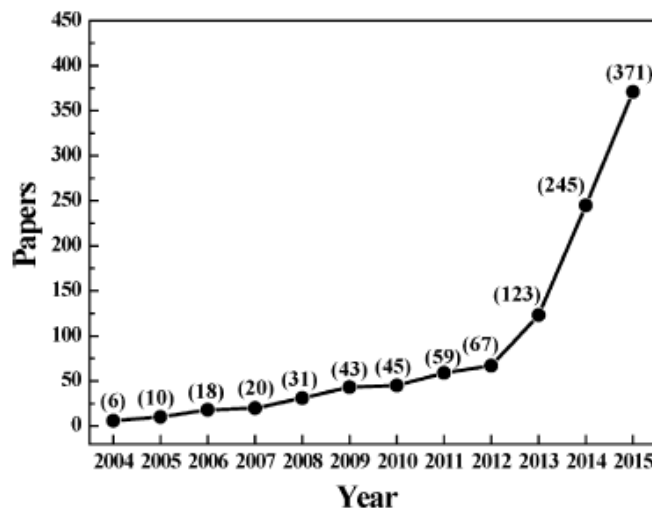


Fig. 3.1.2. The number of publications per year on high entropy alloys (HEAs) between 2004 and 2015 [36].

HEAs, is reflected in the significant increase in the number of HEM studies published since 2004 as shown in Fig. 3.1.1 and Fig. 3.1.2 [3], [36].

The stability of the relatively simple solid solution phases in HEAs was originally attributed to their high mixing configurational entropy which, assuming an ideal solid solution can be expressed as,

$$\Delta S_{conf} = -R \sum_i^n x_i \ln x_i \quad \text{Equation 3.1.1}$$

where n is the number of principal elements and x_i is the mole fraction of component i , and R is the gas constant equal to $8.3145 \text{ J K}^{-1}\text{mol}^{-1}$. As can be seen from the above equation, ΔS_{conf} increases with increasing the number of principal elements in the alloy. Large values of ΔS_{conf} lower the tendency of elemental segregation and intermetallic phase formation by countering the effects introduced by the mixing enthalpies, if they are not very large themselves, and thereby promote the formation of single solid solution phases. From here came the very first definition of HEAs as those consisting of 5 or more principal elements, where the concentration of each element can vary between 5 and 35 at. wt.% [1].

An interesting observation regarding ΔS_{conf} is the that its value is maximized at the equiatomic composition of the system. This motivated the development of an alternative definition, which highlights the large ΔS_{conf} that distinguish HEAs. For the minimum 5-principal element threshold determined for the composition-based definition and at equiatomic ratios of the elements, $\Delta S_{conf} = 1.61R$. Accordingly, HEAs have also been defined as those whose mixing entropy is equal to or exceeds this value [37].

3.1.1. The Significance of HEAs and the Four Core Effects

The entropic stabilization of simple solid solution phases is only one of four core effects, which result in the many interesting properties of HEAs [37]. The high entropy effect and its role in HEAs has already been presented in the previous section. The following are the remaining three core effects in HEAs:

(i) Severe Lattice Distortion

This occurs primarily due to the atomic size difference between the different elements that form HEAs. Since the nearest neighbors of an atom are likely to all be different in an HEA, this introduces severe strain and distortion in its lattice. Other important factors that contribute to the lattice distortion effect are the different electronic and crystal structures of neighboring atoms in their native metal crystals, which affect their bonding in the lattice of the HEA. These differences and their effects tend to be amplified in HEAs compared to conventional alloys due to the increased likelihood that all or most of the nearest neighbors of a specific atom will be different, which becomes even more likely as the number of elements in the alloy system is increased. The

examples of 10-element and 5-element alloy systems are used to illustrate these concepts in Fig. 3.1.3 [38].

The lattice distortion effect has mostly positive effects on HEA properties as it results in significant solid solution strengthening and increases the alloys' structural stability at high temperature. However, in some cases, amorphous structures can form if lattice distortion exceeds a certain limit, which might not be desirable for the intended application [37].

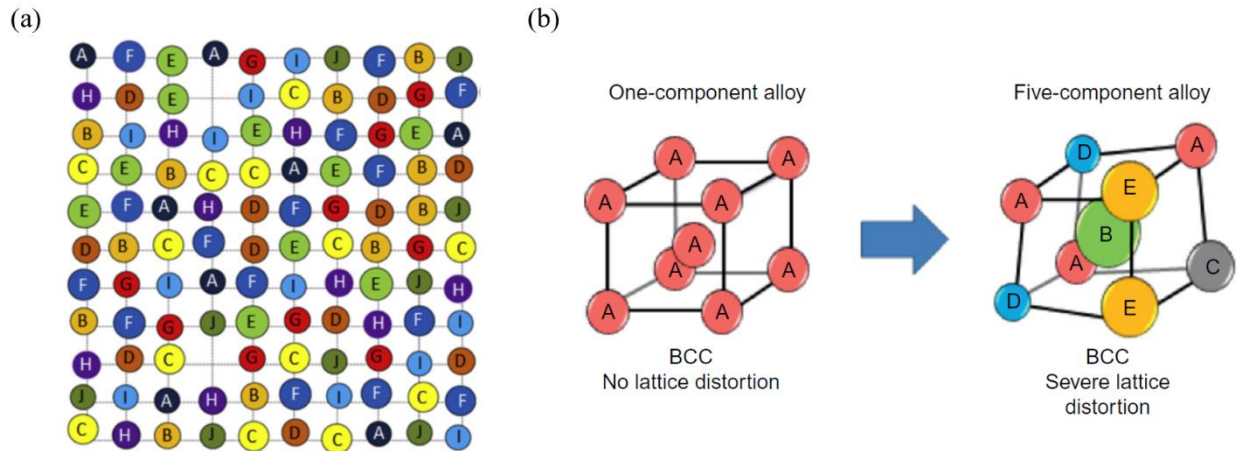


Fig. 3.1.3. (a) An example of a lattice in a 10-element system. The nearest neighbors of a given atom mostly consist of different elements. (b) A comparison between a BCC unit cell for a 1-element system and a 5-element system illustrating the resulting lattice distortion on varying the elements and its effect on the unit cell structure [38].

(ii) Sluggish Diffusion

The sluggish diffusion effect refers to the kinetic impediment HEA lattices pose to the diffusion of atomic species within them. This is important in relation to diffusion-controlled phase transformations that lead to the formation of new phases and their development, as diffusion affects phase nucleation, growth, and distribution within the alloy. One of the most important consequences of the sluggish diffusion effect is its hindrance to grain growth after nucleation, which leads to finer and hence stronger structures. This also means that once fine structures are achieved it is easier to maintain them throughout high-temperature processing and in service compared to conventional alloys adding to HEAs' high-temperature stability [38].

(iii) Cocktail Effect

The cocktail effect refers to treating HEAs as composites in the sense that an HEA can exhibit a combination of properties that is not possible for any element or lower-order alloy within the HEA's subsystems. This emphasizes the importance of element selection in HEAs, as each element is likely to contribute at least some of its properties to the final alloy formed. Moreover, it has been shown that elements can work together synergistically to enhance a specific property. For example, in refractory HEAs their constituent elements possess high melting temperatures individually. However, when alloyed together into HEAs the resulting alloys exhibit melting

temperatures much higher than any constituent element and even super alloys of the same elements [3], [39].

3.1.2. Current Definitions of HEAs

After numerous studies focusing on HEAs (extensively reviewed in ref. [29]), the initially developed definitions stated above have been shifting to incorporate a more general picture in terms of the structures expected for HEAs. The main premise that is being reassessed is the underlying assumption that ΔS_{conf} alone is sufficient to suppress intermetallic phase formation. While ΔS_{conf} does play an important role in promoting the formation of simple solid solution phases, it has been shown that more complex microstructures than those originally anticipated can arise even if a given combination of elements follows the composition-based and/or entropy-based definition of HEAs [29]. Alternately, there is a vast evidence to support that a combination of factors and their effects on elemental compatibility are what determines the final structure obtained, rather than any one single parameter or property.

The factors affecting the final structure of HEAs will be discussed extensively in the upcoming sections of this thesis. However, it is useful to first briefly highlight an example of the changes occurring in HEA theory by considering the study by Manzoor et al. [40]. In this report, Density functional Theory (DFT) was used to explore the roles of different entropic contributions including the electronic, vibrational, and configurational entropies on phase stabilities in binary alloys as a step towards understanding their effects in HEAs. The authors emphasize the inaccuracy that can result from relying on a single thermodynamic property (such as the configurational entropy) to predict the stability or instability of a given phase. They show that a comprehensive picture of ΔG_{mix} , ΔH_{mix} , and ΔS_{mix} (including its different contributions) is necessary in order to explain certain phase stabilities as shown by the examples in Fig. 3.1.4. From the DFT calculations, the authors showed that the electronic entropy usually has a negligible effect on the resulting structure. On the other hand, while the contribution of the vibrational entropy is not as significant as that of the configurational entropy, it is capable of stabilizing or destabilizing solid solution phases. The quaternary FeNiCoCr alloy was used to illustrate the importance of the vibrational entropy in higher order systems. Experimentally, this alloy has been found to possess a single solid solution structure, despite its calculated ΔH_{mix} value, which indicates the instability of the solid solution phase. The authors, therefore, attribute the experimental structure to the alloy's vibrational entropy (27% of total entropy for that particular system), which reduces the temperature at which the solid solution phase can be stabilized to room temperature, which would otherwise be 600 K.

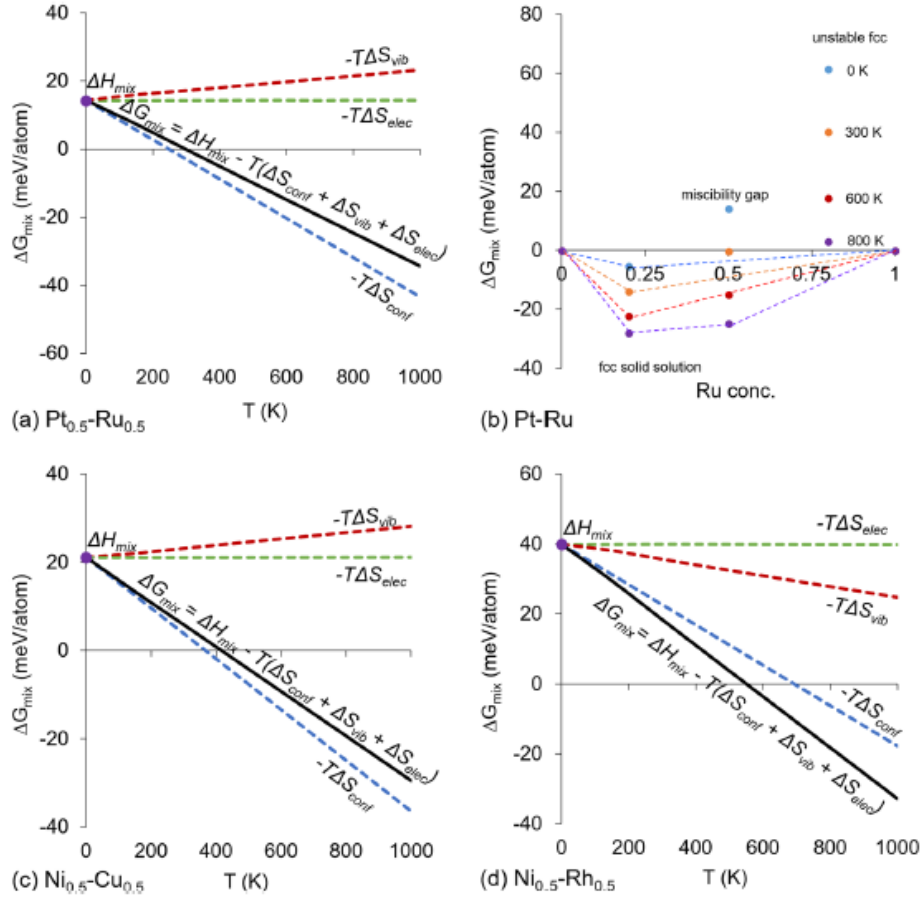


Fig. 3.1.4. (a) ΔG_{mix} vs. T of a $\text{Pt}_{0.5}\text{-Ru}_{0.5}$ binary alloy with an increasing slope for $-T\Delta S_{\text{vib}}$ indicating it destabilizes the solid solution phase (b) a convex hull plot for the Pt-Ru alloy system (c) ΔG_{mix} vs. T of a $\text{Ni}_{0.5}\text{-Cu}_{0.5}$ binary alloy also with a destabilizing $-T\Delta S_{\text{vib}}$ contribution (d) ΔG_{mix} vs. T of a $\text{Ni}_{0.5}\text{-Rh}_{0.5}$ binary alloy with a decreasing slope for $-T\Delta S_{\text{vib}}$ indicating it stabilizes the solid solution phase [40].

3.2. Alloy Design

Although it is proving more difficult than initially thought to achieve single solid solution structures, HEAs still offer exceptional properties that make them remarkably valuable to study. However, despite the many advantages of HEAs, their full exploitation remains hindered by the massive compositional search space available for a given multi-principal element system. Conventional experimental methods used in studying the phase stabilities of lower-order alloy systems require extensive time and material resources and are increasingly ineffective in the case of HEAs. Accordingly, the development and use of computational methods for HEA design have been central to their exploration. These methods typically involve the use of computational thermodynamics to either calculate relevant thermodynamic properties or to generate the phase diagram of a given system [36].

The ability to computationally design alloys and target specific structures and properties for different applications is important because it can save much of the time and resources that go

into trial and error approaches. However, this requires developing the correct tools for accurate structure prediction. For example, parametric approaches can be used for screening for desirable element combinations and alloy compositions if reliable parameters and criteria are developed for determining the resulting structures. On the other hand, once an alloy system has been chosen, it becomes useful to explore specific phase stabilities at different compositions and temperatures, and this can be achieved through producing computational phase diagrams. It is also important to be able to calculate and screen alloys based on their mechanical properties prior to resorting to experiments. This can be achieved using first principles approaches in which alloy properties are determined from density functional theory (DFT) calculations. All three approaches have been beneficial and essential to the design and study of HEAs. CALPHAD and DFT are central to the present work and accordingly will be discussed in depth in the coming sections. However, it is also worthwhile to first briefly review some of the most prominent parametric approaches used in HEA studies.

3.2.1. Parametric Approaches and Empirical Models

Since not every equiatomic multi-principal element system is capable of forming simple solid solution phases, many attempts have been made to develop parameters and criteria to help with predicting the type of structures (SS, IM, or both) that should be expected from a given combination of elements at a specific composition. The ability of a system to stabilize solid solutions was the main interest of these efforts in addition to the type of solid solution, ie. FCC or BCC, that would form. The following parameters and criteria have therefore been suggested as a measure of the solid solution-forming ability of different multi-principal element systems.

(i) Minimum Allowable Mixing Entropy, ΔS_{mix}

As stated in the entropy-based definition of HEAs, mixing elements will more likely result in solid solution phases if their entropy of mixing is greater than or equal to $1.61R$ [37]. Accordingly, ΔS_{mix} should be $\geq 1.61R$ to favor the formation of a solid solution phase. The main difference between the previous definition and its use here as a parameter for structure prediction is that in this case, it is not assumed that it is the sole factor in determining the type of structure that will be formed. Contrary to before, it is now acknowledged that it is a combination of factors including mixing entropy that are capable of stabilizing or destabilizing a certain phase or structure [41].

(ii) Maximum Tolerable Deviation of ΔH_{mix} from ΔH_{mix}^{ideal}

As mentioned in section 1, the mixing enthalpy is an indication of the types of interactions that occur between elements in a liquid or solid solution. Recalling that large positive values of ΔH_{mix} result in elemental segregation and phase separation while large negative values can lead to SRO and also recalling that $\Delta H_{mix}^{ideal} = 0$, it can be seen that solid solution phases will typically form when the positive or negative deviation from the ideal case is minimal.

Several attempts have been made to determine the thresholds of tolerable deviation of ΔH_{mix} from ideal behavior within which a solid solution can still form (ie. segregation and compound formation are prevented) [30], [41]–[44]. These studies approach this task by calculating the ΔH_{mix} for a given system at a specific composition using the following model

$$\Delta H_{mix} = \sum_{i=1, i \neq j}^n \Omega_{ij} c_i c_j \quad \text{Equation 3.2.1}$$

where

$$\Omega_{ij} = 4\Delta H_{mix,AB} \quad \text{Equation 3.2.2}$$

c_i and c_j are the concentrations of elements i and j respectively and $\Delta H_{mix,AB}$ can be obtained from ref. [45]. Experimental results at the compositions of interest are then used to try and establish the allowable deviations from ΔH_{mix}^{ideal} . Table 3.2.1 summarizes the thresholds of allowable deviations of ΔH_{mix} determined by these studies.

Table 3.2.1. The different thresholds for maximum allowable deviation of ΔH_{mix} from ΔH_{mix}^{ideal} for a solid solution to still be able to form a multi-principal element alloy system

Maximum Allowable Deviation of ΔH_{mix}	Reference
$-15 \text{ kJ/mol} < \Delta H_{mix} < 5 \text{ kJ/mol}^1$	[30], [41], [42]
$-22 \text{ kJ/mol} < \Delta H_{mix} < 7 \text{ kJ/mol}$	[43]
$-4 \text{ kJ/mol} < \Delta H_{mix} < 2 \text{ kJ/mol}^2$	[44]

¹ Commonly accepted range

² Values are determined from CoCrFeMnNi system

(iii) The Atomic Size Difference Parameter, δ

The notion of developing a parameter that measures the differences in atomic radii of the constituent elements of an alloy is also present in conventional metallurgy as one of the criteria of the Hume-Rothery rules for extended solid solubility in binaries. This states that elements whose atomic radii are within $\pm 15\%$ of each other are likely to form a solid solution given that they are chemically compatible [18]. A similar approach has been adopted for HEAs and the parameter δ has been formulated for this purpose.

Contrary to binary systems, HEAs contain much more atom pairs of different elements that have to be accounted for when considering atomic size differences in addition to the fact that there are no specific solute or solvent elements (all elements are principal elements). Accordingly, δ has been formulated in a way that captures this, where

$$\delta = \sqrt{\sum_{i=1}^n c_i (1 - r_i/\bar{r})^2} \quad \text{Equation 3.2.3}$$

and

$$\bar{r} = \sum_{i=1}^n c_i r_i \quad \text{Equation 3.2.4}$$

where r_i is the atomic radius of element i , which can be obtained from ref. [46], c_i is its concentration, and \bar{r} is a weighted average of the atomic radii of the elements in the system. δ is therefore a measure of the comprehensive atomic size difference in a HEA across all its elements. The criterion for the formation of a solid solution in a HEA system has been determined as $\delta < 4.6$ [41], [43].

(iv) Valence Electron Concentration (VEC)

Similar to atomic size effects, the use of electron concentration as a parameter for structure prediction is a concept that has been borrowed from the Hume-Rothery rules for lower-order alloy systems. The main difference between the parameters discussed thus far and the electron concentration in predicting alloy structure is that while the former indicate whether or not a solid solution phase is likely to be stabilized, electron concentration can be used to predict the type of solid solution that will result if it is [36].

The VEC is one of two common measures of electron concentration, the other being the e/a ratio, which is the number of itinerant electrons per atom and which is often difficult to determine for transition metals. This and the fact that most HEAs studied to date have mainly consisted of transition metals has made the VEC the main measure of electron concentration for structure prediction in HEA. The VEC is defined as the total number of electrons occupying the valence band, including d-orbital electrons. For an alloy, it is merely the weighted average of the VEC of each of its constituent elements as seen in Equation 3.2.5. Table 3.2.2 shows the VEC criteria for the formation of FCC, BCC, or mixed solid solution structures as developed by Guo et al. [47].

$$VEC = \sum_{i=1}^n c_i (VEC)_i \quad \text{Equation 3.2.5}$$

Table 3.2.2. VEC criteria for structure prediction as determined by Guo et al. [47]

Structure	VEC Range
Single FCC SS	$VEC \geq 8$
Mixed FCC and BCC SS	$6.87 \leq VEC < 8$
Single BCC SS	$VEC < 6.87$

(v) Other Parameters

There seems to be good agreement between the various studies involving these parametric approaches regarding the parameters discussed so far and their influence on structure determination. In the following section, some additional parameters that have recently been proposed to help with element selection and the design of HEAs are presented. An additional approach is also seen here, where rather than focusing on parameters and criteria that promote random solid solution structures, some studies focus on predicting the formation of intermetallic phases and other ordered structures. While some of these might require further validation, some interesting ideas worth discussing are put forth throughout their development.

Comprehensive Electronegativity Difference, ΔX

The overall electronegativity between the different elements forming an alloy has been proposed by Dong et al. [48] to predict the formation of topologically close-packed (TCP) phases, which are a class of intermetallic phases that are often found in HEAs. This is based on the idea that the larger the difference in electronegativity between elements promotes the formation of intermetallic compounds. While the electronegativity difference between two elements is used as part of the Hume-Rothery rules to determine the extent of solid solubility of one element in another in binary system, a more comprehensive measure of the difference in electronegativity between elements is needed in more complex, higher-order systems such as HEAs. Accordingly, Equation 3.2.6 quantifies the electronegativity difference, ΔX , for multi-component alloy systems as

$$\Delta X = \sqrt{\sum_{i=1}^N c_i (X_i - \bar{X})^2} \quad \text{Equation 3.2.6}$$

$$\bar{X} = \sum_i^n c_i X_i \quad \text{Equation 3.2.7}$$

where X_i is the Pauling electronegativity of element i in a system of n elements, c_i is its concentration in at.%, and \bar{X} is the weighted average of the elements' individual electronegativities [46].

Based on a survey of various HEAs in literature that have been found to form TCP phases, it was determined that such phases will form when $\Delta X > 0.133$. Alloys containing significant amounts of Al, however, do not abide by this criterion [48].

The Competition between ΔS_{mix} and ΔH_{mix} , Ω

The parameter Ω (Equation 3.2.8 below) was proposed by Yang et al. [49] as a measure of the competition between ΔS_{mix} and ΔH_{mix} in stabilizing different types of structures in HEAs. The authors make the argument that ΔS_{mix} can be thought of as a driving force for solid solution formation, and that when it is large enough, it is able to overcome the ordering and/or segregation tendencies introduced by ΔH_{mix} . Accordingly, while increasing ΔS_{mix} promotes solid solution stabilization, ΔH_{mix} resists it and their relative contributions will determine the final structure. The entropy contribution is multiplied by T_m , which in this case is defined as the weighted average (by composition) of the melting temperatures of the alloy's constituent elements. The average melting temperature was chosen since that apart from solid-state phase transformations, phases will usually form close to the melting temperature of the alloy.

The effect of temperature on Ω should be emphasized, since it plays a major role in determining the significance of the entropic contribution. At higher temperatures, the $T_m \Delta S_{\text{mix}}$ is more likely to approach the same order of magnitude as $|\Delta H_{\text{mix}}|$ than at lower ones. This means that as temperature increases, ΔS_{mix} is more likely to be able to prevent the ordering effects of ΔH_{mix} and stabilize solid solution phases.

$$\Omega = \frac{T_m \Delta S_{mix}}{|\Delta H_{mix}|} \quad \text{Equation 3.2.8}$$

It was found that solid solutions are likely to form when $1.1 \leq \Omega \leq 229.8$, however, only when $0.8\% \leq \delta \leq 6.6\%$, where δ is the atomic size difference parameter (Equation 3.2.3). This correlation between Ω and δ in stabilizing solid solutions highlights the interdependencies that exist between the different parameters used for structure prediction, which will be discussed in more detail at the end of this section. Moreover, Ω should not be confused with Ω_{ij} used in the calculation of ΔH_{mix} .

Enthalpy and Entropy of Formation for Intermetallic Phases, ΔH_{IM} and ΔS_{IM}

Senkov et al. [50] later argued against the premise on which the Ω parameter was developed stating that ΔH_{mix} and ΔS_{mix} work synergistically to minimize the Gibbs free energy of a solid solution phase rather than being in competition with one another. By replacing T_m in Equation 3.2.9 with T_A , the annealing temperatures of the alloys selected for the study, the authors showed that Ω does not work well in determining the final equilibrium structure of HEAs.

Instead, the authors propose a new criterion based on the enthalpy and entropy of formation of intermetallic phases, ΔH_{IM} and ΔS_{IM} respectively. The condition for solid solution formation is

$$\kappa_1^{cr} > \kappa_1 = \Delta H_{IM} / \Delta H_{mix} \quad \text{Equation 3.2.9}$$

where

$$\kappa_1^{cr} = -\frac{T \Delta S_{mix}}{\Delta H_{mix}} (1 - \kappa_2) + 1 \quad \text{Equation 3.2.10}$$

$$\kappa_2 = \Delta S_{IM} / \Delta S_{mix} \quad \text{Equation 3.2.11}$$

$$\Delta H_{IM} = \sum_{i < j} 4H_{ij}^{IM} c_i c_j \quad \text{Equation 3.2.12}$$

The above equations assume a linear relationship between ΔH_{IM} and ΔH_{mix} as well as ΔS_{IM} and ΔS_{mix} . Put in simpler terms, Equation 3.2.9 is based on the idea that a solid solution phase will be stabilized if its ΔG_{mix} is less than ΔG_{IM} , which is the Gibbs free energy of formation of an intermetallic phase. Equation 3.2.12 for the calculation of ΔH_{IM} is very similar in form to Equation 3.2.1 and the values of H_{ij}^{IM} can be obtained from ref. [51]. As shown in the study, this criterion works well in predicting the formation of solid solution versus mixed solid solution and intermetallic structures of HEAs, based on 45 cast and annealed alloys.

(vi) Correlations between Structure Prediction Parameters and their Evaluation

It should be emphasized that the parametric approaches discussed in (i) through (v) are usually interdependent. The same plots that have been developed to determine the upper and lower bound values necessary for the stabilization of certain types of phases can also be used to show

the correlations between the developed criteria. These plots map the different structures obtained at different combinations of the above parameters such as that shown in Fig. 3.2.1.

Despite the relative simplicity associated with parametric approaches such as those discussed above, some concerns arise regarding their accuracy and validity, which warrants that they should be used with caution. For instance, the accuracy of the structure predicted is sometimes system-dependent, meaning that some approaches work better for certain alloy systems than others. An example of this is the $\Delta X > 0.133$ criterion for TCP phase formation, which does not work well at high concentrations of Al [48]. Moreover, the criteria stated above were mainly developed using as-cast alloys and their structures, which are often not the equilibrium phases. Accordingly, when Wang et al. [52] evaluated the parameters in (i) through (iv) for annealed alloys instead, their allowable ranges for specific structure stabilization were found to be different. The contrast between as cast and annealed values is highlighted in Table 3.2.3. The most notable differences appear to be in the narrowing of the allowable range of ΔH_{mix} and δ , such that the conditions for achieving a solid solution phase are more strict for the alloy in the annealed state compared to the as-cast condition. The contrast between both conditions is illustrated in Fig. 3.2.1 (a) and (b), which compare the criteria for solid solution formation in each case. It is therefore clear that the type of processing that a HEA will undergo affects the phase selection rules and should be taken into account when developing such parameters and determining their associated rules. Finally, it should be noted that the accuracy of such parameters and criteria for structure prediction is highly dependent on the number of different alloys considered in their development. For that reason, it is important that as new alloys and alloy systems emerge, the criteria developed thus far should be continuously validated and updated as needed.

Table 3.2.3. Difference in phase selection rules between as cast and annealed HEAs [52]

Parameter	As Cast Alloy	Annealed Alloy
ΔS_{mix}	> 13.38	> 13.38
ΔH_{mix}	$-15 \text{ kJ/mol} < \Delta H_{\text{mix}} < 5 \text{ kJ/mol}$	$\Delta H_{\text{mix}} \geq -7.5 \text{ kJ/mol}$
δ	$\leq 6.6\%$	$< 3.3\%$
VEC	FCC: $\text{VEC} \geq 8.0$ BCC: $\text{VEC} < 6.87$	FCC: $\text{VEC} \geq 7.8$ BCC: $\text{VEC} < 6.0$

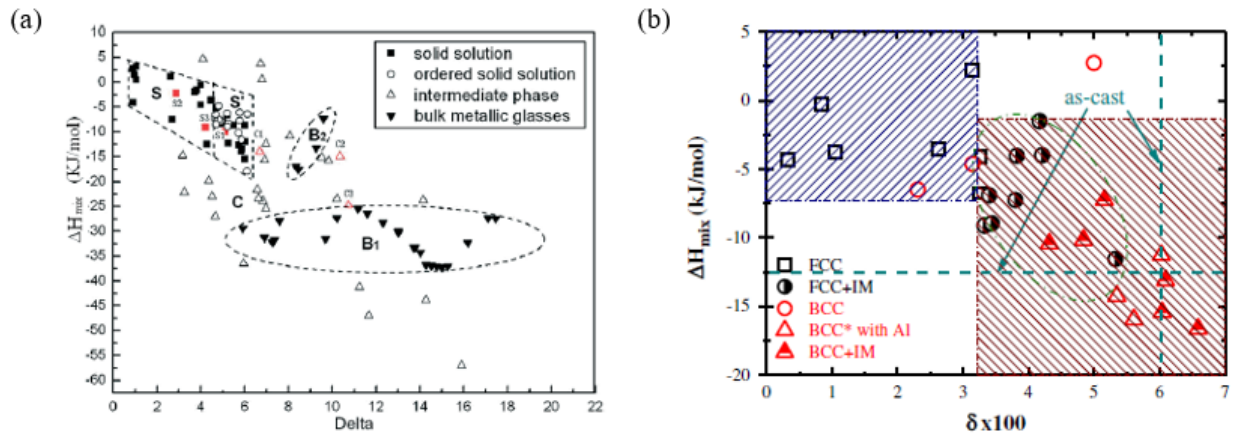


Fig. 3.2.1. Structural dependence on ΔH_{mix} and δ for (a) as cast [41] and (b) annealed HEAs [51]

3.2.2. The Calculation of Phase Diagrams (CALPHAD) Method

While the parametric approaches discussed above offer a quick solution to predict the type of structure that would result from a given combination of elements, the information these approaches provide is still very limited. On the other hand, phase diagrams can provide extensive information relating to a material's phase stabilities, solubility ranges, and transition temperatures and therefore, they have been the primary means of alloy design in conventional metallurgy. Accordingly, the ability to obtain phase diagrams for HEAs is of great value to their design process. Traditionally, phase diagrams are constructed through conducting a series of experiments in which the material composition is varied, and where the system is allowed to equilibrate followed by the thermal and structural characterization of the produced samples. However, for multi-component alloy systems, this becomes infeasible in terms of the extensive amounts of material and time resources needed to produce a comprehensive phase diagram. Computational methods for generating phase diagrams overcome this problem and accordingly facilitate and accelerate the exploration of different HEA systems [38].

The Calculation of Phase Diagrams (CALPHAD) method [23] has been central to generating computational phase diagrams of HEAs. Contrary to what its name implies, the CALPHAD method is not limited to the generation of phase diagrams but can also be used to calculate phase fractions and their compositions, as well as various thermodynamic properties of a given alloy under a given set of conditions. Its flexibility and the extensive information that can be extracted using the CALPHAD method have made it central to the exploration of the large compositional search space available for HEAs. Accordingly, it has become a key element in HEA research. The CALPHAD approach depends on computational thermodynamics and the basis of the approach, the details of its models, and the required software and databases needed to carry out its calculations will be discussed throughout this section.

3.2.2.1. Overview of the CALPHAD Method

The CALPHAD method relies on the fact that the equilibrium state of a system occurs when it attains its lowest possible Gibbs energy. Accordingly, a minimization of the total Gibbs energy function for a given alloy system can be used to calculate its equilibrium state given that the individual Gibbs energy functions of its different phases are known. This requires mathematical models for the different types of phases in alloy systems which accurately represent the variation of their Gibbs energy as a function of temperature, pressure, and composition. To achieve this, these models consist of terms and parameters that describe the various contributions of the phases to the overall Gibbs energy of the system. These parameters are determined via an optimization procedure using available experimental data as input such that the developed models are able to reproduce the original input data. Where experimental data is lacking, input to the optimization process can also be obtained from first principles calculations such as Density Functional Theory (DFT). Once reliable models and parameters are determined, the thermodynamic description of the system is complete, and it can be used to predict the structures and thermodynamic properties of alloys outside the temperature and compositional ranges of the original input data. This becomes especially important for HEAs since their available experimental data is scarce and the abundance of such thermodynamic descriptions for their lower-order binary and ternary subsystems makes it possible to predict their structures and properties via extrapolation [36], [38].

3.2.2.2. CALPHAD Software Packages and Thermodynamic Databases

To carry out CALPHAD calculations typically requires a CALPHAD software package and a thermodynamic database. The thermodynamic database contains the thermodynamic description of a system including the mathematical models of the Gibbs energy functions of its phases as well as the optimized values of the model parameters. The software should be able to read the database and perform the Gibbs energy minimization to calculate the equilibrium state of the selected system. CALPHAD software can also be used for database development and assessment. Several commercial software packages are available for this purpose such as ThermoCalc [53] and Pandat [54], as well as the open-source software used in this study, namely OpenCalphad [55], [56].

OpenCalphad is the first high-quality open-source software that encompasses the multiple facets of the CALPHAD method. Using open-source software has several advantages including security, quality, and customizability. However, one of their major advantages is that they are free, which makes important tools, like CALPHAD, accessible to a broader range of researchers and academics without the need to pay the high prices associated with proprietary software licenses, support, and upgrades [57]. Like other CALPHAD software, OpenCalphad uses a minimization algorithm to determine a given system's equilibrium state (at its minimum Gibbs energy) under set conditions of composition, temperature, and pressure. To do this, a set of linear equations is formulated, where each stable phase is modeled by one equation. The algorithm then differentiates

between the stable and unstable phases based on the selected conditions, which represent the constraints on the different parameters, until the calculation converges. For the algorithm to be successful, it should also result in physically meaningful quantities. For example, a phase amount cannot be negative and any phase with such an amount should be considered unstable. A more detailed account of the minimization procedure can be found in ref [58].

The development and optimization of thermodynamic databases is an important but difficult task that requires extensive knowledge of experimental methods and thermodynamic theory. This is because the quality of the optimization input comprised of the experimental data and first-principles results needs rigorous evaluation to ensure the accuracy of the optimized parameters and consequently the CALPHAD results [59]. Fig. 3.2.2 illustrates the process of a thermodynamic database development and optimization. The mc_ni.tdb open database [60], used in the current study, is an example of the thermodynamic databases needed to carry out CALPHAD analysis. While several commercial databases are currently available for the CALPHAD modelling of HEAs such as the TCHEA1 [61] and PanHEA [54], these can only be read using their corresponding proprietary software which limits their accessibility. Open databases have the same advantages as open-source software mentioned above and accordingly their availability and development is as important. While the mc_ni.tdb has not been specifically developed for HEA calculations, it is optimized and tested for another class of multi-component alloys, namely Ni super-alloys. Accordingly, it contains all the binary and ternary interaction parameters of the following elements: Ni; Al; B; C; Co; Cr; Cu; Fe; Hf; La; Mn; Mo; N; Nb; Ni; O; S; Si; Ti; V; W; Y; Zr; and should therefore have the appropriate extrapolation capabilities needed for HEA systems consisting of different combinations of these elements, including the CoCrFeNiTi system.

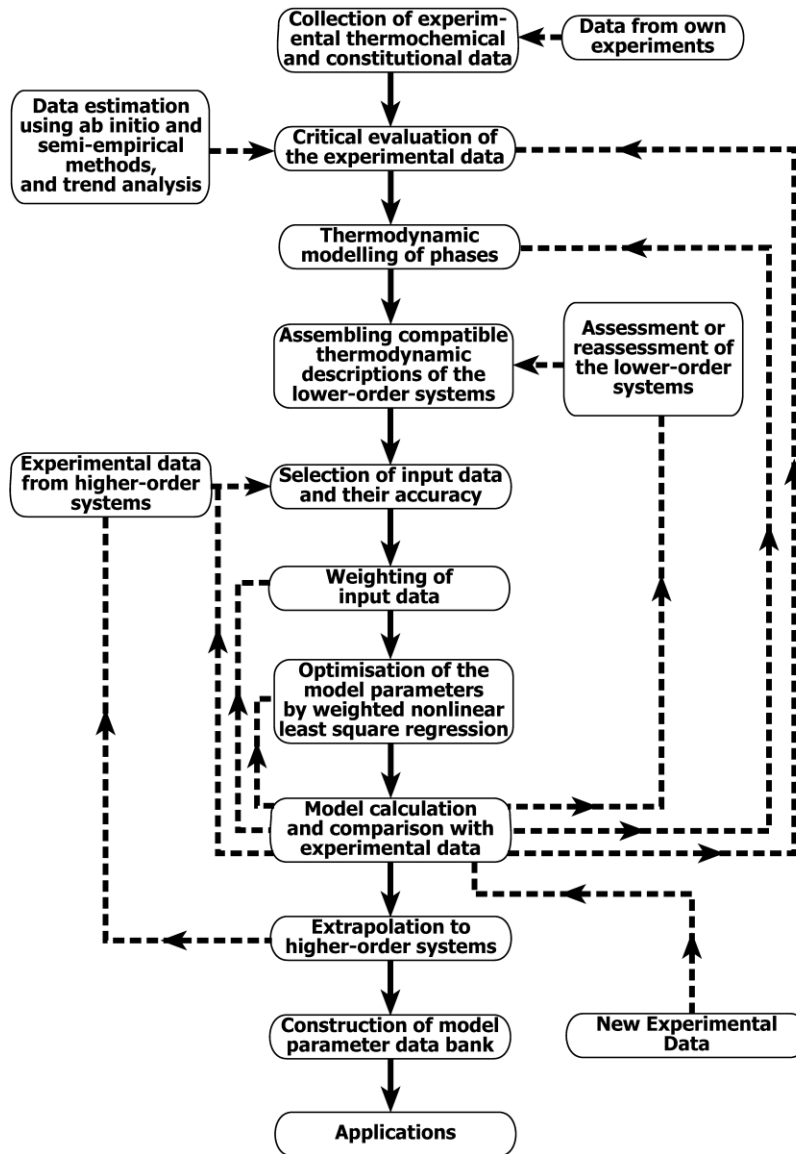


Fig. 3.2.2. Thermodynamic database development and optimization process [59].

3.2.2.3. Phase Models

Mathematical models that accurately describe the changes in the Gibbs free energy of the individual phases present in HEAs in the desired composition and temperature ranges are necessary to obtain accurate and realistic CALPHAD results. Solid solution and topologically close-packed (TCP) intermetallic phases are of particular importance to the study of HEAs and accordingly, in this section their respective models will be presented. This is also important to further illustrate the thermodynamic theory of multicomponent systems including HEAs.

Successful models will usually satisfy three main criteria, where the Gibbs energy function of a phase: (i) is physically meaningful; (ii) can be used to extrapolate properties of higher-order systems from lower-order ones and; (iii) is compatible with other models used in a thermodynamic

database if existing results are to be augmented with new ones [59]. For CALPHAD, sub-regular solution models are typically used for substitutional solid solution phases such as FCC and BCC phases. On the other hand, sublattice models, and especially the Compound Energy Formalism (CEF) [62], are needed for modelling many of the intermetallic phases found in HEAs.

(i) The Subregular Solution Model

Real alloys are better represented as regular and subregular solutions, which are types of non-ideal solutions, and therefore Equation 2.2.5 and Equation 2.2.7 insufficiently describe their properties. The main difference is in the excess Gibbs energy contribution, which results from their deviation from ideal behavior and which needs to be accounted for mathematically. Accordingly, the subregular solution model is typically used to represent the Gibbs energy of non-ideal solid solution phases such as FCC and BCC as a function of temperature, pressure, and composition. This model assumes that the elements are randomly and homogeneously distributed in the solution lattice, with no preferential lattice sites for a given element. According to this model, the molar Gibbs energy function of a solid solution phase ϕ is given by

$$G_m^\phi = G_{m,ref}^\phi + G_{m,id}^\phi + G_{m,ex}^\phi + G_{m,mag}^\phi \quad \text{Equation 3.2.13}$$

The subscript m indicates that the given quantities are molar quantities. The $G_{m,ref}^\phi$ term is the elemental reference state of the system and can be obtained from the molar Gibbs energy $G_{m,i}^\phi$ of each element i with structure ϕ using Equation 3.2.14. The $G_{m,id}^\phi$ is the ideal mixing contribution to G_m^ϕ previously given by Equation 2.2.7. The $G_{m,ex}^\phi$ and $G_{m,mag}^\phi$ terms represent excess quantities and are a measure of the deviation from the ideal solution behavior due to non-magnetic and magnetic contributions, respectively. The $G_{m,mag}^\phi$ should only be considered if any magnetic ordering exists in the alloy [36].

$$G_{m,ref}^\phi = \sum_i^n x_i G_{m,i}^\phi \quad \text{Equation 3.2.14}$$

Equation 2.3.15 is an expansion of the non-magnetic excess term, $G_{m,ex}^\phi$, for a quinary alloy system, since the minimum number of elements in a HEA is expected to be five. The parameters $L_{i,j}^\phi$, $L_{i,j,k}^\phi$, $L_{i,j,k,l}^\phi$, and $L_{i,j,k,l,m}^\phi$ represent the binary, ternary, quaternary, and quinary interactions between the alloy's elements, respectively, and are obtained by the optimization procedure previously discussed. It should be noted however, that for databases to be used with multicomponent systems, it is often sufficient to only optimize the binary and ternary interaction terms as higher-order interactions (such quaternary and quinary interactions) have negligible contributions and can therefore be ignored [36].

$$G_{m,ex}^\phi = \sum_{i \neq j} x_i x_j L_{i,j}^\phi + \sum_{i \neq j \neq k} x_i x_j x_k L_{i,j,k}^\phi + \sum_{i \neq j \neq k \neq l} x_i x_j x_k x_l L_{i,j,k,l}^\phi + x_i x_j x_k x_l x_m L_{i,j,k,l,m}^\phi$$

$$\text{Equation 3.2.15}$$

Both regular and subregular solutions can be treated using Equation 3.2.13 and Equation 3.2.15. However, the distinction between these two types of solutions appears in further expanding the binary and ternary interaction parameters $L_{i,j}^{\phi}$ and $L_{i,j,k}^{\phi}$ (higher-order interactions will be ignored onwards). In the regular solution model, composition-independent interaction parameters are assumed, while the sub-regular solution model is more involved in terms of the composition dependencies of its interaction parameters [23]. The sub-regular model better describes the behavior of non-ideal solutions compared to the regular solution model and is accordingly more widely used for CALPHAD purposes.

(ii) The Compound Energy Formalism (CEF)

Overview

Sublattice phases consist of two or more sublattices, where the phase constituents can occupy lattice sites of either sublattice. Contrary to the subregular solution model, the mixing of the phase constituents is not necessarily random and there can be a preferential occupation of a certain sublattice by a given constituent, however, random mixing is assumed within each sublattice. Fig. 3.2.3 illustrates this concept, where a BCC structure is shown to have its body-center sites occupied by one type of atoms and the corner positions occupied by another [23].

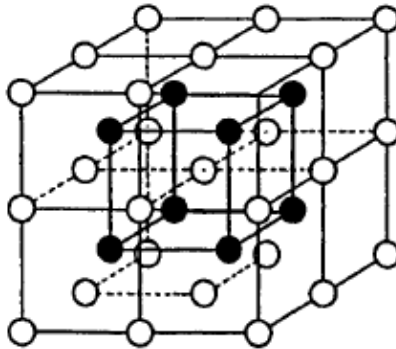


Fig. 3.2.3. Preferential occupation of the body-center and corner sublattice sites in a sublattice phase with a BCC structure [23].

While the subregular model can effectively model non-ideal solid solution phases, it fails to describe the thermodynamic behavior of solid solutions with multiple sublattices, which require models that can capture the interactions between the elements on the different sublattices. One of the most important methods used to approach this problem is the Compound Energy Formalism [62], which has consequently become a central part of CALPHAD modelling [59]. The CEF is a general framework that encompasses various models for different types of sublattice solution phases, such as interstitial solid solutions and reciprocal solution phases, the latter being commonly found in HEAs [17], [63], [64].

In the CEF, the general notation of a sublattice solution phase is $(A,B)_a(C,D)_b$, where A and B occupy the first sublattice and C and D and occupy the second. The subscripts a and b are the stoichiometric coefficients and also denote a stoichiometric constraint, meaning that the degrees

of freedom of the composition are two rather than three. In other words, the concentration of one element cannot be changed if it is not present on all the sublattices [62], [65]. Sublattice phases can include more than two components and sublattices than those illustrated in the case above, however, the 2-sublattice, quaternary solution is useful for demonstrating the basics of the thermodynamic modeling of these phases.

Concentration dependent interactions are central to sublattice models, including the CEF, and require the definition of site fractions. Site fractions quantify the occupancy of a sublattice by a particular species. The site fraction y_i^s of species i on sublattice s is defined as

$$y_i^s = \frac{n_i^s}{N^s} \quad \text{Equation 3.2.16}$$

where n_i^s is the number of sublattice sites occupied by species i and N^s is the total number of sublattice sites [23]. In the CEF, the species occupying a sublattice can be anything from an atom to an ion or vacancy and these form the constituents of the sublattice [62]. However, for the purposes of HEAs, constituents will usually be atoms of elements, which will be the focus of the remaining part of this section.

Reciprocal solution phases are compound phases that can exist over a range of compositions and therefore are solutions rather than stoichiometric compounds. However, contrary to substitutional solid solutions, reciprocal solution phases abide by the stoichiometric constraint explained above. The intermetallic phases found in HEAs such as the sigma (σ) and Laves phases belong to this category of phases and are therefore modeled using the CEF. Accordingly, in the remainder of this section, the discussion of the CEF will focus on models for reciprocal solution phases [23].

When a sublattice of a reciprocal solid solution is occupied by a single component, end-member compounds are obtained. Endmembers are important because they define the composition space of a sublattice solution. In the $(A,B)_a(C,D)_b$ example, the end-members would be A_aC_b , A_aD_b , B_aC_b , and B_aD_b . The composition space for this phase is, therefore, enclosed within a square with each of the end-member compounds at a corner of the square. Moreover, the CEF uses the Gibbs energy of the endmembers ${}^\circ G_{end}$ to define a reference surface, which is the first step in the formulation of the Gibbs energy of the whole solution. The Gibbs energy reference surface for a reciprocal solution phase is illustrated in Fig. 3.2.4 and is given by the following equation [62]

$$G_m^{s.r.} = \sum {}^\circ G_{end} \prod y_i^s \quad \text{Equation 3.2.17}$$

$$G_m = y_A y_C {}^\circ G_{A_a C_b} + y_A y_D {}^\circ G_{A_a D_b} + y_B y_C {}^\circ G_{B_a C_b} + y_B y_D {}^\circ G_{B_a D_b} \\ + RT [a y_A \ln y_A + a y_B \ln y_B + b y_C \ln y_C + b y_D \ln y_D] + G_m^E$$

$$\text{Equation 3.2.18}$$

Equation 3.2.18 gives the total molar Gibbs energy G_m for a reciprocal solution phase. The first four terms represent the Gibbs energy reference surface and are obtained by expanding Equation 3.2.17. The following term is the entropic contribution in terms of the site fractions of the various components on the different sublattices. The final term, G_m^E , is the excess Gibbs energy, which is dependent on the interactions of the components with their neighbors on the same and different sublattices. A detailed discussion of the excess Gibbs energy in reciprocal solid solutions can be found in ref. [65].

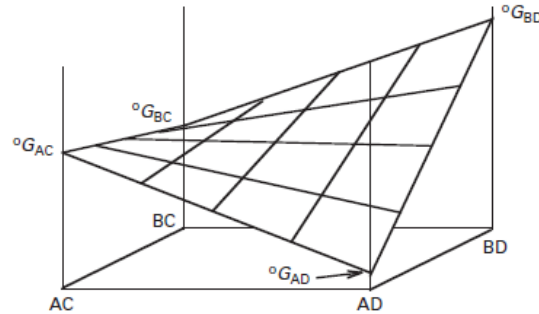


Fig. 3.2.4. The Gibbs energy reference surface for a $(A,B)_a(C,D)_b$ reciprocal solution phase. The composition space is the square defined by the endmember AC, AD, BC, and BD [65].

Example: The Sigma (σ) Phase

As an example, to illustrate how sublattice models can be applied, the σ phase is considered. The σ phase is an intermetallic phase that precipitates in many alloy systems such as stainless steels [66] as well as HEAs. Several studies have emerged attempting to understand and predict the formation of the σ phase in HEAs [63], [67] due to its frequent encounter in HEA studies (including those of the CoCrFeNiTi system of interest) and the embrittlement it causes.

The σ phase has 30 atoms in its unit cell, which occupy five sublattices in the ratio 2:4:8:8:8. For multicomponent systems like HEAs, modelling the interactions across all five sublattices using CALPHAD would be an impossible task due to the massive number of variables that arises. Accordingly, some simplifications are made, where certain sublattices can be joined. In the case of a binary system with elements A and B, the σ phase is considered as $(A,B)_{16}(A,B)_{10}(B)_4$ or $(A,B)_{16}(A)_{10}(B)_4$ depending on the solubility of the elements on each sublattice [23].

The simplified structure can be further extended to include more elements (in the case of HEAs, five or more) and similar simplifications are utilized in the mc_ni.tdb database used in this study. Another interesting observation is that in a two-sublattice system, if the second sublattice is completely occupied by vacancies, the sublattice model reduces to the subregular solution model described previously. The mc_ni.tdb database also uses sublattice models for FCC and BCC solid solution phases with the second sublattice fully occupied by vacancies.

3.3. The CoCrFeNiTi System

High entropy alloys of the CoCrFeNiTi system have become in recent years prime candidates for developing HEAs that are both strong and ductile [13]. At low concentrations of Ti, these alloys exhibit a primary FCC solid solution phase, which increases their ductility compared to other HEAs which form primarily BCC structures. The main challenge the CoCrFeNiTi alloys pose to this goal of increased ductility with increasing strength is their tendency to form a wide range of hard and brittle intermetallic phases, which embrittle their ductile FCC solid solution structures. In this section, a review of the literature available on the CoCrFeNiTi HEA system, the mechanisms of their intermetallic phase formation, and the means by which these phases embrittle the alloys is presented.

Interest in the CoCrFeNiTi system stems from the study of the AlCoCrFeNiTi and AlCoCrCuFeNiTi alloys, which were found to possess excellent compressive strengths but performed very poorly in terms of ductility and fracture strain. This was attributed to the BCC structure of these alloys, which is stabilized by the presence of Al and Ti, both of which are known to be BCC stabilizers as well as solid solution strengtheners [68], [69]. Investigations of the AlCoCrFeNiTi HEAs, revealed that when the concentration of Al is kept at zero and the content of Ti is limited Ti (ie. CoCrFeNiTi), the alloy will form FCC-dominated structures rather than BCC, which increases the resulting alloys' ductility. Accordingly, the CoCrFeNiTi system has been the focus of several studies targeting strong and ductile HEAs [9].

3.3.1. Dendritic Microstructures, Elemental Segregation, and Anisotropic Properties

An analysis of the available literature on the CoCrFeNiTi HEA system reveals that the most common method of alloy fabrication employed in these studies is the use of melting and casting techniques, which are simple and efficient. However, despite many precautions taken to ensure alloy homogeneity, dendritic microstructures with significant elemental segregation are typically obtained, which result in an anisotropy of properties in the alloys produced.

Arc melting is one of the most common methods used for alloy fabrication in CoCrFeNiTi studies. The typical microstructure obtained using this technique is a dendritic structure with a Ti-deficient, FCC-structured dendritic region and a Ti-rich interdendrite consisting of a primary FCC-structured phase and intermetallic secondary phases as shown in Fig. 3.3.1 (b). As a result of the inhomogeneity of the microstructure, the dendritic and interdendritic regions also tend to exhibit different hardness values indicating an anisotropy of the mechanical properties in the as-cast alloys [9], [11], [13], [17].

Several explanations have been offered to explain the obtained microstructures. One such explanation is the size mismatch between Ti and the alloy's remaining elements. From a thermodynamic standpoint, the large negative ΔH_{mix} between Ni and Ti has been attributed to the formation of a (Ni,Ti)-rich phase in the interdendrites. This consequently leads to high concentrations of Cr and Fe in regions where Ni and Ti are depleted and the formation of a (Cr,Fe)-

rich phase in the dendrites. The effect of Ti is clear when the as-cast microstructures of CoCrFeNiTi alloys are compared to that of CoCrFeNiTi₀ (ie. CoCrFeNi) shown in Fig. 3.3.1 (a). The simplicity of this alloy's structure in the absence of Ti can be explained by the similarity of the atomic sizes of the elements as well as the absence of a strong negative or positive ΔH_{mix} between them [9], [17].

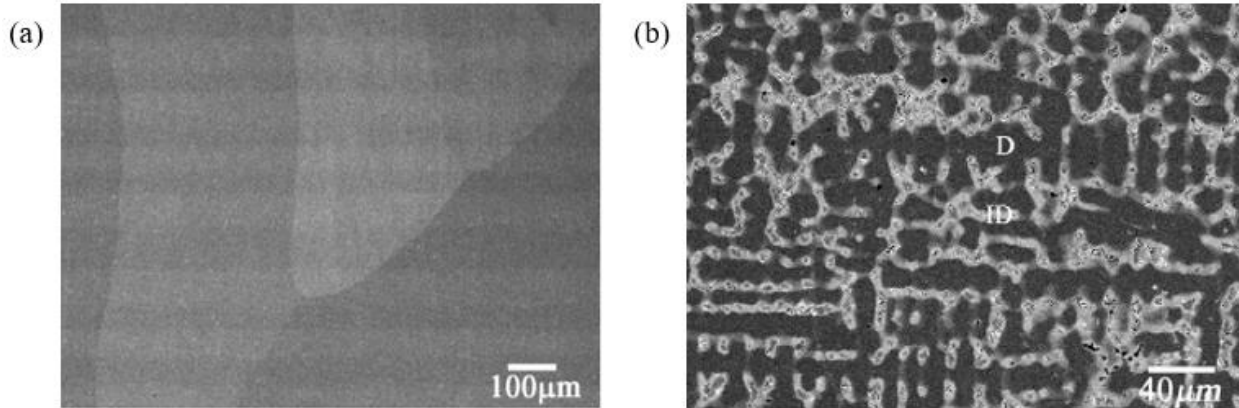


Fig. 3.3.1. SEM microstructure image of as-cast (a) CoCrFeNiTi₀ (ie. CoCrFeNi) [9] and (b) SEM microstructure image of CoCrFeNiTi_{0.3} showing the alloy's dendritic microstructure. The dendritic region is labeled as D and the interdendrite as ID [17].

3.3.2. Intermetallic Phases in the CoCrFeNiTi System

3.3.2.1. Structural Inheritance

The types of primary and secondary phases that appear in a HEA often depend on three main factors. These are: the elements present and structural inheritance; the concentration of each element i.e. alloy composition; and the selected fabrication and processing route. As previously discussed in section 3.3.1, the types of elements present and their interactions can result in either single or multiple SS phases and/or IM compounds. An interesting concept that should be introduced in the discussion of the effect of elements on the resulting structure of alloys is structural inheritance. Structural inheritance suggests that the IM phases that form in complex, higher-order systems such as those of HEAs are inherited from their lower-order binary and ternary phase diagrams. Structural inheritance has been thoroughly explored by Otto et al. [44], who used a combination of experimental and computational approaches to compare the phases detected in fabricated HEAs to those found in the binary phase diagrams of each pair of their constituent elements. The authors showed that IM phases present in binary systems are likely to appear in higher-order systems containing the same elements. Another important outcome of this work is the evidence it provides in support of the notion discussed in section 3.1.2, that although the high entropy of mixing of some HEAs can sometimes suppress the formation of intermetallic phases, it is in most cases unlikely, especially if they are common in lower-order systems of the same elements.

Structural inheritance was also later investigated by Tsai et al. [70], who examined HEAs literature and applied a statistical approach to assess the role of structural inheritance in the formation of IM phases in HEA alloys. The authors developed a database of 142 HEAs containing intermetallic phases (excluding those with compositional similarity) and it was found that in 90% of the alloys surveyed, the existing IM phases were present in their binary phase diagrams. In the remaining 10%, the IM phases formed were found to be in common with the alloys' ternary phase diagrams, which indicates that these phases are ternary in nature, meaning they require 3 different elements for the structure to form.

3.3.2.2. Important Intermetallic Phases and their Effect on Alloy Properties

The remainder of this section will focus on the most common types of intermetallic phases that have been observed in the CoCrFeNiTi HEA system. While it is beneficial to examine similar phases in superalloys, it should be noted that the mechanisms of intermetallic phase formation in HEAs are often very different than those in superalloys [63]. Accordingly, the discussion below will only refer to superalloys in terms of the structures of intermetallic phases that are common between HEAs and these alloys, but not their precipitation/formation mechanisms.

(i) Topologically Close-Packed (TCP) Phases

TCP phases are a large class of intermetallic phases with complex structures and properties. TCP phases often cause the deterioration of alloy mechanical properties especially in terms of plasticity and accordingly, are generally undesirable [25]. Among the most important TCP phases are the sigma (σ), Laves, and mu (μ) phases, which have been observed in various HEA systems [64], including the CoCrFeNiTi system.

The Sigma (σ) Phase

The σ phase has been briefly introduced in section 3.2.2.3, in the discussion pertaining to phase models. The σ phase is an AB type intermetallic phase with a Body-Centered Tetragonal (BCT) structure, where A elements typically belong to groups 5-7 while B elements typically belong to groups 7-10 of the periodic table [67], [71]. Similar to other TCP phases, the σ phase can have a detrimental effect on alloy properties and for that reason, it has been of major interest to the study of superalloys such as Ni-based superalloys [72]. This interest has shifted to also encompass the frequent occurrence of the σ phase in multiple HEA systems, including the CoCrFeNiTi system, and its significant impact on alloy properties [48].

The σ phase was observed by Fu et al. [10] in a Co_{0.5}FeNiCrTi_{0.5} HEA, which was fabricated using mechanical alloying (MA) followed by spark plasma sintering (SPS). The mechanical alloying was achieved via a combination of dry and wet ball milling, which resulted in a mixed FCC and BCC solid solution structure. Following consolidation by SPS, the structure of the alloy was found to consist of an FCC solid solution phase and a secondary σ phase, which led to the suggestion that the BCC phase formed during the non-equilibrium milling process was a metastable phase that evolved into the more stable σ phase during sintering. The alloy was tested

under compression and was found to exhibit a good yield and compressive strength compared to similar alloys produced by casting. The alloy was also found to possess the highest Vickers hardness compared to CuNiCoZnAlTi and CuCoFeCrAl also produced by MA. However, the compression test also shows that the alloy fails without undergoing plastic deformation. This is a typical effect of the presence of a σ phase, where its presence can generally improve the strength and hardness of an alloy, but also leads to a significant loss of ductility limiting the possibility of its use for structural applications.

The Laves Phases

The Laves phases are also a type of TCP phases that are commonly observed in HEAs. Laves phases are A_2B phases with cubic (C15) or hexagonal (C14 and C36) structures [38]. The formation of Laves phases in CoCrFeNiTi alloys has also been reported and will be discussed in a later section of this thesis.

(ii) Geometrically Close-Packed (GCP) Phases

Contrary to TCP phases, GCP phases are a class of intermetallic phases that are often desirable due to their strengthening effect, especially at elevated temperatures. The GCP phases of interest to this study are those with an A_3B structure such as the gamma prime (γ'); gamma double prime (γ''); eta (η); and the delta (δ) phase (not to be confused with the comprehensive atomic size difference parameter). The coordination number of the atoms in these phases is 12 and their crystal structures are shown in Fig. 3.3.2 [73]. The notation used to label the structures in Fig. 3.3.2 is called the Strukturbericht Designation [74], which is a common method for defining crystal structures. According to the Strukturbericht method, the γ' phase has the $L1_2$ structure; the η phase has the DO_{24} structure; and the δ phase the DO_a structure, which are shown in Fig. 3.3.2.

The Gamma Prime (γ') Phase

In addition to its major strengthening role in Ni superalloys [25], the γ' phase has been frequently observed in the CoCrFeNiTi HEA system. One important report of the presence of the γ' in CoCrFeNiTi HEAs is that by Shun et al. [17], who studied the formation of multi-elemental nanoparticles within the FCC matrices of four HEAs: CoCrFeNiAl_{0.3}; CoCrFeNiTi_{0.3}; CoCrFeNiMo_{0.3}; and CoCrFeNiAl_{0.3} Mo_{0.1}. Since the present work is focused on the CoCrFeNiTi system, only results pertaining to the CoCrFeNiTi_{0.3} alloy will be discussed herein. For this alloy, it was found that secondary intermetallic phases precipitate in the form of nanoparticles within the primary FCC phase in the as-cast state. While the large negative mixing enthalpy between Ni and Ti (-35 kJ/mol) promotes the formation of intermetallic phases, the formation of nanoparticles was attributed to the sluggish diffusion effect, which hinders the growth of the precipitated phase. The nanoparticles were found to have either an ordered or disordered structure depending on the local Ti concentration in the location of their formation (recall from Fig. 3.3.1 the dendritic microstructure of the CoCrFeNiTi_{0.3} alloy). The authors argue that a minimum concentration of 6.25 at. % Ti and 25 at. % Ni is required for ordering to occur due to certain considerations for the

symmetry of the structure. Accordingly, nanoparticles formed in the dendritic regions exhibit a disordered FCC solid solution structure (designated as the γ phase) since the condition for ordering is not met. On the other hand, the nanoparticles in the Ti-rich interdendritic regions were revealed by the selected area diffraction (SAD) pattern to possess a $L1_2$ ordered structure, which is the γ' intermetallic phase.

To further understand the structure and evolution of the γ' phase in CoCrFeNiTi HEAs, Han et al. [14] explored the aging behaviour of the γ' phase in a CoCrFeNiTi_{0.2} alloy both experimentally and computationally through first principles calculations. Samples of the alloy were produced using arc melting and were then subjected to a solutionizing heat treatment followed by aging for 5 minutes, 1 hour, and 24 hours at 1073 K. TEM analysis revealed an FCC solid solution matrix with $L1_2$ -structured nanoparticles i.e. γ' . Atomic probe tomography (APT) revealed that the γ' nanoparticles were composed primarily of Ni and Ti, contained some Co, and had very low concentrations of Fe and Cr. The concentration of Ni and Ti was found to be almost constant with increasing aging time, however, Fe and Cr were eventually incorporated into the structure of the γ' nanoparticles at 24 hours. It was suggested that the γ' phase evolves from (Co,Ni)₃Ti to (Co,Fe,Cr,Ni)₃Ti over the 24 hours of aging. First principles calculations showed that the formation energies for incorporating Fe and Cr into the Ni sublattice are much higher than that of Co, which the authors suggest as an explanation for the exceptionally low concentrations of Fe and Cr in the γ' phase. Finally, the effect of the changes occurring in the γ' phase on the mechanical properties of the alloy was considered, and the sample aged for 1 hour exhibited the highest hardness value compared to that aged for 5 minutes and 24 hours.

The Eta (η) Phase

The η phase is a Ni₃Ti-type phase with the D0₂₄ structure shown in Fig. 3.3.2. It evolves from the γ' phase at temperatures above 750°C in Ni-superalloys, but its strengthening effect is not as significant as that of the γ' phase. Although it does not directly lead to a deterioration of mechanical properties, the depletion of Ni from the alloy matrix that occurs as a result of the formation of the η phase makes the alloy prone to the precipitation of undesirable TCP phases, such as σ and Laves phases [71]. Similar behavior has been observed in CoCrFeNiTi HEAs, where the simultaneous precipitation of η and σ phases and the formation of a duplex η + σ phase has been reported in several studies. While the precipitation of these phases has a strengthening effect, that is usually reflected in an increase in the hardness of the alloys in which they form, this is usually accompanied by a considerable reduction in ductility.

This effect was observed in a study by Hung et al. [75], who investigated the effect of reducing the concentration of Co in Co_xCrFeNiTi_{0.3} (x=1.0, 0.8, 0.6) on its microstructure and mechanical properties. The main motivation for the reduction of Co content was to reduce the cost of the alloy as Co is the most expensive among the constituent elements of the CoCrFeNiTi HEAs. The alloys were produced via arc melting and all three exhibited a dendritic microstructure with a single FCC solid solution in the dendrite, that is slightly depleted of Ti. The structure of the ID

consisted of a major FCC solid solution matrix in which was precipitated a Ti-rich L1₂ ordered structure as well as a duplex $\eta + \sigma$ phase. Structural and chemical analysis of the two phases suggest that the η phase is a hexagonal close-packed (HCP) (Ni,Co,Fe)₃(Ti,Cr) phase, while the σ phase is expected to be a BCT (Fe,Co,Ni)(Ti,Cr) phase. The strengthening mechanisms at play are expected to be solid solution strengthening and secondary phase strengthening due to the precipitation of the hard duplex phase, which resulted in an increase in alloy hardness and compressive yield strength on Co content reduction. On the other hand, a decrease in the alloys' compressive strength and a significant degradation of fracture strain with decreasing Co content was observed. This was attributed to the large misalignments that exist between the structure of the FCC matrix and those of the precipitated intermetallic phases, which can lead to an accumulation of dislocations at the interfaces between them and consequently premature failure of the alloy. It was therefore concluded that decreasing the Co content of Co_xCrFeNiTi_{0.3} alloys is unfavorable due to the resulting increase in the amount of the $\eta + \sigma$ duplex phase formed as a result of this reduction.

In a later study by Shun et al. [76], with a similar motivation of reducing the cost of CoCrFeNiTi HEAs, the authors explored the substitution of Co with Ni (both of which are known FCC phase stabilizers) and its effect on the resulting alloys' properties. Co_{1-x}CrFeNi_{1+x}Ti_{0.3} (x=0, 0.5,1) were fabricated via arc melting followed by a homogenization heat treatment at 1200°C for 2 hours, hot rolling, and aging for 72 hours at temperatures between 500°C and 1200°C. While the alloys exhibited a simple FCC structure in the as-rolled condition, following aging, precipitation of secondary η and σ phases occurred in the FCC matrix. On increasing the value of x i.e. increasing the Ni content at the expense of Co, an increase in alloy hardness, yield strength, and ultimate tensile strength is observed. However, similar to the previous results reported in [75], a significant decrease in ductility accompanying the increased amounts of η and σ precipitates was also observed. The alloy hardening was attributed to three main factors, namely: secondary phase strengthening due to η and σ phase precipitation; solid solution strengthening; and the greater number of strong Ni-Ti, Ni-Cr, and Ni-Fe bonds that form as a result of the large negative mixing enthalpy between Ni and the remaining elements compared to their mixing enthalpy with Co, which leads to a stronger, less ductile alloy. The complete dissolution of σ at 1000°C and η at 1100°C leads to a severe softening of the alloys at these temperatures and up to 1200°C in addition to grain coarsening as a result of the elevated temperature.

The concurrence of the η and σ phases has also been reported by Shun et al. [13] in a study that focused on exploring the age treatment behavior of the CoCrFeNiTi_{0.3} alloy. Alloy samples were produced via arc melting and were subsequently subjected to aging heat treatments for durations spanning 24 to 144 hours at temperatures from 500°C to 1000°C. Age treatment at temperatures up to 700°C produced a dendritic structure consistent with that in Hung et al. [75] described above. Age hardening is observed at treatment temperatures between 600°C and 800 °C, with the optimum hardening occurring after treatment for 144 hours at 700°C due to large amounts of the η and σ phases that form. An interesting observation is the complete dissolution of the σ

phase at 1000°C, while the η phase remained in abundance within the FCC matrix. At this condition, the alloy age-softened, which was reflected in the significant decrease in its hardness. This led to the suggestion that the main hardening contribution comes from the σ phase. However, more information regarding the alloy's mechanical behavior is still needed to further understand the individual effects of its different phases, which was not clear in this study since hardness testing was the only measure used to probe its mechanical performance under different treatment conditions.

In addition to CoCrFeNiTi alloy strengthening through the concurrent precipitation of the η and σ phases, the η phase has also been found to have a synergistic strengthening effect when precipitated in alloys with oxide nanoparticle dispersions. To that end, Moravcik et al. [15] studied the structural evolution and mechanical properties of a $\text{Ni}_{1.5}\text{Co}_{1.5}\text{CrFeTi}_{0.5}$ ($\text{Co}_{1.5}\text{CrFeNi}_{1.5}\text{Ti}_{0.5}$ for consistency with current study) HEA produced by a combination of mechanical alloying (via high-energy ball milling) and spark plasma sintering (SPS). The alloy samples were annealed at 700°C, 900°C, and 1100°C for 48 hours followed by air-cooling, which led to the precipitation of an η phase within an FCC solid solution matrix. However, the origin of the oxide dispersions is different from that of the η phase, where they form as a result of surface contamination inherent to the ball milling process. The oxide phase was identified as Ti oxides, which formed due to the high affinity of Ti to oxygen. The best combination of mechanical properties was achieved after aging at 700°C with an ultimate tensile strength (UTS) of 1660 MPa and an elongation of 14%. It is proposed that the oxide dispersions play a major role in strengthening the alloys under all conditions, both directly through Orowan strengthening and indirectly, where the oxide particles impede grain growth through grain boundary pinning. At higher annealing temperatures (900°C and 1100°C), a loss of strength and hardness is observed due to: grain coarsening; the coarsening and change in morphology of the η structure; and the dissolution of the η and σ phase; all of which is consistent with previous reports [13], [75], [76].

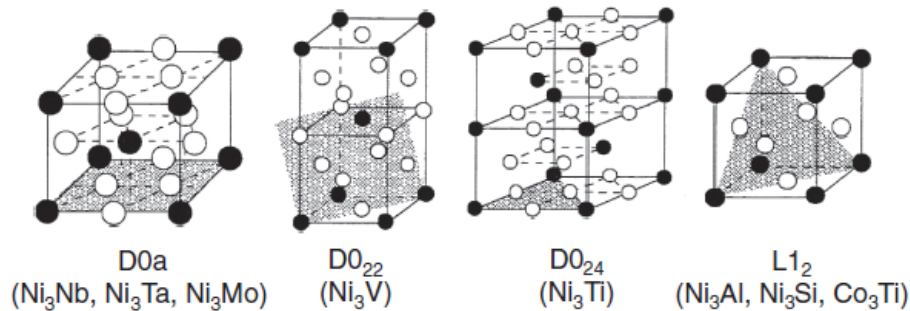


Fig. 3.3.2. The crystal structures of some geometrically close-packed (GCP) phases of the A₃B type. Each structure is labeled with its Strukturbericht designation and its prototype phase. The white circles correspond to the Ni atoms in the prototype phase, while the black circles correspond to the phase's other element [73].

(iii) Other Phase Combinations

The studies reviewed thus far mainly focus on CoCrFeNiTi alloys with relatively simple structures consisting of one primary solid solution phase and one type of secondary intermetallic phase (TCP or GCP). However, alloys of this system have also been found to exhibit more complex structures with numerous and multiple types of intermetallic phases.

In a study by Shun et al. [9], the effect of Ti addition on the microstructure and mechanical properties of the CoCrFeNi HEAs was explored. This was one of the earliest reports to systematically study the CoCrFeNiTi HEA system, and the authors were able to shed some light on the types of IM phases that form as a result of varying the Ti content of the alloy. CoCrFeNiTi_x (x=0, 0.3, and 0.5) were fabricated via arc melting and the samples were characterized in their as-cast states. The obtained microstructures were previously described in section 3.3.1 and accordingly, only the types of secondary phases that form within this alloy will be discussed more in-depth here. Both the CoCrFeNiTi_{0.3} and CoCrFeNiTi_{0.5} alloys form a dendritic structure, where the dendrite region consists of a single FCC solid solution structure that is slightly depleted of Ti (with almost equal amounts of the remaining elements). In the interdendrite of CoCrFeNiTi_{0.3}, plate-like intermetallic particles form, which were identified to be a (Ni, Ti)-rich R phase and a (Cr, Fe)-rich σ phase. The R phase is also a TCP phase that forms in HEAs [64]. The CoCrFeNiTi_{0.5} exhibits a structure similar to that of the CoCrFeNiTi_{0.3} alloy, but has a (Ti, Co)-rich Laves phase in addition to the R and σ phases in its ID, which formed due to the excess Ti content in the alloy. Based on a chemical and structural analysis, the Laves phase is expected to be (Co,Fe,Ni,Cr)₂Ti; the R phase (Ni,Co,Fe)₂(Ti,Cr); and the σ phase (Cr,Ti)(Fe,Co,Ni). The authors argue that the Cr atoms can more readily substitute for the Ti atoms on its sublattice due to their similar crystal structure at elevated temperatures as well as the proximity of their electronegativities. On the other hand, it is suggested that Ni, Co, and Fe can more readily substitute for one another due their close atomic sizes and electronegativities. Regarding their effect on the mechanical behavior of the alloys, the precipitated IM phases led to an increase in their yield and compressive strengths. However, a deterioration of their ductility was observed, which was attributed to the misalignments between the structure of the FCC matrix and those of the IM phases as previously described [75].

So far, all the reports reviewed entail studies of the microstructure and mechanical properties of small-small sized samples produced primarily by arc melting and in some cases powder metallurgy (PM). Jiang et al. [11] studied the effect of annealing on the microstructure of CoCrFeNiTi_{0.5} large cast samples produced by a medium frequency induction furnace. Samples were cut from the cast ingot and were subjected to annealing at 600°C, 700°C, 800°C, and 1000°C for 6 hours followed by furnace cooling. The samples exhibited a dendritic structure similar to that described previously. Annealing below 1000°C resulted in a (Ni, Ti)-rich phase R phase, a (Fe, Cr)-rich σ phase, and a (Co, Ti)-rich Laves phase in the ID. Results of the chemical analysis suggest that the R phase is Ni_{2.67}Ti_{1.33} with a (Ni,Co,Fe)₂(Ti,Cr) structure and the Laves phase Co₂Ti with either the (Co,Cr,Fe,Ni)₂Ti or (Co,Cr,Fe,Ni)₂(Ti,Cr) structure. On annealing above 1000°C, a dissolution of the Laves phase occurs, while the R and σ phase coarsen. The as-cast micro- and macro-hardness values are 618.8 HV and 52 HRC respectively, which remained unchanged up to annealing at 1000°C, at which the alloy softens due to changes in the morphologies of the IM phases. The results give an indication of the alloys' structural stability up to this temperature.

3.3.3. Computational Phase Diagrams of the CoCrFeNiTi System

Despite the increase in interest in the CoCrFeNiTi system, most efforts to explore its alloys have been limited to experimental studies. To the best of our knowledge, the current literature on CoCrFeNiTi HEAs does not include any extensive computational phase diagrams, but rather partial diagrams limited either by the composition or temperature ranges they cover. Despite these limitations, the available diagrams offer some valuable insight into the type of structures and phases that should be expected for different compositions of CoCrFeNiTi HEAs. Moreover, they help with identifying some trends in alloy structures as a function of composition and temperature.

Chang et al. [77] used the Thermo-Calc software [53] and the TCNI5 [78], a database originally developed for use with Ni-superalloys, to produce a partial phase diagram of the Al_xCo_{1.5}CrFeNi_{1.5}Ti_y (x+y=0.5) system shown in Fig. 3.3.4. At x = 0, the alloy is the CoCrFeNiTi_{0.5} and the diagram shows that the γ (disordered FCC solid solution phase) and η phases are the equilibrium phases above 700°C and just under 1000°C. In the study, the Al content is increased at the expense of Ti in an attempt to stabilize the γ' strengthening phase rather than the less favorable η phase. This trend is clear from the diagram in Fig. 3.3.4 and is supported by the study's experimental results.

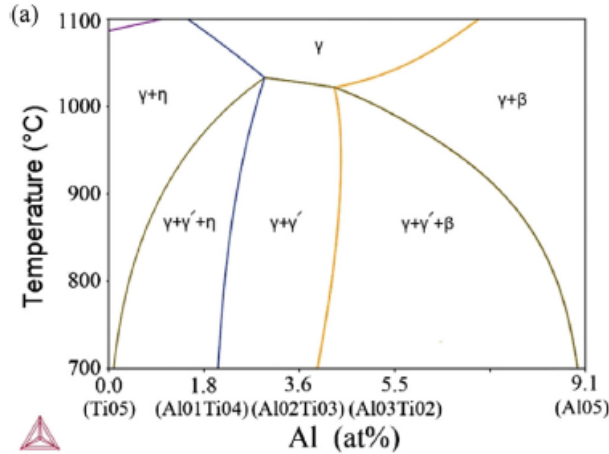


Fig. 3.3.3. Partial phase diagram of the $Al_xCo_{1.5}CrFeNi_{1.5}Ti_y$ ($x + y = 0.5$) system produced by Thermo-Calc and the TCN15 database [77].

He et al. [79] also used the CALPHAD method to calculate the amounts of phases present in a $CoCrFeNiTi_{0.4}$ HEA as temperature is varied using the JMatPro software [80] and the TTNi8 [78] database. The resulting diagram is shown in Fig. 3.3.3 and in the study, the authors investigated the possibility of using kinetic methods, mainly through varying the cooling rate of laser-melted alloys, to control which phases are formed. From the diagram it can be seen that within the temperature range shown ($600^{\circ}C - 1600^{\circ}C$), a primary FCC solid solution is stable in addition to various intermetallic phases such as the σ and γ' phases. The experimental results in the study showed good agreement with the CALPHAD results. However, it was noted by the authors that the accuracy of the calculations needed further improvement due to some mismatch between the predicted phases and the experimental data.

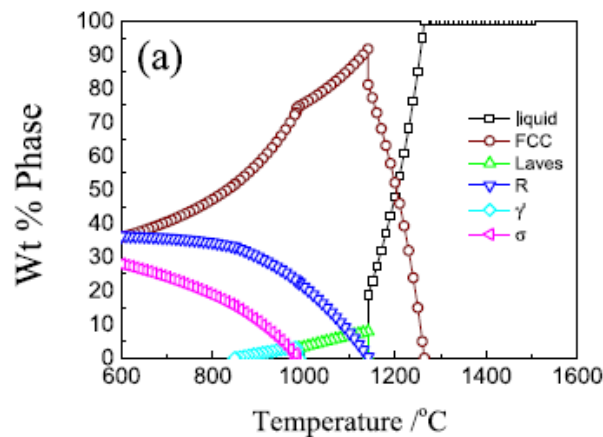


Fig. 3.3.4. Phase amounts calculated using CALPHAD for a $CoCrFeNiTi_{0.4}$ HEA using the JMatPro software and the TTNi8 database [79].

Perhaps the most extensive phase diagram available (to the best of our knowledge) for the $CoCrFeNiTi$ system is that shown in Fig. 3.3.5. This diagram was published in a review by Liu et al. [7], in which the authors discussed the precipitation hardening behavior of $CoCrFeNi$ HEAs

when various fifth elements are added including Ti. In the review, the CoCrFeNiTi_x phase diagram produced by the Thermo-Calc [53] software and the TCHEA1 [33], [57] database was presented as unpublished data by Tong et al. The diagram covers a composition range of $x = 0$ to $x = 0.15$ of the CoCrFeNiTi_x alloy system and spans a temperature range of 750°C to 1500°C. One interesting perspective is that in this diagram, the CoCrFeNi alloy (ie. at $x = 0$) can be considered as a pseudo-element and the phase diagram as a whole can be considered a pseudo-binary phase diagram. It should also be noted that the phases predicted in the CoCrFeNiTi_x diagram in Fig. 3.3.5 are in good agreement with those observed in experimental studies of the alloys it includes, however, it still needs further validation.

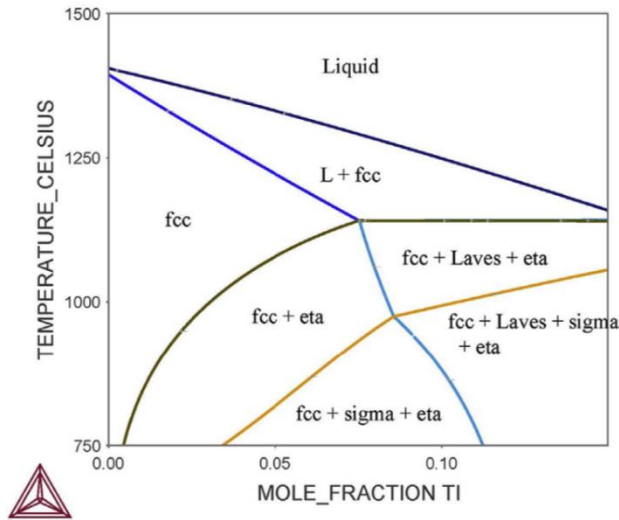


Fig. 3.3.5. Partial computational phase diagram of the CoCrFeNiTi_x HEA system, where x is the mole fraction of Ti. The diagram covers the region of the system from 0 (ie. equiatomic CoCrFeNi) to 0.15 mole fraction Ti and 750°C – 1500 °C [65].

3.4. HEA Properties from First Principles

Determining and understanding the phase stabilities of a given system is only the first step for successful alloy design. Once a potential alloy composition is determined, this should be followed by a characterization of its properties. In the following, a description of the tools that facilitate the modelling and computational characterization of HEAs is provided.

3.4.1. Special Quasirandom Structures (SQSs)

SQSs are important tools for the modeling of random alloys such as HEAs solid solution phases. An SQS is a periodic structure that is representative of the random alloy and is constructed based on mimicking the correlation functions of the first few nearest neighbors for given lattice sites. This approach has several advantages, the most important being the offset of periodicity errors to more distant neighbors, which allows for small representative cells that are accessible to electronic structure calculations such as density functional theory (DFT) [81]. Periodicity arises

because in most electronic structure calculations, periodic boundary conditions (PBC) are applied such that a given representative system of interest is surrounded by an infinite number of identical systems during a simulation. This has the benefit of preventing the creation of artificial interfaces between the simulated system and its environment (ex. vacuum) [82]. However, this works best if the system of interest is periodic and while solid solution HEAs usually have a distinct crystal structure, the arrangement of the atoms in their lattice is random. Accordingly, small, computationally inexpensive cells with a random distribution of atoms often cannot capture the randomness of bulk solid solution HEAs under PBC. However, as mentioned, this can be overcome by applying the SQS concept to model solid solution HEAs.

There are two common methods of generating SQSs, which are exhaustive enumeration or by applying stochastic methods to the search for the SQS [83]. Both approaches are implemented in the Alloy Theoretic Automated Toolkit (ATAT) [84] in the *gensqs* and the *mcsqs* codes respectively. However, the use of *gensqs* is not recommended and is generally only suitable for generating small SQS cells. On the other hand, the *mcsqs* code uses a Monte Carlo (algorithm) to speed up the search for an SQS and has been shown to be highly effective and efficient for generating cells consisting of up to hundreds of atoms [85]. Once a suitable SQS is found, DFT can then be applied to the generated structure to calculate the desired alloy properties.

3.4.2. Current State of HEA SQS First Principles Studies

Several studies have emerged that exploit the strength of SQSs in representing random alloys for the study of various types of HEAs using DFT. Some of the properties calculated are the electronic, and mechanical properties of HEA SQSs. In the following sections, a brief review of HEA property calculations using DFT and the SQS approach is provided with a special focus on mechanical properties.

3.4.2.1. Formation Energies and Phase Stabilities

The SQS approach can be used for the calculation of HEA enthalpies of formation at zero K, which can offer important information for establishing phase stability rules such as those discussed earlier. For instance, the enthalpies of formation can help distinguish the ground state phase of an alloy by comparing the formation energies calculated for different crystal structures or magnetic states. Where experimental structural data is available, it is also possible to test the accuracy of the generated SQSs by evaluating whether the ground state can be predicted by comparing their formation energies [83].

3.4.2.2. Vibrational and Electronic Entropies

As discussed earlier, it has been shown that the different entropic contributions, and especially the vibrational entropy, can play a significant role in the stabilization or destabilization of a given phase in an alloy [40]. It is therefore important to quantify the different entropy contributions to further understand the phase stabilities in HEAs. DFT can be used to calculate the phonon density of states (DOS) of an SQS, from which the vibrational free energy and the

vibrational entropy can be calculated. Similarly, DFT can also be used to calculate the electronic entropy of an SQS [83]. For example, Wang et al. [86] used SQSs for disordered phases and DFT to predict phase separations in V-Nb-Mo-Ta-W refractory HEAs by considering changes to different entropy contributions. Moreover, Fig. 3.4.1 illustrates the calculation of various entropy contributions (electronic and vibrational) as well as the Helmholtz free energy of mixing for 64-atom FCC, BCC, and HCP HEA SQSs [83]. These examples highlight how powerful the SQS method is for modelling HEAs and studying their properties from first principles, which would otherwise be very difficult.

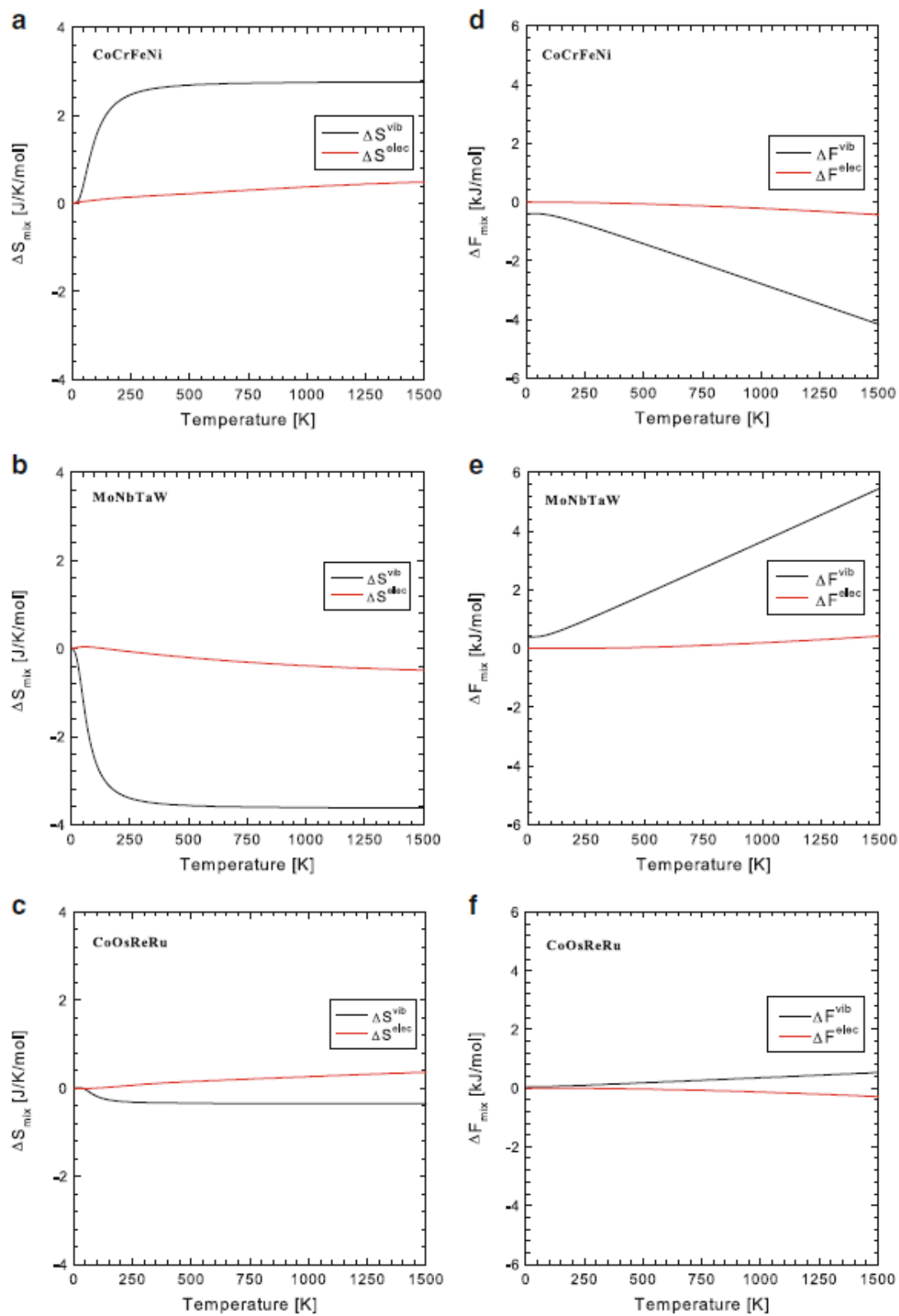


Fig. 3.4.1. Vibrational and electronic entropies and Helmholtz vibrational and electronic free energies of mixing for 64-atom FCC CoCrFeNi; BCC MoNbTaW; and HCP CoOsReRu alloy SQSs [83].

3.4.2.3. Elasticity Theory and Mechanical Properties

The SQS approach has been especially important in providing a suitable model for random alloys which enables the computational characterization of the mechanical properties of HEAs [87]–[89]. This is usually achieved by calculating the second order elastic constants (SOECs) of the HEA SQS of interest, where for a cubic system (eg. FCC or BCC HEAs), there are three independent elastic constants, namely c_{11} , c_{12} , and c_{44} .

One of the most common methods used in literature to determine the elastic constants of HEA SQSs with cubic structures is to first calculate bulk modulus, B , of the alloy by fitting the Birch-Murnaghan equation of state (EOS) to energy-volume data calculated using DFT. The tetragonal shear modulus, C' can then be obtained through a volume-conserving orthorhombic deformation of the structure. The elastic constants c_{11} and c_{12} can then be calculated from B and C' , while c_{44} is determined from a volume-conserving monoclinic deformation to the structure. Details of the procedure as applied to a cubic SQS with an FCC structure can be found in [87].

An alternative approach is implemented in the ElaStic [90] package, which is a powerful tool that automates the calculation of the elastic constants and additionally includes utilities for the calculation of the mechanical properties of a given structure. The general essence of the methods used is the same as above, where selected deformations are applied to the original structure and from the DFT output either the resulting energy or stress data is used for the property determination. For a given structure geometry, the stress approach will require less data points compared to those needed for the energy approach and is preferred if the DFT package used for the deformed structures calculations includes the stress tensor calculation. The procedure used is summarized in Fig. 3.4.2 and a detailed account of the methodology used can be found in [90].

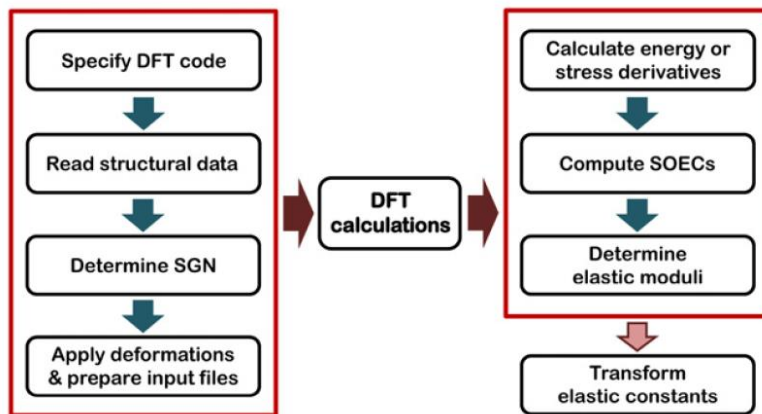


Fig. 3.4.2. The procedure used for calculating the elastic constants and moduli of a give structure using the ElaStic package [90].

Once the elastic constants have been determined, it is possible to calculate the bulk, shear, and Young’s modulus in addition to the Poisson’s ratio of the structure of interest. The bulk and shear moduli can be calculated either using the Voigt, Reus, or Hill methods. Values for properties

calculated using the Voigt approach represent an upper bound while the those calculated using the Reus procedure are a lower bound. This was shown by Hill [91] and accordingly, the arithmetic average of both quantities is the Hill average and is reported for all properties in the current study.

3.5. Research Aims and Objectives

The above discussion highlights the importance of HEAs as emerging materials that can fill the gaps left by conventional alloys. However, several obstacles still hinder their full exploration, the most important of which being the massive compositional search space associated with each HEA system. Additionally, the need for exploring non-equiatomic compositions exacerbates this problem. The CoCrFeNiTi HEA system has gained interest from researchers in recent years due to its potential to form alloys that are both strong and ductile. However, its exploration remains limited by the trial and error approaches of experimental studies. Limited computational efforts have been made to study the phase stabilities encompassed by comprehensive composition and temperature ranges. Accordingly, this work aims at systematically investigating non-equiatomic compositions of the CoCrFeNiTi alloys to identify those that results in favorable structures, specifically alloys with single-phase FCC solid solution structures.

The work undertaken targets achieving the following objectives:

- (i) Produce comprehensive computational phase diagrams for the $\text{CoCrFeNi}_x\text{Ti}_{2-x}$, $\text{Co}_x\text{CrFeNiTi}_{2-x}$, $\text{CoCrFe}_x\text{NiTi}_{2-x}$, and $\text{CoCr}_x\text{FeNiTi}_{2-x}$ subsystems of the broader CoCrFeNiTi HEA system using the CALPHAD approach
- (ii) Contribute to the understanding of the thermodynamic stabilization of single-phase HEAs as opposed to multi-phase ones again using CALPHAD approach.
- (iii) Study the mechanical properties of a single-phase FCC HEA from the CoCrFeNiTi system using first principles density functional theory method. The particular composition to be examined is determined from step (i) and (ii) above.

Thus, the work undertaken in this thesis establishes a systematic framework to pinpoint single phase solid solution HEA and then computationally characterize its mechanical properties. The framework combines two different scales of computational methods: a continuum level thermodynamic CALPHAD approach and a discrete atomistic level based on density functional theory. We believe that the framework presented in this thesis can be used to analyze and study other HEA systems.

Chapter 4. Computational Methods

4.1. CALPHAD

The CALPHAD method was used to carry out thermodynamic equilibrium calculations for subsystems of the CoCrFeNiTi HEAs, namely the $\text{Co}_x\text{CrFeNiTi}_{2-x}$, $\text{CoCr}_x\text{FeNiTi}_{2-x}$, $\text{CoCrFe}_x\text{NiTi}_{2-x}$, and $\text{CoCrFeNi}_x\text{Ti}_{2-x}$ systems, where x ranges from 0 to 2. In these systems, the concentration, x , of each constituent element is increased at the expense of Ti. This allowed the investigation of the effect of each element on the thermodynamics and phase stabilities of the CoCrFeNiTi HEAs. Thus, the region of compositional space explored here is wide and beyond the traditional exploration of equiatomic systems. The results of the equilibrium calculations were used for the construction of phase diagrams of each subsystem in addition to the extraction of information pertaining to the thermodynamic properties of the systems under different conditions of composition and temperature.

In the following, descriptions of the phase diagram construction from the CALPHAD output as well as the computational codes developed for this purpose are presented. Moreover, details of the calculation of the various thermodynamic properties are given.

4.1.1. Single-Point Calculations in OpenCalphad

An overview of the CALPHAD method including details of the various phase models needed for calculating the equilibrium state of alloys was given in section 3.2. Using a CALPHAD software and a suitable thermodynamic database the equilibrium phases at a given alloy composition and temperature can be calculated. In the present study, the OpenCalphad software [55] was used with the mc_ni.tdb database [60] to carry out the CALPHAD calculations. Both the software and the database are open-source, the benefits of which have already been discussed. Attempts to benchmark the database used were made, an example of which is provided in Appendix A.

4.1.1.1. Input

To calculate the thermodynamic equilibrium state of a system using OpenCalphad, a database, the system constituents, and a set of conditions must be defined and input to the software. The OpenCalphad software does not come with a graphical user interface (GUI) and therefore the input to can be entered either through its command line user interface or using input files. In the current study, we opted for the latter and a typical input file is provided in Appendix A.

Once a database is selected, the specific elements comprising the desired alloy need to be determined since a single database can contain thermodynamic data for many elements. The concentration of each elements as a fraction of the system size should then be determined. In the current study, a system size of 1 mole was chosen for simplicity and the element amounts are therefore defined in mole fractions. Finally, the system temperature and pressure (typically atmospheric pressure) at which the equilibrium is to be calculated are required. As an example, the

input to compute the equilibrium state of the CoCrFeNi_{1.75}Ti_{0.25} alloy studied experimentally at 1500 K is shown in Table 4.1.1.

Table 4.1.1. OpenCalphad input example for CoCrFeNi_{1.75}Ti_{0.25} at 1500 K

Description	Symbol	Value
Database	N/A	mc_ni.tdb
Elements	N/A	Co, Cr, Fe, Ni, and Ti
Element concentration in mole fraction	x(co); x(cr); x(fe); x(ni); x(ti)	0.2; 0.2; 0.2; 0.35; 0.05 respectively
Temperature in Kelvin	T	1500
Pressure in Pa	P	1e5 (atmospheric pressure)
System size in moles	n	1

4.1.1.2. Output

1. General system information such as the temperature (T) and pressure (P). The last line shows the system Gibbs energy (GS), enthalpy (HS), and entropy (S)

2. System component information including their amounts, chemical potentials, and activities

3. Phase equilibrium information including the names of stable phases, their amounts, and composition.

```

Output for equilibrium: 1, DEFAULT_EQUILIBRIUM 2020.05.05
Conditions .....:
1:T=1500, 2:P=100000, 3:X(CO)=0.2, 4:X(CR)=0.2, 5:X(Fe)=0.2, 6:X(NI)=0.35,
7:N=1
Degrees of freedom are 0

Some global data, reference state SER .....:
T= 1500.00 K ( 1226.85 C), P= 1.0000E+05 Pa, V= 0.0000E+00 m3
N= 1.0000E+00 moles, B= 5.6291E+01 g, RT= 1.2472E+04 J/mol
GS= -1.00721E+05 J, GS/N= -1.0072E+05 J/mol, HS= 3.9188E+04 J, S= 932.727 J/K

Some data for components .....:
Component name Moles Mole-fr Chem.pot/RT Activities Ref.state
CO 2.0000E-01 0.20000 -8.4393E+00 2.1619E-04 SER (default)
CR 2.0000E-01 0.20000 -6.4880E+00 1.5216E-03 SER (default)
FE 2.0000E-01 0.20000 -8.1347E+00 2.9318E-04 SER (default)
NI 3.5000E-01 0.35000 -8.0155E+00 3.3031E-04 SER (default)
TI 5.0000E-02 0.05000 -1.3162E+01 1.9215E-06 SER (default)

Some data for phases .....:
Name Status Moles Volume Form.Units Cmp/FU dGm/RT Comp:
FCC_A1..... E 1.000E+00 0.00E+00 1.00E+00 1.00 0.00E+00 X:
NI 3.5000E-01 FE 2.0000E-01 CR 2.0000E-01 TI 5.0000E-02
CO 2.0000E-01

```

Fig. 4.1.1. Output obtained from an OpenCalphad single-point equilibrium calculation for a CoCrFeNi_{1.75}Ti_{0.25} alloy at 1500 K. The red boxes highlight the different types of data available pertaining to the equilibrium state of the system. These are: general system information; system component information; and phase equilibrium information.

Fig. 4.1.1 shows the output of the equilibrium calculation using OpenCalphad for the conditions defined in Table 4.1.1. In the figure, three regions of the output are highlighted in red boxes, where data is located pertaining to: (1) general system information; (2) system component information; (3) phase equilibrium information. Each of these are addressed separately below, however, it should be noted that all quantities given in the output are in mole fractions, which was chosen again for simplicity as the calculations were carried out for a system size of 1 mole. The results shown in Fig. 4.1.1 are only part of the larger output file, which is provided in full in Appendix A.

General System Information

In this section of the results, the global data of the system is stated. This includes the temperature (T), pressure (P) as well as other information such as the number of moles (N) and the value of RT, which is the ideal gas constant multiplied by the system temperature. In the last line of this portion of the results, the system's thermodynamic properties are listed, namely its Gibbs energy (GS), molar Gibbs energy (GS/N), enthalpy (HS), and entropy (S). These will be further discussed in relation to their use in the thermodynamic property calculation presented in section 0.

System Component Information

The system components chosen are then listed, which in the present example of the CoCrFeNi_{1.75}Ti_{0.25} are the elements Co, Cr, Fe, Ni, and Ti. The concentration of each element is stated in addition to its chemical potential (μ_i) per R.T, where μ_i is related to the Gibbs energy of the system (GS) by the following equation

$$GS = \sum_i x_i \cdot \mu_i \quad \text{Equation 4.1.1}$$

Phase Equilibrium Information

The phases present in the system at equilibrium are then listed. The amount of each phase in mole fraction is shown in addition to the phase composition, where its constituent elements and their amounts are given.

4.1.1.3. General remarks on the choice of database

It is worth reiterating that the mc_ni.tdb database [60] was not originally developed for HEA calculations but rather for multi-component Ni-base superalloys. However, it was chosen for use in this study since it includes all the binary and ternary interaction parameters for the elements present in the CoCrFeNiTi alloys. It was also, to the best of our knowledge and at the time of this publication, the only well tested open-source database with thermodynamic descriptions suitable for use in multi-principal element and multi-component systems. The database has been tested within the following composition ranges of the elements present in our system of interest: Co, Cr, and Fe < 20 wt.%; Ti < 4 wt.%; and Ni as a primary solvent element. These limits are in good agreement with the alloy compositions studied in the present study. Since the database file is too large to include as a whole, only a portion of the database version 2.033 used in this study is provided in Appendix A. The part included shows some useful information about the database and only excludes the part where the model parameters are extensively listed. Finally, the database was originally developed for use with the MatCalc software [92]. Accordingly, some syntax changes needed to be made to the database for it to be readable by OpenCalphad.

4.1.2. Phase Diagram Construction

The OpenCalphad software includes STEP and MAP functions, which allow the user to automatically plot various properties as well as phase diagrams. While these utilities work well for lower-order alloys such as binary and ternary systems, they have been found to be problematic for

Step 1: Determining possible phase combinations in the studied systems

The composition-temperature space of each system of interest was manually scanned by running several single-point calculations at regular composition and temperature intervals. The output of these calculations was used to compile a preliminary list of possible phases for the investigated system. Each discovered phase combination was assigned a color code to be distinguishable from the remaining phase combinations when plotting the phase diagram. This was done for all the systems studied and a comprehensive list was developed containing all the phase combinations found in the subsystems of the CoCrFeNiTi HEA system. This comprehensive color-coded list was continuously updated throughout the phase diagram construction process as more phases became known. The single-point calculations were carried out at composition intervals of 0.01 (mole fraction) and temperature intervals of 100 K, which provided a sufficient base for the remaining steps to be carried out successfully.

Step 2: Automating a dense mesh of single-point equilibrium calculations

Single-point calculations were run to cover a dense mesh within the composition-temperature space of the alloy systems. The composition of each element was varied from 0 ($x=0$) mole fraction to 0.4 ($x=2$) in increments of 0.001 at the expense of Ti. For example, in the $\text{CoCrFeNi}_x\text{Ti}_{2-x}$ system, the composition at $x=0$ is CoCrFeTi_2 and $x=2$ CoCrFeNi_2 . At each composition, calculations were run from 300 K to 2000 K in increments of 1 K. The equilibrium phases at each combination of composition and temperature were extracted from the calculation output and were appended to a single output file for further processing. Due to the immense number of calculations required for the phase diagram construction, this task was automated using a Bash Shell script. A sample of the compiled output for this system is also shown in Fig. 4.1.3.

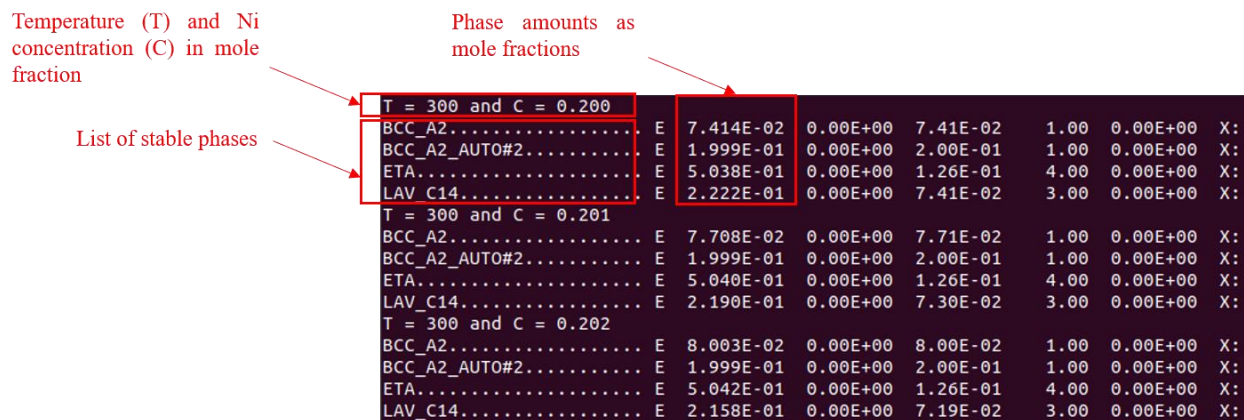


Fig. 4.1.3. Sample of the compiled output from the $\text{CoCrFeNi}_x\text{Ti}_{2-x}$ automated calculations.

Step 3: Processing the compiled output using a developed C++ code

A C++ code was developed to process the output from the calculations carried out in the previous step. The code reads the compiled output file to identify the equilibrium phases present at a given combination of temperature and composition. A number is then assigned to the

temperature and composition point, which corresponds to a phase combination and color from the phase list. The code can also read the amount of each present and the user can define a cut-off for which phases to consider in the determination of the equilibrium phase combination. In the present study, the cut-off was set for any phase amount $< 10^{-3}$. For each system, a text file is generated, which contains all the combinations of temperatures and compositions and their assigned numbers.

Step 4: Scatter plot generation using a developed Python code and the Matplotlib library

To generate the phase diagram of a system, its corresponding text file generated by the C++ code was read by a Python code, that was developed to generate a scatter plot with alloy composition on the x-axis and temperature on the y-axis. The assigned number is translated into a color for the datapoint to be plotted in the scatter plot. Due to the dense mesh that was used, distinct phase regions are distinguishable by their color, which corresponds to the color code assigned in the phase list as seen in Fig. 4.1.2 (b). For presentation purposes, the resulting scatter plots, once finalized, were traced and labeled using the Inkscape image processing software (Fig. 4.1.2 (c))

Step 5: Addition of any missing phase combinations to the phase list

Since the compilation of the phase list initially depended on a manual scan of the composition-temperature space, it was possible that some phase combinations were not identified. The C++ and Python codes were developed such that if an unknown phase combination is encountered, it would be assigned a special color. This allowed the identification of any phase combinations initially missed. The phase list as well as the C++ and Python codes were updated and steps 3-5 were repeated until no unknown phase combinations were present.

4.1.3. Thermodynamic Calculations

4.1.3.1. Mixing Enthalpy and Entropy

$$H_{alloy} = \sum_i^n x_i H_i + \Delta H_{mix} \quad \text{Equation 4.1.2}$$

$$S_{alloy} = \sum_i^n x_i S_i + \Delta S_{mix} \quad \text{Equation 4.1.3}$$

Equation 4.1.2 and Equation 4.1.3 were used to calculate the mixing enthalpy ΔH_{mix} and the mixing entropy ΔS_{mix} of the alloys in the systems studied, respectively. H_{alloy} and S_{alloy} are the system enthalpy and entropy, respectively, and were obtained from the CALPHAD single-point calculations carried out. H_i and S_i are the elemental enthalpies and entropies, which were obtained from the NIST-JANAF Thermochemical tables [94] for each element at the temperatures of interest. The calculated ΔH_{mix} and ΔS_{mix} were plotted as a function of alloy composition in each of the systems studied at temperatures ranging from 1100 K to 1700 K. The changes in ΔH_{mix} and ΔS_{mix} were compared to those in their corresponding phase diagrams to find any connections between the alloy phase stabilities to their thermodynamic behavior. In addition to ΔH_{mix} and ΔS_{mix} , the ratio $\Delta H_{mix}/T \cdot \Delta S_{mix}$ was also calculated and plotted as a function of compositions at the same temperatures for the investigation of the effect of the relative magnitudes of these quantities on the phase stability, if any.

4.1.3.2. The Deviation of the Thermodynamic Properties from the Ideal Solid Solution Behavior

Recalling from Section 2.2

$$\Delta H_{mix}^{ideal} = 0$$

$$\Delta S_{mix}^{ideal} = \Delta S_{mix,conf} = -R \sum_i^n x_i \ln x_i$$

$$H_{mix}^{excess} = \Delta H_{mix} - \Delta H_{mix}^{ideal} = \Delta H_{mix}$$

$$S_{mix}^{excess} = \Delta S_{mix} - \Delta S_{mix}^{ideal}$$

The above equations were used to calculate the deviation of the calculated ΔH_{mix} and ΔS_{mix} from the ideal solid solution behavior, namely the quantities H_{mix}^{excess} and S_{mix}^{excess} , respectively. The enthalpy and entropy deviations were also plotted as a function of composition in the 1100 K to 1700 K temperature range. The extent of the systems' deviation from the ideal thermodynamic behavior was also analyzed to determine its effect on their phase stabilities through a comparison of the developed plots to the generated phase diagrams.

4.2. Density Functional Theory (DFT)

Based on the constructed phase diagrams, an alloy with a composition of $\text{CoCrFeNi}_{1.75}\text{Ti}_{0.25}$ was selected for further analysis. Density functional theory (DFT) was used for alloy property calculations including the characterization of its mechanical properties. All DFT calculations were carried out using the PWscf package included in the QUANTUM ESPRESSO (QE) open-source distribution [95], which consists of various packages for electronic-structure calculations within the framework of DFT and based on plane waves and pseudopotentials. All the calculations and analyses carried out for the alloy were also applied to its individual constituent elements for comparison with available experimental data in order to benchmark our methods. It is important to note that our goal was not to reproduce exact experimental values but rather to establish a basis for a meaningful comparison between the calculated properties of the $\text{CoCrFeNi}_{1.75}\text{Ti}_{0.25}$ and those of its constituent elements.

4.2.1. DFT Setup

4.2.1.1. Special Quasirandom Structure (SQS) Generation

To model the $\text{CoCrFeNi}_{1.75}\text{Ti}_{0.25}$ HEA, a special quasirandom structure was generated using the *mcsqs* code [85] in the Alloy Theoretic Automated Toolkit (ATAT) [84]. As explained previously, the SQS method allows a relatively accurate representation of the structure of random alloys using cells that are small enough to remain accessible to electronic structure calculations such as DFT. The SQS in the present study consisted of 80 atoms and the cell shape was constrained such that a $5 \times 2 \times 2$ FCC supercell was produced. In the generation of the SQS, pair correlation functions up to the second nearest neighbor distance were considered. Triplet correlations were also tested,

however, the structure in which only pairs was found to be less energetic (using DFT). Accordingly, all subsequent calculations and analysis approaches were applied for the pair correlation SQS only. The absolute magnitudes of the difference between the SQS correlation functions and the targeted functions corresponding to the truly random alloy did not exceed 0.03. The lattice vectors, lattice parameters, atomic positions, and site occupations of the final $\text{CoCrFeNi}_{1.75}\text{Ti}_{0.25}$ SQS are provided in Appendix D. For the DFT calculations, the generated structure is scaled to the calculated theoretical lattice parameter of 3.6 Å, which is based on a theoretical density of 8 g/cm³ calculated for the alloy using the rule of mixtures (ROM). Accordingly, the 5x2x2 supercell corresponds to 18x7.2x7.2 Å and a visualization of this structure using VESTA [96] is provided in Fig. 4.2.1. This value for the lattice parameter serves as an initial guess for structural relaxation as explained in the coming sections.

4.2.1.2. Pseudopotentials

All calculations use the generalized-gradient-approximation (GGA) with the Perdew-Burke-Ernzerhof (PBE) functional [97] for the treatment of exchange-correlation functionals. Ultrasoft pseudopotentials [98] for Co, Cr, Ni, and Ti were obtained from the Standard solid-State Pseudopotentials (SSSP) Precision library [99]. The pseudopotential for Fe (also ultrasoft) was obtained from pslibrary.0.3.0 [100]. The pseudopotentials used are listed in Table 4.2.1 in addition to their corresponding recommended energy and charge density cutoffs (E_{cut} and ρ_{cut} respectively). All calculations are carried out using an E_{cut} value of 90 Ry and ρ_{cut} of 1080 Ry.

4.2.1.3. K-point Convergence

K-point convergence tests were carried out for each element by calculating the force acting on a displaced atom as a function of the number of k-points (Appendix D). The optimal k-points were determined by applying a convergence criterion of 10 meV/Å and are shown in Table 4.2.2. For the $\text{CoCrFeNi}_{1.75}\text{Ti}_{0.25}$ SQS, the number of k-points were determined by applying the necessary scaling to the converged points for Ni as it is the majority constituent of the alloy. A 2x5x5 mesh was found to be very computationally expensive and a 1x3x3 was opted for instead to reduce the computational load. A Marzari-Vanderbilt smearing of 0.01 Ry was applied in all cases to accelerate the convergence of the electronic structure with respect to k-points.

4.2.1.4. Structural Relaxation

Using the above-mentioned pseudopotentials and the determined optimal k-points a full structural relaxation was carried out to obtain the minimum energy, unstressed structures for each of Co, Cr, Fe, Ni, and Ti as well as the $\text{CoCrFeNi}_{1.75}\text{Ti}_{0.25}$ SQS. For the relaxation of the $\text{CoCrFeNi}_{1.75}\text{Ti}_{0.25}$ SQS, the cell shape was constrained such that the cell axes remain at 90° to one another. The relaxed structures were used for all subsequent property calculations and the relaxed lattice parameters of the individual elements were compared to experimental values. The stopping criteria

for structure relaxation based on energy, force, and stress are 7.7D-6 Ry , 4.0D-5 Ry/a.u. , and 0.5 kbar , respectively.

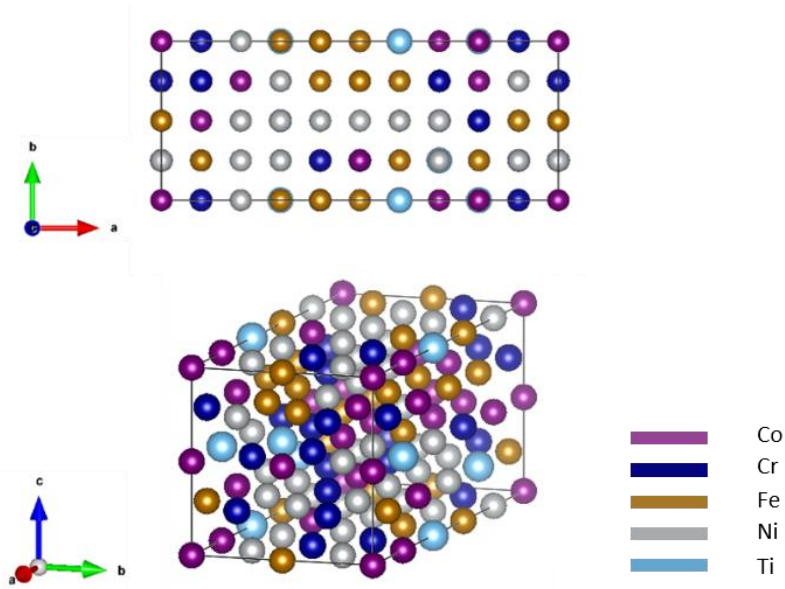


Fig. 4.2.1. Visualization of the generated $\text{CoCrFeNi}_{1.75}\text{Ti}_{0.25}$ SQS

Table 4.2.1. Element pseudopotentials for DFT calculations and the recommended energy and charge density cutoffs.

Element	Pseudopotential	E_{cut} (Ry)	ρ_{cut} (Ry)	Ref.
Co	Co_pbe_v1.2.uspp.F.UPF	90	1080	[99]
Cr	cr_pbe_v1.5.uspp.F.UPF	40	320	
Ni	ni_pbe_v1.4.uspp.F.UPF	50	400	
Ti	ti_pbe_v1.4.uspp.F.UPF	40	320	[100]
Fe	Fe.pbe-spn-rrkjus_psl.0.2.1.UPF	90	1080	

Table 4.2.2. Summary of structure, magnetism, and calculated optimal k-points used to treat each of Co, Cr, Fe, Ni, and Ti.

Element	Structure	Initial Assumption for Magnetism	Optimal k-mesh
Co	HCP	Ferromagnetic	8x8x4
Cr	BCC	Antiferromagnetic	12x12x12
Fe	BCC	Ferromagnetic	16x16x16
Ni	FCC	Ferromagnetic	10x10x10
Ti	HCP	Non-magnetic	12x12x6
$\text{CoCrFeNi}_{1.75}\text{Ti}_{0.25}$ SQS	FCC	Ferromagnetic	1x3x3

4.2.2. Alloy Formation Enthalpy, Lattice Distortion, and Magnetism

4.2.2.1. Zero Kelvin Formation Enthalpy (Enthalpy of mixing)

Following the structural relaxation of the 80-atom SQS and the individual elements, the total energies of the relaxed structures were used to calculate the zero Kelvin formation enthalpy, $H_{f,0K}$, of the alloy using Equation 4.2.1. Note that this is essentially the enthalpy of mixing of the alloy evaluated at zero Kelvin. $E_{SQS,relax}$ is the total energy of the relaxed SQS and $E_{i,relax}$ is that of the relaxed element i , where the summation runs over the alloy's constituent elements ie. Co, Cr, Fe, Ni, and Ti. The total energy of each element i is divided by the number of atoms in its unit cell, $n_{i,cell}$, to get the energy per atom, which is then multiplied by the number atoms of that element present in 80-atom SQS, $n_{i,SQS}$.

$$H_{f,0K} = E_{SQS,relax} - \sum_i \frac{E_{i,relax}}{n_{i,cell}} \times n_{i,SQS} \quad \text{Equation 4.2.1}$$

4.2.2.2. Lattice Distortion Quantification

To quantify the lattice distortion in the alloy SQS, the final positions $\vec{r}_{i,final}$ of the atoms in the relaxed SQS structure were compared to their initial positions $\vec{r}_{i,initial}$ prior to the relaxation. An average displacement $D_{i,avg}$ is defined for the atoms of each element i (Equation 4.2.2) in addition to an overall average displacement across all atom types D_{avg} (Equation 4.2.3), which is just a weighted average over all elements.

$$D_{i,avg} = \langle |\vec{r}_{i,final} - \vec{r}_{i,initial}| \rangle \quad \text{Equation 4.2.2}$$

$$D_{avg} = \sum_i x_i D_{i,avg} \quad \text{Equation 4.2.3}$$

4.2.2.3. Magnetism Analysis

The average magnetic moment of the atoms of each element type $\mu_{i,avg}$ in the SQS was calculated. These average values were compared to the magnetic moment of the atoms μ_i in the corresponding element's relaxed structure. To calculate $\mu_{i,avg}$, the following equation was used

$$\mu_{i,avg} = \langle |\mu_{i,SQS}| \rangle \quad \text{Equation 4.2.4}$$

where $\mu_{i,SQS}$ is the magnetic moment on atom of element i in the SQS.

4.2.3. Mechanical Properties

The mechanical properties of the 80-atom CoCrFeNi_{1.75}Ti_{0.25} SQS were calculated using two approaches. The first approach involves calculating the alloy's Young's modulus, Poisson's ratio, and ideal strength from its theoretical stress-strain behavior. In the second approach the calculation of its second order elastic constants (SOEC) allows the calculation of its bulk, shear, and Young's modulus as well as its Poisson's ratio. The properties calculated using each method were compared. The same methods were also used to calculate the mechanical properties of Co,

Cr, Fe, Ni and Ti, which were compared to available experimental data. A comparison between the alloy's calculated properties and those of the individual elements was also made.

4.2.3.1. Computational Stress-Strain Curves

Computational stress-strain curves of the alloy and individual elements were produced by simulating a uniaxial tensile strain applied along the $\langle 001 \rangle$ for both the 80-atom SQS cell and the metallic elements unit cells. The unstrained cells were those produced by the structural relaxation. For the strained cells, the lattice parameter was increased in the relevant direction and was fixed throughout the calculation while the remaining two directions were allowed to relax, in addition to relaxing the ions and electrons. The resulting stress in the direction of the applied strain was recorded and used to plot the computational stress-strain curves. The applied strain was increased in increments of 1% up to where the crystal reaches its ideal tensile strength as indicated by the decrease in stress values upon further straining.

From the linear portion of the computed curves ie. the elastic region, the Young's modulus is calculated and is equivalent to the slope of the curve within this region. The Poisson's ratio is also calculated by considering the change in the lattice parameter in the $\langle 100 \rangle$ and $\langle 010 \rangle$ directions to calculate the transverse strain. The Poisson's ratio, ν , can then be determined using the following equation

$$\nu = -\frac{\varepsilon_{trans}}{\varepsilon_{long}} \quad \text{Equation 4.2.5}$$

where ε_{trans} and ε_{long} are the transverse and longitudinal strains, respectively. The longitudinal strain is simply that imposed on the crystal during the simulation. Finally, the ideal strength can also be determined, where it corresponds to the largest stress value achieved. Elastic Constants Analysis

The mechanical properties of the alloy and its constituent elements were also evaluated by determining their SOECs using DFT, which are used to calculate their bulk, shear, and Young's modulus as well as their Poisson's ratio. The SOECs are determined by applying a set of pre-determined deformations, depending on the crystal geometry, to the relaxed structure of the alloy or element of interest. By extracting either energy or stress information from the output of the DFT calculations, the SOECs can be calculated and subsequently the above-mentioned properties are determined. The ElaStic tool [90] was used for generating the DFT input files with the necessary deformations applied. ElaStic was also used to process the DFT output files and calculate the relevant SOECs as well as the Voigt (upper limit), Reus (lower limit), and Hill (average) value of the bulk, shear, and Young's modulus and the Poisson's ratio.

As mentioned, two methods are possible for the elastic constants' analysis described, namely an energy-based approach and a stress-based approach. Since stress calculation is implemented in QUANTUM ESPRESSO, the stress approach is followed in the present study. For the same crystal geometry, less deformations are required for the stress approach compared to the

energy-based one, which makes the stress-based approach computationally efficient and appealing. This is especially important for the more complex structures considered such as HCP Co and Ti as well as the SQS alloy supercell, which is treated as an orthorhombic cell rather than a cubic one.

Chapter 5. Results and Discussion

In this chapter, the results of the current study are presented. First, the constructed computational phase diagrams and the thermodynamic calculations using CALPHAD are given. This is followed by a discussion which examines the phase stabilities in the calculated phase diagrams from a thermodynamic perspective and with a special focus of the single FCC solid solution phase regions in the generated diagrams. The following sections focus on the computational characterization of an FCC HEA, the composition of which was selected from the computed diagrams. Details of the first principles density functional theory (DFT) results and the various analysis approaches followed to obtain the alloy's properties and are then provided.

5.1. Phase Diagrams and Computational Thermodynamics

5.1.1. Computational Phase Diagrams of the CoCrFeNiTi System

In this section, computational phase diagrams of the CoCrFeNiTi alloy system are presented. These diagrams have been generated using the OpenCalphad software [55] and the mc_ni.TDB database [60] using the procedure explained previously Chapter 4. First, the phase diagrams of the $\text{Co}_x\text{CrFeNiTi}_{2-x}$, $\text{CoCr}_x\text{FeNiTi}_{2-x}$, $\text{CoCrFe}_x\text{NiTi}_{2-x}$, and $\text{CoCrFeNi}_x\text{Ti}_{2-x}$ alloys are shown. These were used to study the effect of substituting Ti in equiatomic CoCrFeNiTi by Co, Cr, Fe, and Ni on the alloy's structure.

To the best of our knowledge, this is the first report of extensive phase diagrams of the CoCrFeNiTi HEA system that encompass large composition and temperature ranges. The constructed phase diagrams offer a starting point for systematically designing and studying CoCrFeNiTi alloys by providing insight into the effect of varying alloy composition on the equilibrium phases obtained.

5.1.1.1. General Notes

To avoid confusion, CoCrFeNiTi will be used to refer to the general alloy system, which encompasses all compositions and non-equiatomic subsystems. In case the equiatomic composition is being referred to it will be explicitly stated to avoid confusion with the larger alloy system. Moreover, the $\text{Co}_x\text{CrFeNiTi}_{2-x}$, $\text{CoCr}_x\text{FeNiTi}_{2-x}$, $\text{CoCrFe}_x\text{NiTi}_{2-x}$, and $\text{CoCrFeNi}_x\text{Ti}_{2-x}$ subsystems will be referred to as the Co, Cr, Fe and Ni systems for simplicity.

In the following discussion, when a combination of solid solution and intermetallic phases are present, it is assumed that the solid solution phase is the primary phase, while the intermetallic phases are considered as secondary phases. This assumption is supported by the microstructures reported in literature, which have been reviewed in sections 3.3.1 and 3.3.2.

The diagrams presented in this section have been traced and labeled for presentation and clarity purposes. The raw output from the phase diagram construction procedure is provided in Appendix C. It should also be noted that the distinction between the different types of Laves phases

ie. hexagonal and cubic, was not made in the diagrams since it was not clear from the database used.

Gaining an understanding of the thermodynamic stabilization of single solid solution phases in HEAs is one of the main aims of this study. For that reason, the single FCC phase region in the systems studied as well as its surrounding regions were focused on. The main advantage of having this type of structure is the expected improvement in alloy ductility compared to those with intermetallic phases.

Moreover, Ti is expected to have a solid solution strengthening effect in CoCrFeNiTi alloys [9]. However, most studies also suggest that Ti is a BCC stabilizer, meaning that its presence is more likely to favor the stabilization of solid solution phases with a BCC crystal structure rather than an FCC one. Accordingly, also of interest is the maximum Ti content that still allows for the stabilization of the single FCC phase.

5.1.1.2. $CoCrFeNi_xTi_{2-x}$

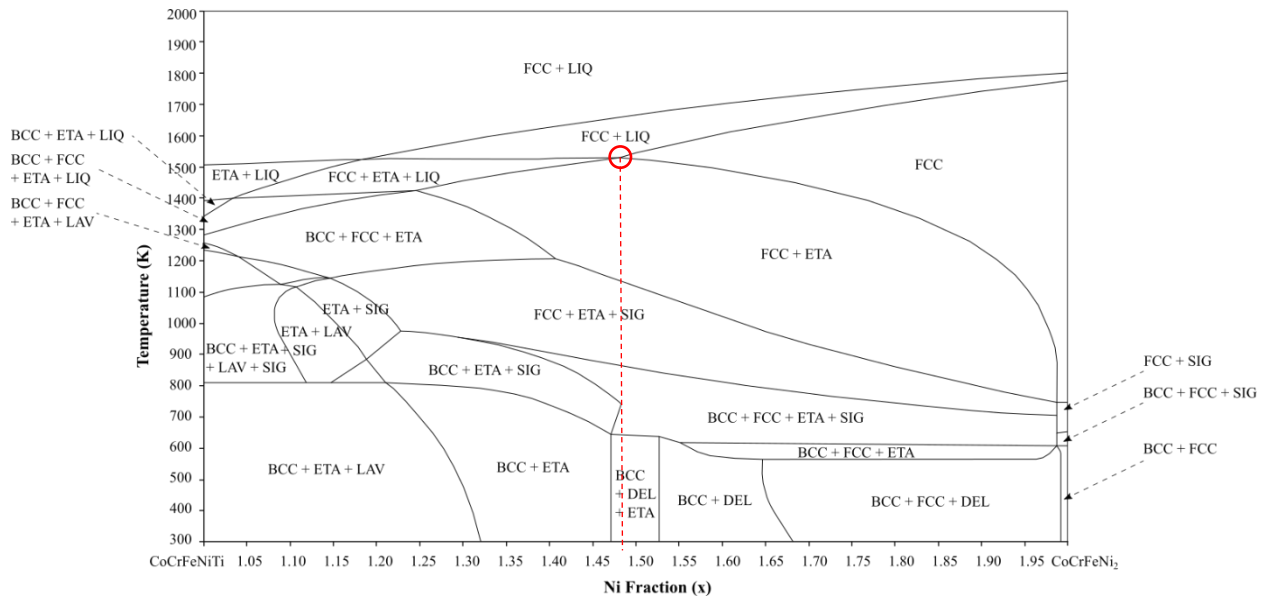


Fig. 5.1.1. The $CoCrFeNi_xTi_{2-x}$ computational phase diagram generated by the CALPHAD method. The values of x range from 1 to 2, where the diagram starts at equiatomic $CoCrFeNiTi$ ($x=1$) and ends at $CoCrFeNi_2$ ($x=2$). The diagram spans a temperature range of 300 K to 2000 K.

The $CoCrFeNi_xTi_{2-x}$ phase diagram in Fig. 5.1.1, shows the changes in the phase stabilities of this alloy system as the concentration of Ni (x) is increased at the expense of Ti ($2-x$). At $x=1$ the composition of the alloy is equiatomic $CoCrFeNiTi$ and at $x=2$ $CoCrFeNi_2$. A general trend exhibited by this system is the stability of a BCC structure as the primary solid solution phase at lower concentrations of Ni (and higher concentrations of Ti) and at lower temperatures. As the Ni concentration and temperature increase, an FCC phase becomes stable in addition to the BCC phase or instead of it. In other HEA systems, Ni has been shown to be an FCC stabilizer [101]. The present results suggest that Ni plays a similar role in the $CoCrFeNiTi$ system. In addition to the primary BCC and FCC solid solution phases, the intermetallic phases present are the delta

(DEL), η (ETA), Laves (LAV), and σ (SIG) phases, which are commonly found in CoCrFeNiTi alloys.

The effect of temperature on the crystal structure of the stable phase should also be emphasized. It has been suggested that in HEAs close-packed structures such as FCC are more likely to form at higher temperatures since at lower temperatures high lattice strains can be better accommodated for in more open structures, such as the BCC crystal structure [102].

In addition to the gradual evolution of the alloy's primary phase from BCC to BCC+FCC to FCC with increasing Ni content and temperature, the CoCrFeNi_xTi_{2-x} system exhibits a large single FCC phase region, which also supports that the presence of Ni in this system more likely favors an FCC structure. The maximum Ti content at which the single FCC phase is stable is approximately 0.52 at $x=1.48$ ie. CoCrFeNi_{1.48}Ti_{0.52} and at 1520 K as shown by the red circle in Fig. 5.1.1. The temperature and composition limits of the single FCC phase are approximately 740 K and 1790 K and $x=1.48$ and $x=2$.

5.1.1.3. Co_xCrFeNiTi_{2-x}

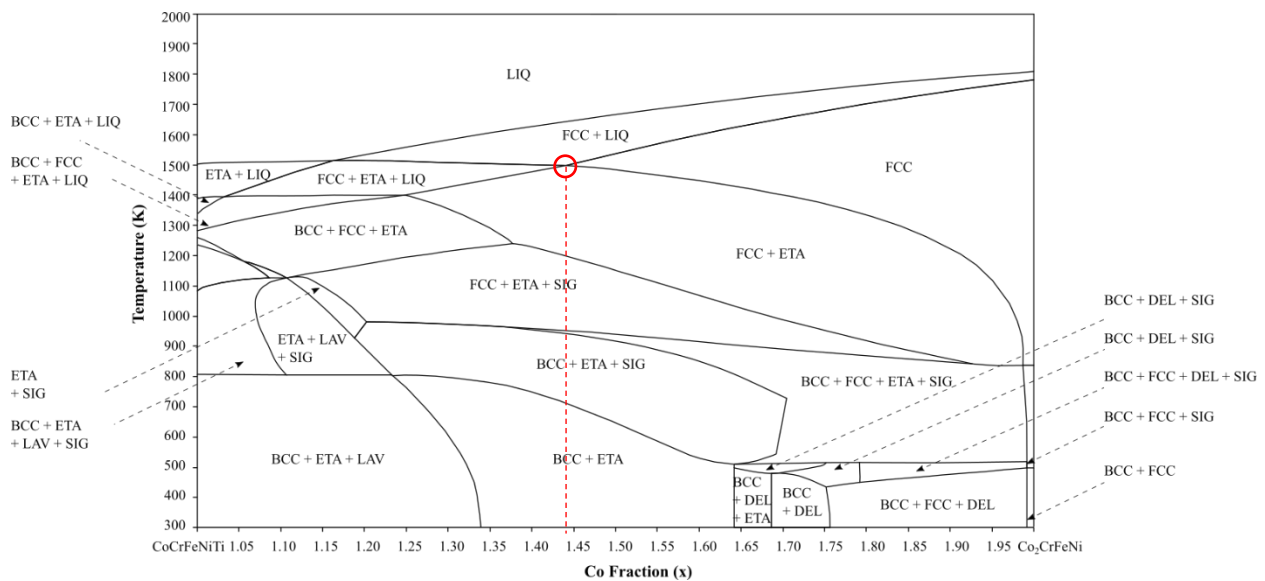


Fig. 5.1.2. The Co_xCrFeNiTi_{2-x} computational phase diagram generated by the CALPHAD method. The values of x range from 1 to 2, where the diagram starts at equiatomic CoCrFeNiTi ($x=1$) and ends at Co₂CrFeNi ($x=2$). The diagram spans a temperature range of 300 K to 2000 K.

The Co_xCrFeNiTi_{2-x} phase diagram is shown in Fig. 5.1.2. In this diagram, the concentration of Co (x) is increased at the expense of Ti ($2-x$) while the remaining elements are kept at an equiatomic ratio. At $x=1$ the composition of the alloy is equiatomic CoCrFeNiTi and at $x=2$ Co₂CrFeNi.

The primary solid solution phases present are BCC, FCC, or a combination of both. The intermetallic phases present are also the delta, η , Laves, and σ phases, similar to the previous diagram. Near the equiatomic CoCrFeNiTi composition at $x=1$, the calculated structures are

mainly combinations of solid solution BCC and intermetallic phases. As the Co concentration increases relative to that of Ti, the FCC solid solution phase is stabilized in addition to the BCC phase. Previous studies have shown that Co is an FCC stabilizer [101] in AlCoCrFeNi alloys and the present results suggest that Co has a similar effect on CoCrFeNiTi alloys as well. Moreover, like the $\text{CoCrFeNi}_x\text{Ti}_{2-x}$, FCC solid solution phases are prevalent at higher temperatures.

As mentioned, the single FCC solid solution region is the prime target of this study. The single FCC region is stable up to a Ti concentration of approximately 0.56 at $x=1.44$ ie. $\text{Co}_{1.44}\text{CrFeNiTi}_{0.56}$ and at 1500 K indicated by the red circle in Fig. 5.1.2. Finally, the single FCC phase is stable between approximately 830 K and 1790 K depending the concentration of Co and Ti between $x=1.44$ and $x=2$.

5.1.1.4. $\text{CoCrFe}_x\text{NiTi}_{2-x}$

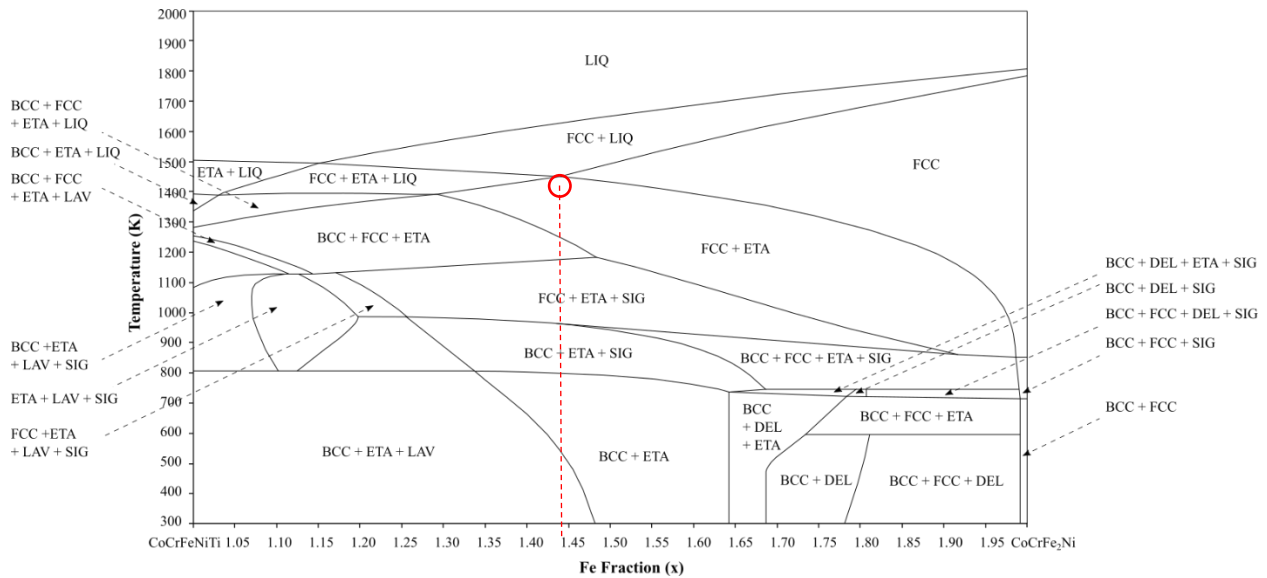


Fig. 5.1.3. The $\text{CoCrFe}_x\text{NiTi}_{2-x}$ computational phase diagram generated by the CALPHAD method. The values of x range from 1 to 2, where the diagram starts at equiatomic CoCrFeNiTi ($x=1$) and ends at CoCr_2FeNi ($x=2$). The diagram spans a temperature range of 300 K to 2000 K.

The $\text{CoCrFe}_x\text{NiTi}_{2-x}$ is shown in Fig. 5.1.3. The composition and temperature ranges are similar to the previous diagrams however, in this case the concentration of Fe (x) is increased at the expense of that of Ti ($2-x$). The resulting phase diagram bears a lot of resemblance to those of the $\text{CoCrFeNi}_x\text{Ti}_{2-x}$ and $\text{Co}_x\text{CrFeNiTi}_{2-x}$ in terms of the phases stabilized with the main differences being in the size of the different phase regions. Accordingly, the primary solid solution structures in the different phase regions are also BCC, FCC, or both and the intermetallic phases present are also delta, η , laves, and σ .

In the AlCoCrFeNi HEA system, Fe was found to have a neutral effect on stabilizing or destabilizing either BCC or FCC solid solution phases [101]. However, the phase diagram in Fig. 5.1.3 suggests that Fe is likely an FCC stabilizer in CoCrFeNiTi alloys. This claim is supported by

5.1.4. The single FCC phase is stable between approximately 1310 K and 1670 K and $x=1.8$ and $x=2$. It is useful to note that a larger concentration of Cr is needed to counter the BCC stabilizing effects of Ti compared to the remaining elements, which supports that Cr itself is a BCC stabilizer. Also, the single FCC phase in this system is only stable over a small temperature and composition range compared to the remaining systems. This is clear from the summary of the single FCC region limits presented in Table 5.1.1.

Since the CoCrFeNiTi HEAs are often studied as candidates for strong and ductile alloys, the present results suggest that it could be favorable to study the effect of reducing the Cr content in CoCrFeNiTi alloys to further promote the formation of FCC structures rather than BCC ones. This is because BCC phases generally tend to have lower ductility compared to FCC ones. It would also be useful to delineate the contributions of Ti and Cr to the stabilization of the BCC phase in these alloys for further understanding the individual role of each element.

5.1.1.6. Discussion

Based on the phase diagrams presented, it can be seen that the majority of alloy compositions lead to multi-phase structures rather than single phase structures. Accordingly, the availability of computational phase diagrams, even if their accuracy is limited, is necessary to be able to narrow down the composition ranges in which a single solid solution structure could be stabilized via a suitable processing technique. This would save much of the time and resources that would go into trial and error methods. In addition to helping to target single-phase alloys, the availability of such extensive phase diagrams would allow for designing multi-phase alloys with tailored structures for desired applications.

The similarities between the phase diagrams of the Co, Fe, and Ni systems and their limits of the single FCC phase region (summarized in Table 5.1.1) suggest that these elements have similar effects on the phase stabilities of CoCrFeNiTi alloys. This can have important consequences since Co is expensive and attempts have been made to decrease the Co content to reduce the cost of CoCrFeNiTi alloys. However, reducing the Co content in $\text{Co}_x\text{CrFeNiTi}_{0.3}$ has been found to increase the volume fraction of the $\eta + \sigma$ duplex phase, which led to an increase in alloy hardness but decreased its compressive strength and ductility [75]. To further understand the effect of each element on the amount of η and σ phases, CALPHAD was used in the present study to calculate and plot the mole fraction of the η and σ phases in the FCC+ETA+SIG region at 1100 K as a function of Co, Fe, and Ni content in $\text{Co}_x\text{CrFeNiTi}_{2-x}$, $\text{CoCrFe}_x\text{NiTi}_{2-x}$, and $\text{CoCrFeNi}_x\text{Ti}_{2-x}$, respectively. These plots are shown in Fig. 5.1.5 (a), (b), and (c), which show that decreasing the content of any of the three elements leads to an increase in the amount of both η and σ , which agrees with the findings in [75]. The sums of both phase amounts ie. $\eta + \sigma$ were also plotted in Fig. 5.1.5 (d), which shows that all three elements have a similar effect on the total amount of the η and σ phases.

Another important observation is that when the content of any element is 1.25 the total amount of η and σ is almost 0.9, which means that only approximately 10% of the alloy is the FCC

phase. This can be problematic since such an increase in the fraction of intermetallic phases could be detrimental to the alloy mechanical properties as shown in [75]. Accordingly, if a multi-phase structure is being targeted it would be useful to also consider the relative amounts of phases present and their effect on alloy properties to aid with composition selection.

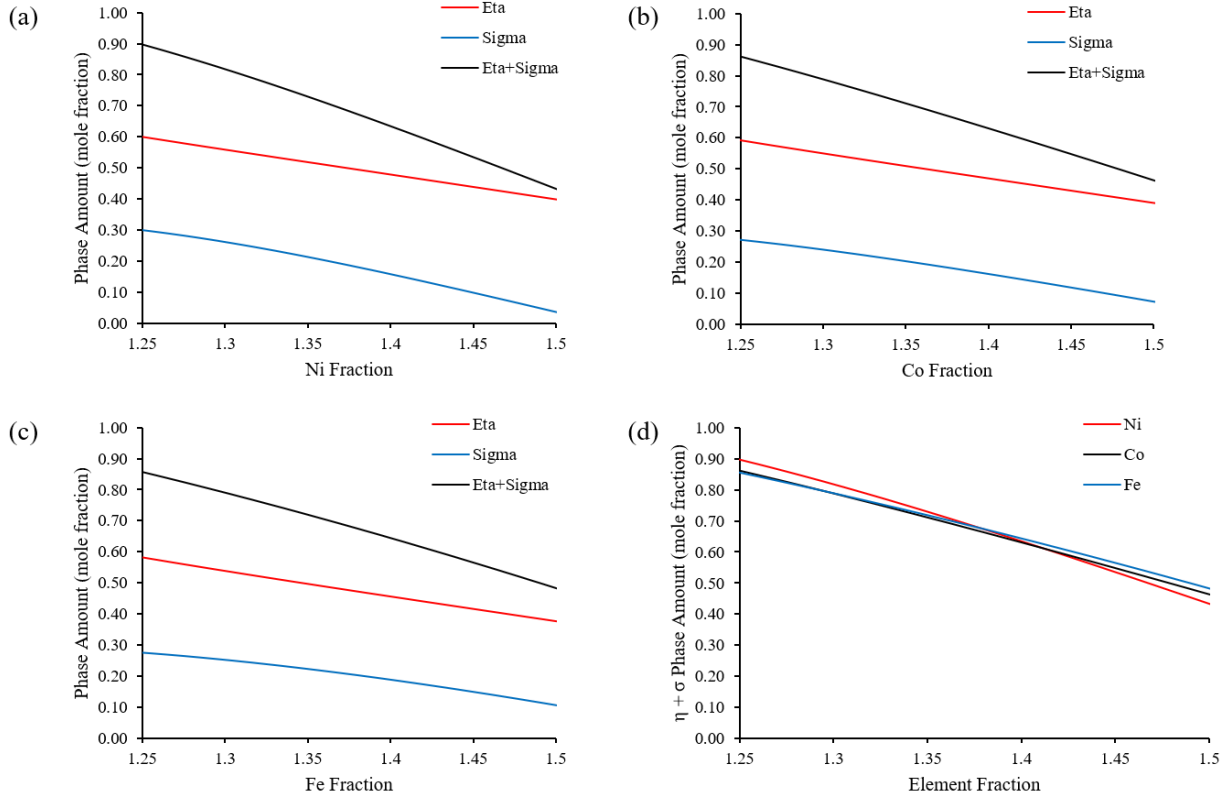


Fig. 5.1.5. Phase fractions of the eta (η) and sigma (σ) phases in the FCC+ETA+SIG phase region at 1100 K as a function of (a) Ni content in $\text{CoCrFeNi}_x\text{Ti}_{2-x}$ (b) Co content in $\text{Co}_x\text{CrFeNi}_x\text{Ti}_{2-x}$ and (c) Fe content in $\text{CoCrFe}_x\text{Ni}_x\text{Ti}_{2-x}$ (d) Total amount of the eta and sigma phases ie. $\eta + \sigma$ in each system. The phase amounts are calculated using CALPHAD.

Table 5.1.1. Summary of the single FCC phase region limits in the $\text{Co}_x\text{CrFeNi}_x\text{Ti}_{2-x}$, $\text{CoCr}_x\text{FeNi}_x\text{Ti}_{2-x}$, $\text{CoCrFe}_x\text{Ni}_x\text{Ti}_{2-x}$, and $\text{CoCrFeNi}_x\text{Ti}_{2-x}$ alloy systems. T_{\min} and T_{\max} are the lower and upper temperature bounds. x_{\min} and x_{\max} are the lower and upper composition bounds.

Alloy System	T_{\min} (K)	T_{\max} (K)	x_{\min}	x_{\max}
$\text{CoCrFeNi}_x\text{Ti}_{2-x}$	740	1790	1.48	2
$\text{Co}_x\text{CrFeNi}_x\text{Ti}_{2-x}$	830	1790	1.44	2
$\text{CoCr}_x\text{FeNi}_x\text{Ti}_{2-x}$	1310	1670	1.80	2
$\text{CoCrFe}_x\text{Ni}_x\text{Ti}_{2-x}$	850	1790	1.44	2

Other approaches to reducing the cost of CoCrFeNiTi alloys include substituting Co for a less expensive element like Ni. For instance, it was previously found that substituting Co with Ni in $\text{Co}_{1-x}\text{CrFeNi}_{1+x}\text{Ti}_{0.3}$ ($x = 0, 0.5, \text{ and } 1$) resulted in an increase in alloy hardness, yield strength,

and ultimate tensile strength and a decrease in ductility although the microstructures of all the tested alloys consisted of a single FCC phase [76]. Accordingly, the effect of such a substitution on the relative phase amounts is not clear. It was suggested that the obtained alloy properties could be explained by the larger enthalpy of mixing between Ni and the remaining elements compared to their enthalpy of mixing with Co, which leads to an increase in the number of stronger bonds (eg. Ni-Ti and Ni-Cr).

Based on our results, which indicate that Ni, Co, and Fe have similar effects on the phase stabilities of alloys in the CoCrFeNiTi systems and the enthalpy of mixing values [9] shown in Table 5.1.2, substituting Co with Fe could yield more favorable results with regards to alloy ductility compared to substituting with Ni. This substitution would also lead to a reduction in alloy cost while also helping to shed more light on the effect of substituting different elements for one another on the resulting properties. Such insight would be valuable as it would allow for further tailoring of alloy structure and properties for various.

Table 5.1.2. Enthalpy of mixing (kJ/mol) of element pairs in the CoCrFeNiTi HEA system [9]

	Co	Cr	Fe	Ni	Ti
Co	0	-4	-1	0	-28
Cr	-	0	-1	-7	-7
Fe	-	-	0	-2	-17
Ni	-	-	-	0	-35
Ti	-	-	-	-	0

5.1.2. Thermodynamic Analysis

The following equation (previously discussed in section 2.2.2) has been central to explaining phase stabilities in HEAs

$$\Delta G_{mix} = \Delta H_{mix} - T\Delta S_{mix}$$

In an ideal solution, the only mixing entropy ΔS_{mix} contribution is that of the configurational entropy such that $\Delta S_{mix} = \Delta S_{conf}$ and the mixing enthalpy ΔH_{mix} is zero. On the other hand, in non-ideal solutions there is an excess entropy, which can consist of vibrational, electronic, or magnetic contributions as well as any combination of these. Large values of ΔH_{mix} , whether positive or negative can lead to atomic clustering or ordering, respectively [8]. Generally, any deviation from the ideal thermodynamic behavior will tend to favor a multi-phase alloy structure rather than a single solid solution phase. However, when the magnitude of ΔS_{mix} is increased compared to that of ΔH_{mix} , there is a higher tendency for the system to form a single solid solution phase.

As previously discussed, the large configurational entropy resulting from the multi-principal element nature of HEAs was originally believed to be sufficient to overcome the ordering and phase separation effects of ΔH_{mix} and would result in the stabilization of single-phase solid solution structures in HEAs [1]. However, studies have shown that this is often not the case since commonly followed approaches greatly simplify the thermodynamics of HEAs. One of the most severe simplifications is the treatment of HEAs as ideal mixtures or solutions, which most real alloys are not. Accordingly, a number of studies [1], [31], [40], [44], [103]–[105] have been dedicated to investigating and developing the thermodynamic theory of HEAs to further understand their phase stabilities, structures, and properties.

In this section, a thermodynamic explanation of the computational phase diagrams presented in section 5.1.1 is given through an analysis of the variation of ΔH_{mix} and ΔS_{mix} as a function of alloy composition in the Ni, Co, Fe, and Cr systems. Two approaches for this analysis are followed. The first considers the variation of the overall mixing enthalpy and entropy within the temperature range that encompasses the single FCC solid solution phase. The second approach considers the calculated deviation of ΔH_{mix} and ΔS_{mix} from those of an ideal solution. The aim of both these methods of analysis is to gain further insight into the underlying thermodynamic factors that contribute to the stability of single solid solution phases in HEAs.

5.1.2.1. The Mixing Enthalpy and Entropy

One of the main ambiguities in the thermodynamic theory of HEAs to date is that many of the developed theoretical frameworks discuss the competition between solid solution and intermetallic phases assuming that an alloy with a given composition will form only one of the two. Such approaches separately consider the energy of formation of a solid solution and an intermetallic phase. However, both experimental and computational studies have shown it is more likely that intermetallic phases will precipitate as secondary phases from primary solid solution phases and the overall system energy would therefore be the sum of both energies [8]. For this reason, the present study considers the overall system enthalpy and entropy values for an explanation of the phase stabilities shown in the calculated phase diagrams.

The ΔH_{mix} and ΔS_{mix} values of the alloys in the Ni, Co, Fe, and Cr systems were calculated by subtracting the elemental contributions from the overall system enthalpies and entropies from the CALPHAD output. Special focus was placed on the variation of these properties close to and within the single FCC phase region as it is the main region of interest. Accordingly, the enthalpy and entropy values of all systems were plotted as a function of alloy composition at temperatures ranging from 1100 K to 1700 K which encompass the single FCC phase region and the phase regions right above and below it.

The variation of ΔH_{mix} as a function of alloy composition in the systems of interest is shown in Fig. 5.1.6. At a given temperature, ΔH_{mix} is continuously increasing or decreasing within a phase region and abrupt changes are observed at the boundaries where a phase change occurs. Accordingly, the kinks in the ΔH_{mix} plots correspond to the points along the tie lines in the phase

diagrams where there is a phase transition. Between 1100 K and 1300 K, the alloys possess the largest magnitudes of ΔH_{mix} at all temperatures, which reach up to -18.36 kJ at 1200 K for equiatomic CoCrFeNiTi. Within this temperature range, ΔH_{mix} generally tends to increase (decrease in magnitude) continuously with increasing the concentration of Ni, Co, Fe, and Cr until it becomes positive. A different trend is observed for ΔH_{mix} at 1400 K, which seems to be a transition temperature for the overall behavior of the different systems. At 1500 K and 1600 K, the ΔH_{mix} values are generally smaller in magnitude than those at lower temperatures. At 1700 K, the plots are similar for the Ni, Co, and Fe system, where ΔH_{mix} increases reaching its maximum value at the boundary between the LIQ and FCC+LIQ phases and then decreases to reach its minimum at the boundary between the FCC+LIQ and FCC phases. On the other hand, in the Cr system at 1700 K the alloy is completely liquid regardless of its composition, which explains the different shape of the ΔH_{mix} plot at this temperature. Within the regions in the plots that correspond to the single FCC phase, ΔH_{mix} varies only slightly as a function of temperature and composition. Within this region, the magnitudes of ΔH_{mix} are generally small reaching a maximum of 1.80 kJ for the Ni system; 3.67 kJ for the Co system; 2.97 kJ for Fe system; and 3.84 kJ for Cr system at $x=2$ and 1100 K. It can be seen that there is a significant difference in ΔH_{mix} between the multi-phase structure present at $x=1$ and the single FCC phase alloy at larger element concentrations, where the latter are small positive values and the former are larger negative values.

The mixing entropy ΔS_{mix} , shown in Fig. 5.1.7 for the Ni, Co, Fe, and Cr systems. Similar to the mixing enthalpy plots, ΔS_{mix} is also exhibits abrupt changes at the phase boundaries for a given temperature. The ΔS_{mix} values increase with increasing temperature except in the region in which the single FCC phase is present, where the ΔS_{mix} values are approximately equal or differ only slightly. For example, in the Ni system ΔS_{mix} is greatest between 1500K and 1700K; intermediate at 1400 K; and the least between 1100 K and 1300 K. This is also true for the Co and Cr systems, however, no distinct trend can be identified for ΔS_{mix} in the high temperature range (1500 K–1700 K) of the Fe system, which could be a result of some type of magnetic behavior that arises as the concentration of Fe is increased. The ΔS_{mix} values calculated consist of both configurational and excess contributions such as vibrational, electronic, and magnetic entropy. The extent of the excess entropy, which represents the deviation from ideal solution behavior, and its implications on alloy phase stability will be discussed in detail in the coming section. However, the increase in ΔS_{mix} with increase in temperature indicates a considerable vibrational entropy contribution, while the almost overlapping ΔS_{mix} plots in the FCC phase region indicate that the mixing entropy is mainly configurational i.e. very close to ideal solid solution behavior [104].

The ratio of ΔH_{mix} to $T.\Delta S_{\text{mix}}$ was also calculated and is shown in Fig. 5.1.8. The quantity $T.\Delta S_{\text{mix}}$ is the product of the mixing entropy and the temperature under consideration. This quantity is used for the comparison rather than ΔS_{mix} due to the important role of temperature in the entropy contribution to ΔG_{mix} since the magnitude of the entropy component is usually only comparable to that of the enthalpy due to the multiplication by temperature. This ratio is calculated

to compare the relative magnitudes of enthalpy and entropy to the Gibbs energy of the systems to determine the relative importance of each to the phase stabilities of the alloys of interest.

At the temperatures studied, $\Delta H_{\text{mix}}/T \cdot \Delta S_{\text{mix}}$ decreases with increasing temperature. This is expected since in addition to the increase in temperature, ΔS_{mix} also tends to be larger at higher temperatures, as seen from Fig. 5.1.6. For all systems, the $\Delta H_{\text{mix}}/T \cdot \Delta S_{\text{mix}}$ values are generally smaller in the 1500 K-1700 K temperature range compared to those between 1100 K and 1300 K, with the values as 1400 K in between. This can be attributed to the presence of a liquid phase in addition to solid solution and intermetallic phases in all regions in the phase diagram along the tie lines in the high temperature range except in that of the single FCC phase. Since the liquid phase is expected to possess a large mixing entropy compared to the solid solution and intermetallic phases, it is expected that the entropy contribution should dominate where the liquid phase is present. The results between 1500 K and 1700 K in the Fe system (Fig. 5.1.8 (c)) are expected to be affected by the anomalous ΔS_{mix} behavior as previously discussed.

The single FCC phase composition range is also another region with consistently lower values of $\Delta H_{\text{mix}}/T \cdot \Delta S_{\text{mix}}$ at all temperatures. This aligns with the expected behavior of the thermodynamic properties, which suggests that the single FCC solid solution phase would only be stabilized if the entropy contribution sufficiently dominates the Gibbs energy of the system [106]. This is especially clear from the $\Delta H_{\text{mix}}/T \cdot \Delta S_{\text{mix}}$ plot at 1300 K in the Ni system shown in Fig. 5.1.8 (a). Between $x=1.025$ and $x=1.36$, which corresponds to the BCC+FCC+ETA phase, $\Delta H_{\text{mix}}/T \cdot \Delta S_{\text{mix}}$ is greatest and exhibits values greater than unity, indicating that the ΔH_{mix} contribution dominates ΔG_{mix} . Between $x=1.36$ and $x=1.865$, $\Delta H_{\text{mix}}/T \cdot \Delta S_{\text{mix}}$ decreases as the entropy contribution starts prevailing in the FCC+ETA region until it becomes sufficient to stabilize the single FCC phase at $x=1.865$ and $\Delta H_{\text{mix}}/T \cdot \Delta S_{\text{mix}}=0.0284$. Within the single FCC phase region $\Delta H_{\text{mix}}/T \cdot \Delta S_{\text{mix}}$ continues to decrease until it reaches a minimum of 0.0006 at $x=1.905$ after which it increases again to 0.0634 at $x=2$. The Fe system at 1300 K exhibits the same trend in $\Delta H_{\text{mix}}/T \cdot \Delta S_{\text{mix}}$ while in the Co and Cr systems, the minimum $\Delta H_{\text{mix}}/T \cdot \Delta S_{\text{mix}}$ occurs in the FCC+ETA and BCC+FCC+ETA regions, respectively, rather than in the single FCC phase region.

5.1.2.2. *The Deviation of the Thermodynamic Properties from the Ideal Solid Solution Behavior*

To further understand the stabilization of the single FCC solid solution phase in the CoCrFeNiTi HEA system, the deviation of the mixing enthalpy and entropy from those of an ideal solution was considered. As previously discussed, an ideal solution is one in which its constituent elements are randomly distributed within its lattice sites with no preferential occupation or ordering. Thermodynamically, the mixing enthalpy of such phases would be zero and the only entropic contribution to their Gibbs energy would be that of the configurational entropy. Systems that deviate from this behavior tend to exhibit multi-phase structures with ordered phases, such as intermetallic phases, rather than single solid solution structures. Real alloys are mostly non-ideal systems, however, the magnitude of the deviation from the ideal solution thermodynamic behavior has an important impact on determining their resulting structure as shown in [44]. Accordingly,

calculating and analyzing the extent of the departure from ideal behavior can provide additional insight into the stabilization of the single FCC solid solution phase.

Since ΔH_{mix} of an ideal solution is zero, its deviation from ideal behavior is the same as the value of ΔH_{mix} calculated for a given alloy composition and temperature. Accordingly, the plots of the mixing enthalpy deviation are the same as those of ΔH_{mix} shown in Fig. 5.1.6. Apart from the single FCC phase region, the alloys in all systems exhibit the largest deviation at 1100 K-1300 K near the equiatomic CoCrFeNiTi composition ($x=1$). In the Ni and Fe systems (Fig. 5.1.6 (a) and (c)), comparing structures that are completely solid i.e. those that do not include a liquid phase in addition to their solid solution and/or intermetallic phases, shows that the deviation of ΔH_{mix} is smallest within the single FCC phase region compared to that in other multi-phase regions. This aligns with the expected alloy behavior since large positive or negative values of ΔH_{mix} lead to elemental segregation and multi-phase structures [40]. The Co system (Fig. 5.1.6 (b)) exhibits a slightly different behavior between 1100 K and 1300 K, where although the ΔH_{mix} deviation is also smallest within the FCC phase region, the ideal behavior (where deviation is zero) occurs within the region corresponding to the FCC+ETA phase. The Cr system (Fig. 5.1.6 (d)) displays similar behavior in addition to the observation that the ΔH_{mix} , and hence the deviation from ideal behavior, is approximately equal at all temperatures in the BCC+FCC and FCC phase regions.

For an alloy with a given composition, the deviation of its mixing entropy from that of an ideal solution is obtained by subtracting from it the ideal configurational entropy. The magnitude of the ΔS_{mix} deviation is therefore a measure of the non-ideal entropy contributions to ΔG_{mix} . The calculated entropy deviation for the Ni, Co, Fe, and Cr systems is shown in Fig. 5.1.9.

The deviation of ΔS_{mix} from the ideal behavior exhibits similar trends to that of ΔH_{mix} , where the largest deviation of the entropy in all systems occurs in the composition ranges where multi-phase structures are stable. Moreover, the alloys exhibit the least deviation within and near the single solid solution phase region in the Ni, Co, and Fe systems and BCC+FCC and FCC in the Cr system. This also indicates that configurational entropy plays a vital role in promoting the stabilization of solid solution structures rather than ordered ones such as intermetallic phases. The small deviation of ΔS_{mix} from the ideal behavior indicates that ΔS_{mix} is largely configurational, which decreases the possibility for other non-ideal entropic contributions that could destabilize the solid solution structure [40].

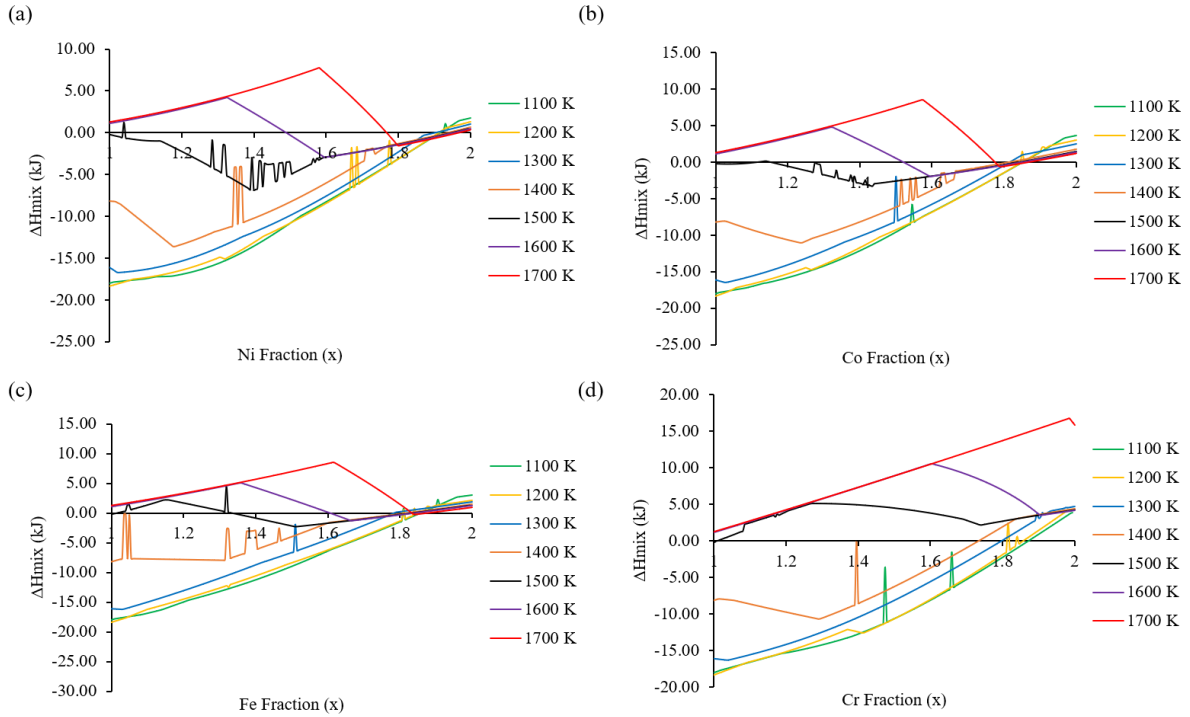


Fig. 5.1.6. Mixing Enthalpy, ΔH_{mix} , as a function of element concentration, x , in (a) $\text{CoCrFeNi}_x\text{Ti}_{2-x}$ (b) $\text{Co}_x\text{CrFeNiTi}_{2-x}$ (c) $\text{CoCrFe}_x\text{NiTi}_{2-x}$ (d) $\text{CoCr}_x\text{FeNiTi}_{2-x}$

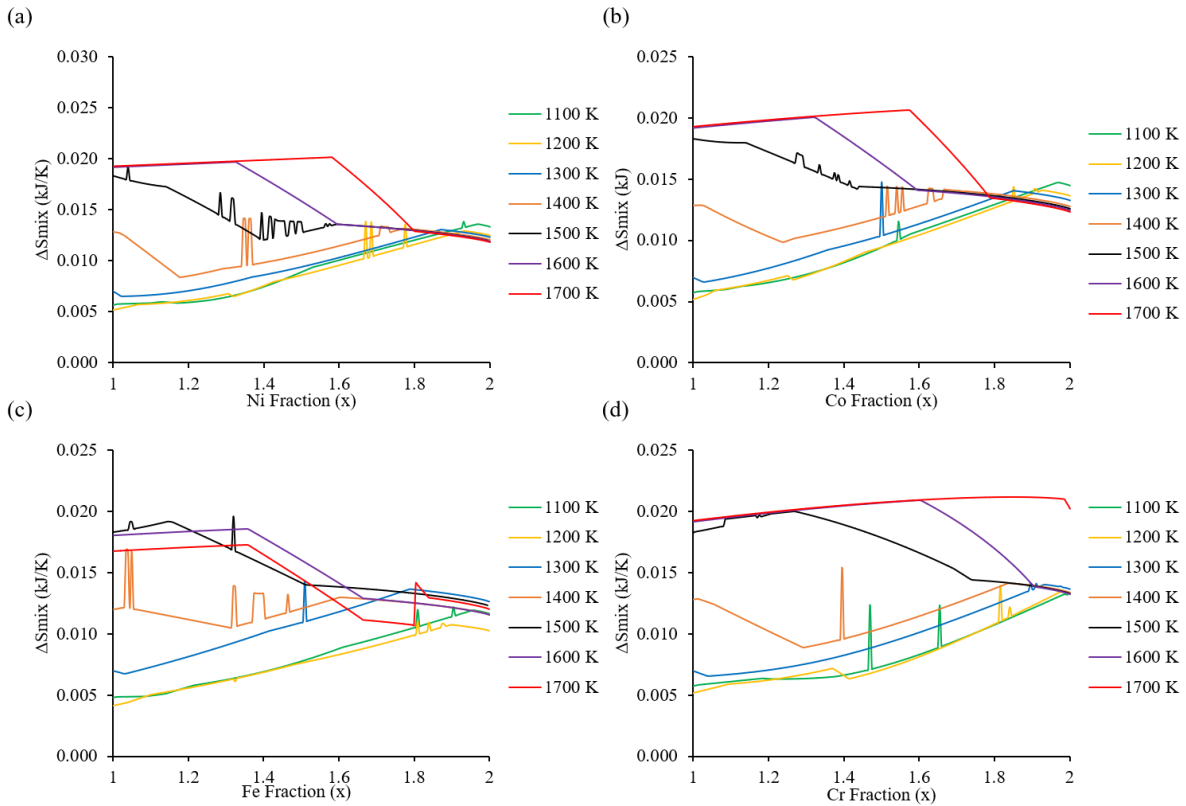


Fig. 5.1.7. Mixing Entropy, ΔS_{mix} , as a function of element concentration, x , in (a) $\text{CoCrFeNi}_x\text{Ti}_{2-x}$ (b) $\text{Co}_x\text{CrFeNiTi}_{2-x}$ (c) $\text{CoCrFe}_x\text{NiTi}_{2-x}$ (d) $\text{CoCr}_x\text{FeNiTi}_{2-x}$

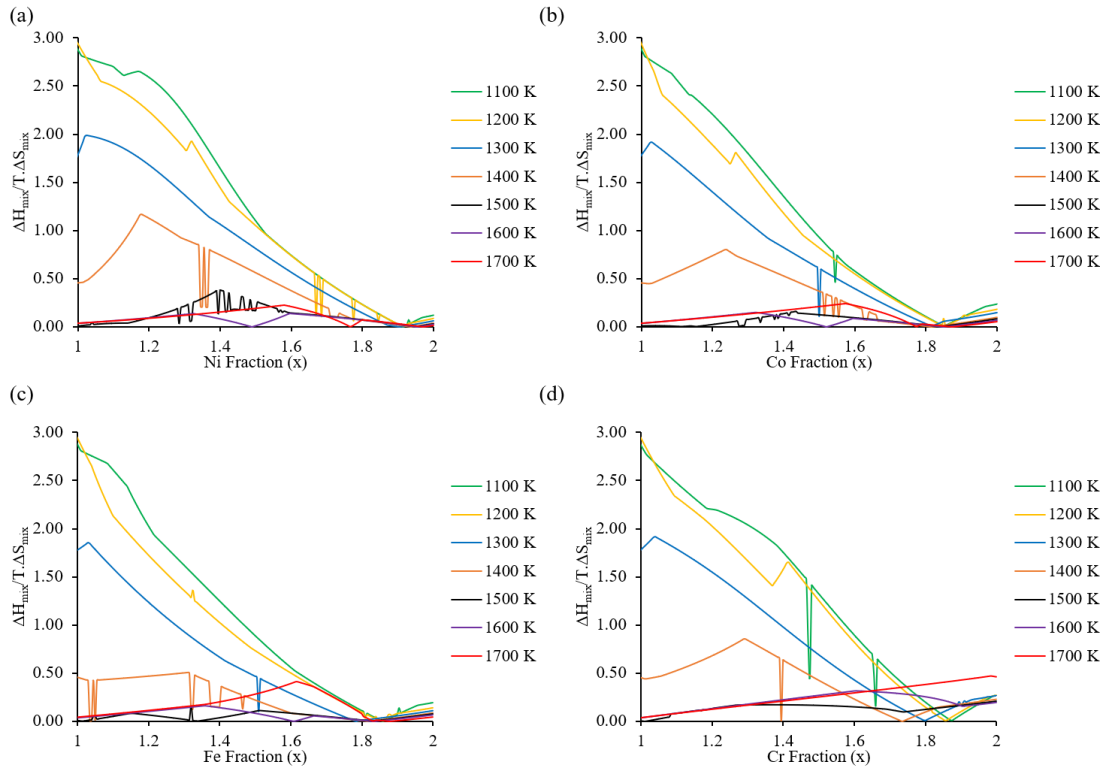


Fig. 5.1.8. The ratio of ΔH_{mix} to $T\Delta S_{\text{mix}}$, as a function of element concentration, x , in (a) CoCrFeNi_xTi_{2-x} (b) Co_xCrFeNiTi_{2-x} (c) CoCrFe_xNiTi_{2-x} (d) CoCr_xFeNiTi_{2-x}

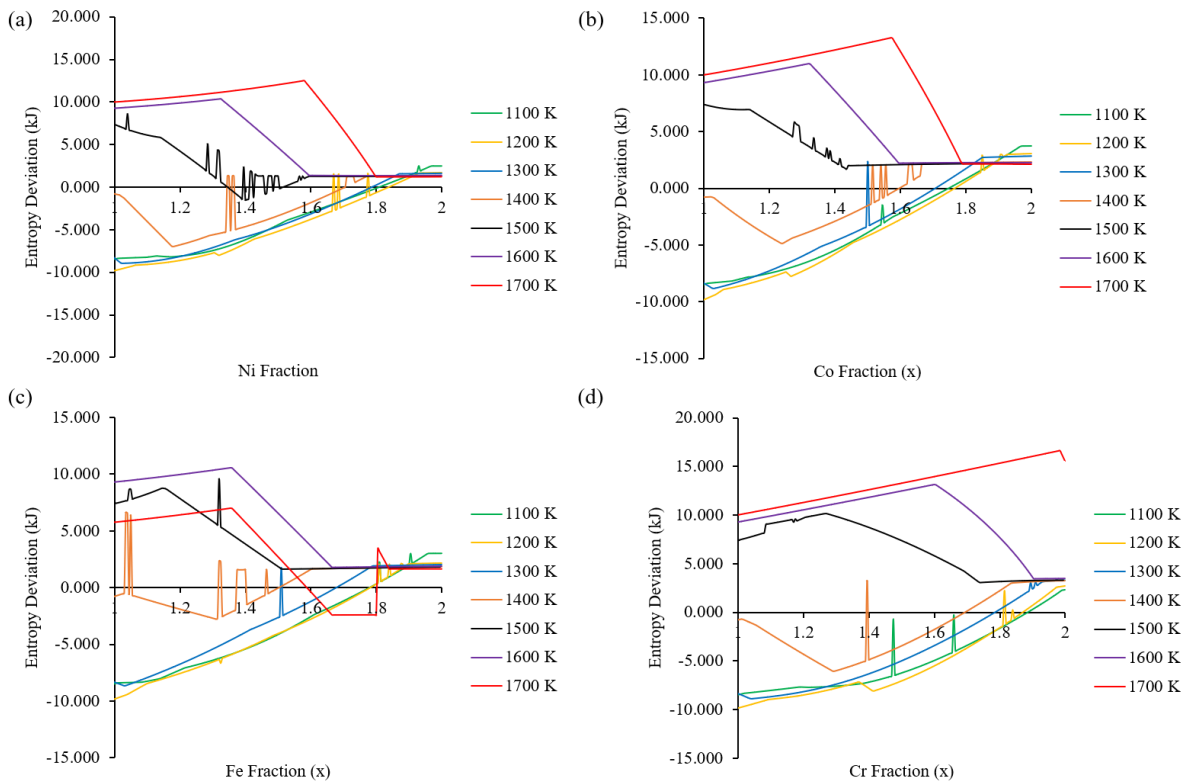


Fig. 5.1.9. The deviation of $T\Delta S_{\text{mix}}$, from the ideal solid solution behavior as a function of element concentration, x , in (a) CoCrFeNi_xTi_{2-x} (b) Co_xCrFeNiTi_{2-x} (c) CoCrFe_xNiTi_{2-x} (d) CoCr_xFeNiTi_{2-x}

5.1.2.3. Discussion of the Thermodynamic Behavior of the Alloy Systems and the Stabilization of the Single FCC Solid Solution Phase

The thermodynamic properties of the alloy systems studied were calculated and analyzed. Coupling thermodynamic calculations with phase diagram interpretation can help with identifying links between thermodynamic properties and phase stabilities. If such links are established, thermodynamic property calculations using CALPHAD can offer an intermediate approach between parametric approaches and the construction of full phase diagrams, which can be complicated. For example, one interesting observation is the similarity between the thermodynamic properties of the Ni, Co, and Fe systems, which could explain the similarities in their phase stabilities as reflected in their corresponding phase diagrams.

It should also be noted that at a given temperature the changes in the thermodynamic properties and their consequences on the phase stabilities are only a function of composition. This emphasizes the importance of exploring non-equiatomically alloy compositions, that can have very different thermodynamic and ultimately structural and mechanical properties than those of equiatomically alloys. For instance, in the case of the present results, the desired single FCC phase is only present far from equiatomically CoCrFeNiTi as the concentration of Ti decreases in all four systems studied. This behavior can be explained by the large chemical incompatibility between Ti and the remaining elements indicated by the large ΔH_{mix} values of their binaries shown in Table 5.1.2. This can also explain the large overall ΔH_{mix} (Fig. 5.1.6) exhibited by the alloys in the studied systems with compositions containing large Ti concentrations. These deviate the most from the ideal solid solution behavior, which is likely the cause of the multi-phase structures stable in such regions of the phase diagrams. The present findings align with those of Otto et al. [44], who reported similar deviations from ideal solution behavior for equiatomically Ti-Cr, Ti-Fe, and Ti-Ni binary alloys.

Moreover, $T \cdot \Delta S_{\text{mix}}$ values in regions with large Ti contents tend to be much smaller relative to ΔH_{mix} , as shown by the $\Delta H_{\text{mix}}/T \cdot \Delta S_{\text{mix}}$ plots in Fig. 5.1.8. The entropy deviations in these composition ranges are also largest, indicating the overall behavior of the system is far from ideal and unlikely to stabilize a single solid solution phase.

It was suggested by Miracle et al. [29] that the electronic entropy contribution in HEAs is negligible. Manzoor et al. [40] later confirmed using DFT calculations that the entropies of binaries of common elements in HEAs mainly consisted of configurational and vibrational entropies with a minor electronic component that had no significant effect on the alloys' phase stabilities. Accordingly, it will be assumed that the electronic entropy can be ignored, such that the main entropy contributions are the ideal configurational entropy in addition to the non-ideal excess configurational and vibrational entropies.

In Fig. 5.1.6, the overlap of most ΔS_{mix} plots within the single FCC phase region, despite the differences in the system temperature, indicates that the main entropy contribution is configurational. This is in contrast to the remaining phase regions in which the overall system

entropy consistently increases with increasing temperature, which indicates that the alloys possess a significant vibrational entropy contribution since vibrational entropy is sensitive to increases in temperature [29], [104]. Moreover, this suggests that in addition to a vibrational component, the excess entropy within the single-phase FCC region likely has a significant configurational component. Excess configurational entropy can result due to atomic size mismatches, atomic clustering, in addition to any short-range ordering (SRO) in the solid solution [8], [29]. The presence of excess configurational entropy indicates that the single FCC solid solution phase is a real solution. Also, its stabilization within the corresponding composition range can be explained by the deviation of the thermodynamic properties of the system being sufficiently small to allow it. While further studies of the various entropy contributions in higher-order, multi-component alloy systems would help delineate the roles of each entropy component on their phase stabilities, these are often too difficult to accomplish. However, it is commonly accepted that binary calculations provide sufficient information as first steps in HEA design, that in addition to their being much simpler, warrant their importance and use [31], [103].

Otto et al. [44] studied the amount of allowable deviation from ideal behavior which would still result in a single solid solution phase in the constituent binaries of the CoCrFeMnNi HEA system as well as the binaries of some of the constituent elements with Ti, Mo, V, and Cu. The CALPHAD method was used to calculate the system enthalpy, entropy, and Gibbs energy and their deviation from their ideal values. Their work showed that the configurational entropy is only sufficient to suppress the formation of intermetallic compounds if the deviation from the ideal behavior is small enough to allow it. While the study was focused on evaluating the properties of binary equiatomic alloys, the present results for the higher-order CoCrFeNiTi alloys supports the study's findings.

Table 5.1.3 shows the enthalpy and entropy deviation at $x=2$ and 1300 K in the studied systems, which represent the maximum values within the solid solution composition range at this temperature. In the Ni, Co, and Fe system this corresponds to the single FCC region, while in the Cr system a BCC+FCC phase is stable at this composition and temperature. From the results it can be seen that the CoCrFeNi₂ alloy shows the least deviation in terms of both enthalpy and entropy, followed by CoCrFe₂Ni, and then Co₂CrFeNi. On the other hand, the BCC+FCC CoCr₂FeNi alloy shows the largest deviation of all the alloys. This trend is also observed throughout the rest of the solid solution phase regions in all systems. The values obtained are also compared to those obtained by Otto et al. [44] for the single FCC phase CoCrFeMnNi at 1273 K, and were found to be in good agreement for all alloys except the Cr alloy.

Finally, based on the above discussion, our results suggest that the single solid solution phase is stabilized in alloys where two main conditions are met These are:

- (i) A sufficiently small deviation from the ideal solid solution thermodynamic behavior. The analysis of the thermodynamic properties over a wide temperature range indicates that in addition to the important role of high temperature, the composition of the alloy plays a

major role in determining their thermodynamic behavior. As mentioned, this warrants the extensive exploration of non-equiatom alloy compositions for a given alloy system, which would only be possible through computational means such as those pursued in the present study.

- (ii) A significant contribution of the configurational entropy. Our thermodynamic analysis supports the original premise of HEAs introduced by Yeh et al. [1] and the results of Otto et al. [44], who proposed that although it is unlikely in most cases, there exists certain alloys in which configurational entropy is capable of overcoming phase separation effects. Again, the ability to identify such compositions depends on the availability of proficient computational models and methods, which are needed to be able to navigate the massive search space of HEAs.

Table 5.1.3. Maximum enthalpy and entropy deviation of single FCC solid solution in the Ni, Co, Fe, and

Present Study¹			Otto et al. [44]²	
System	Maximum ΔH_{mix} Deviation (kJ/mol)	Maximum ΔS_{mix} Deviation (kJ/mol)	Enthalpy Deviation (kJ/mol)	Entropy Deviation (kJ/mol)
Ni	+1.0142	+1.5919	-4 to +2	± 4
Co	+2.4586	+2.8310		
Fe	+1.8464	+2.0486		
Cr	+4.6478	+3.3228		

¹ Determined at $x=2$ and 1300 K for the single FCC solid solution composition range except in Cr system, where BCC+FCC is stable
² Determined for CoCrFeMnNi with a single FCC solid solution structure at 1273 K

5.2. First Principles Properties

5.2.1. Relaxed Lattice Constants

5.2.1.1. Co, Cr, Fe, Ni, and Ti Structural Relaxation

The relaxed lattice constants for each of Co, Cr, Fe, Ni, and Ti were determined from the structural relaxation carried out using DFT and are presented in Fig. 5.2.1. The calculated values are compared to experimental lattice constants obtained from Ref. [107]. The calculated values were found to be in good agreement with experiments since the discrepancy between both is less than 1% for all elements except for Fe, which exhibits a discrepancy of approximately 1.1%. For all elements, our DFT calculations underestimate the lattice constants. This contradicts the expected behavior of the PBE functional, which tends to result in a decreased cohesion and accordingly, overestimated lattice constants [108]. However, the lattice constants calculated in the present study are in good agreement with those of Janthon et al. [109], which were also calculated using the PBE functional and also underestimated the lattice constants as seen in Fig. 5.2.1.

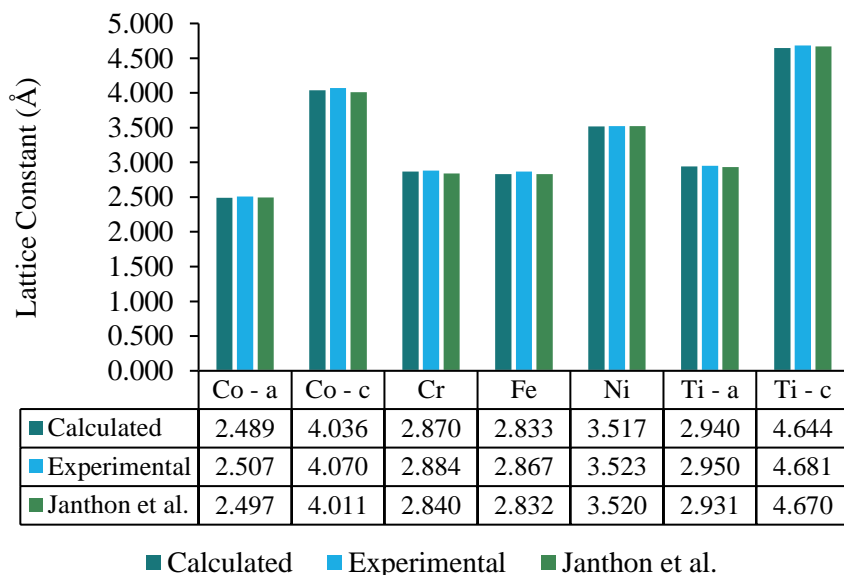


Fig. 5.2.1. Lattice constants for Co, Cr, Fe, Ni, and Ti calculated using DFT (relaxed structures); experimental values from Ref. [106]; and calculated values from Ref. [108].

5.2.1.2. Structural Relaxation of the $\text{CoCrFeNi}_{1.75}\text{Ti}_{0.25}$ SQS

As mentioned in section 4.2.1, the initial structure of the 80-atom $\text{CoCrFeNi}_{1.75}\text{Ti}_{0.25}$ SQS was a $5 \times 2 \times 2$ FCC supercell. This structure was used with an initial guess for the lattice constant of 3.6 \AA as the input for the structural relaxation. The cell parameters of the relaxed HEA SQS are provided in Table 5.2.1, which shows that the relaxation results and which correspond to an orthorhombic cell. On inspection of the atomic positions of the output structure (provided in Appendix D), an expected lattice distortion is observed, which is quantified in section 5.2.4.2.

Table 5.2.1. final cell parameters (in Å) of the relaxed CoCrFeNi_{1.75}Ti_{0.25} 80-atom SQS

	5x2x2 SQS cell	Alloy Unit Cell
a (Å)	17.968	3.594
b (Å)	7.153	3.576
c (Å)	7.077	3.539

5.2.2. Computational Stress-Strain, Young's Modulus, and Poisson's Ratio

The computational stress-strain curves of Co, Cr, Fe, Ni, and Ti under uniaxial tension in the <001> direction are shown in Fig. 5.2.2. From these diagrams, the Young's modulus and Poisson's ratio of the elements were determined and details of their calculation are provided in Appendix D. The calculated Young's modulus and Poisson's ratio for each element are summarized in Table 5.2.2. From these plots, the ideal strengths were also determined and are shown in Fig. 5.2.3.

The calculated Young's moduli of the individual elements differ significantly from experimental values for most elements and the absolute discrepancy ranges from approximately 31% for Ti to 48% for Co. The Young's modulus of Ni, however, shows good agreement with experiments (absolute discrepancy is 14%). The Poisson's ratio of Fe, Ni, and Ti show good agreement with experimental values, where the absolute discrepancy between both does not exceed 20%. For Cr, the calculated Poisson's ratio is exceptionally poor (57% absolute discrepancy) while that of Co deviates from the experimental value by approximately 38%.

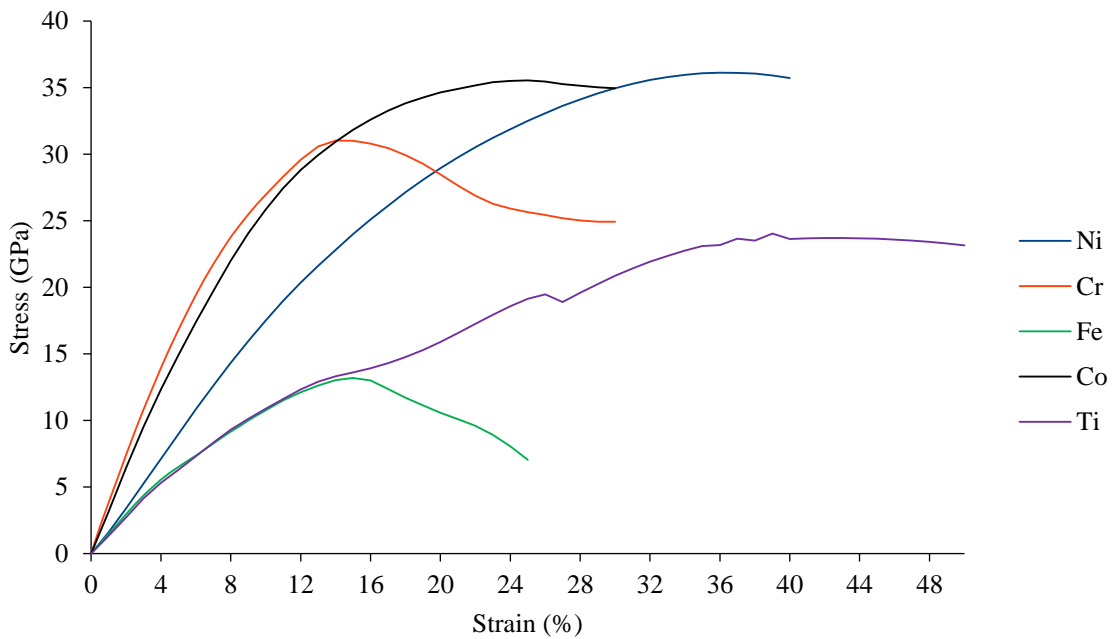


Fig. 5.2.2. Computational stress-strain curves for Co, Cr, Fe, Ni and Ti under uniaxial tension.

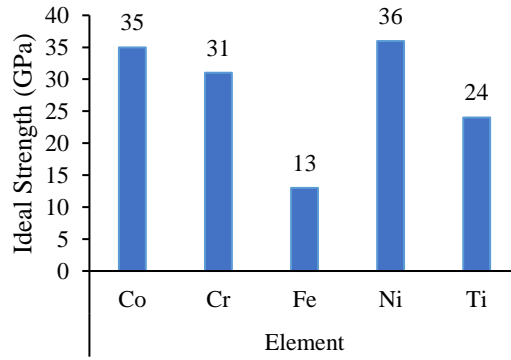


Fig. 5.2.3. Ideal strength of Co, Cr, Fe, Ni, and Ti determined from computational tensile stress-strain diagrams.

Table 5.2.2. Young's modulus, Poisson's ratio, and ideal strength as determined from computational tensile stress-strain diagrams. Experimental values and their respective references are also included for comparison.

Element	Property	DFT	Experimental	Ref.
Co	Young's Modulus (GPa)	313	211	[110]
	Poisson's Ratio	0.2	0.32	[111]
	Ideal Strength (GPa)	35	-	
Cr	Young's Modulus (GPa)	356	248	[111]
	Poisson's Ratio	0.09	0.2-0.22	[112]
	Ideal Strength (GPa)	31	-	
Fe	Young's Modulus (GPa)	146	208.2	[111]
	Poisson's Ratio	0.34	0.291	
	Ideal Strength (GPa)	13	-	
Ni	Young's Modulus (GPa)	179	207	[110]
	Poisson's Ratio	0.27	0.31	
	Ideal Strength (GPa)	36	-	
Ti	Young's Modulus (GPa)	138	100-110	[113]
	Poisson's Ratio	0.3	0.32-0.36	
	Ideal Strength (GPa)	24	-	

The same approach was also applied to the $\text{CoCrFeNi}_{1.75}\text{Ti}_{0.25}$ SQS and the resulting stress strain curve is presented in Fig. 5.2.2. Since no reports of the experimental or computational elastic properties of the $\text{CoCrFeNi}_{1.75}\text{Ti}_{0.25}$ alloy are available to date, its calculated properties will be evaluated in the present study by comparison to the weighted average by at.% of its constituent elements' properties.

The comparison of the elemental properties calculated from the stress-strain curves to their experimental counterparts suggests that this approach does not perform well in capturing the elastic

behavior of the systems considered. Accordingly, for the calculation of the selected alloy's properties, the stress-strain method will be limited to calculating its ideal tensile strength. The ideal tensile strength is an important material property as it is the stress that if exceeded locally within a material would lead to cleavage crack formation [114]. Additionally, there are no methods to-date to measure the ideal strength experimentally. For that reason, the first-principles tensile stress-strain approach followed in the present study remains essential for the quantification of this essential property and has been extensively applied for various classes of materials [115]–[118].

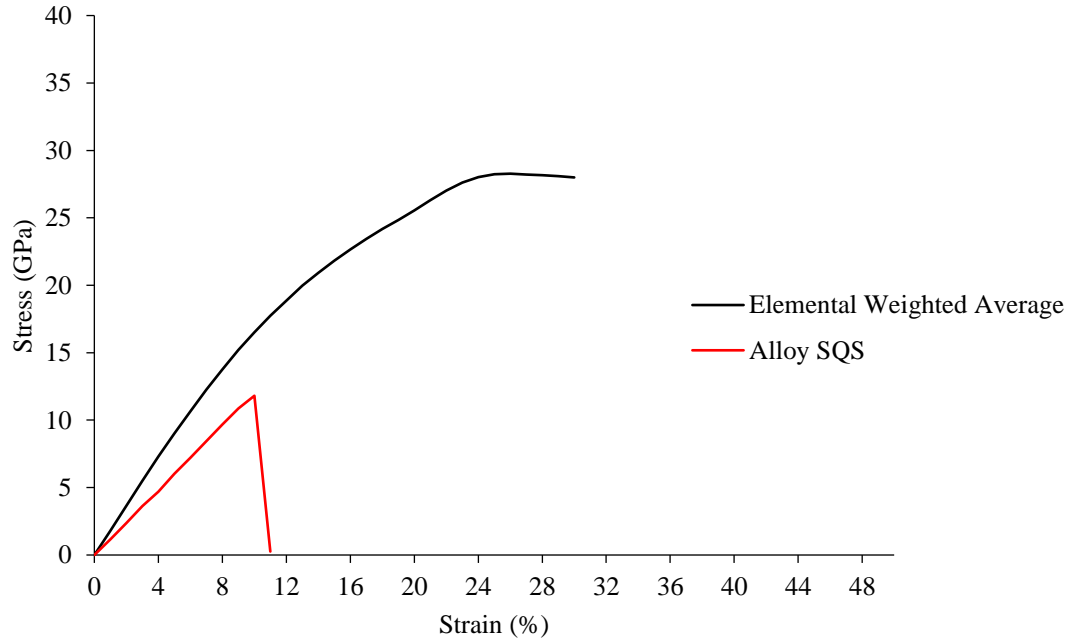


Fig. 5.2.4. Stress-strain curve of the weighted average by at.% of the $\text{CoCrFeNi}_{1.75}\text{Ti}_{0.25}$ elements (black) and that of the alloy SQS (red).

The weighted average of the DFT elemental stress-strain behavior was calculated and is used for comparison to that of the for the 80-atom $\text{CoCrFeNi}_{1.75}\text{Ti}_{0.25}$ SQS as shown in Fig. 5.2.4. As discussed in earlier chapters, the cocktail effect has been identified as one of the core effects of HEAs. To reiterate, the cocktail effect entails that the properties of an HEA are not merely a weighted average of those of its constituent element, but rather that the alloy's components work together synergistically to result in improved properties compared to the weighted average [36]. This is not the case, however, for the ideal strength determined from the computational stress-strain curve of the alloy SQS. The ideal strength of the $\text{CoCrFeNi}_{1.75}\text{Ti}_{0.25}$ alloy was found to be 11.8 GPa while the elemental weighted average was 28.24 GPa, showing an exceptionally poor performance of the alloy SQS with respect to this property. While the cocktail effect is usually considered to have positive implications on alloy properties, in the case of the present results, unfavorable atom-atom interactions in the alloy could explain the worsening of the ideal strength compared to the weighted average values.

5.2.3. Elastic Constants Analysis

The ElaStic package [90] was used with QE [95] to calculate the elastic constants of the individual elements, which can then be used to calculate the bulk, shear, and Young's modulus of each element in addition to the Poisson's ratio. More details of the procedures used are provided in Appendix D. Generally, the absolute discrepancy between the elastic properties calculated through the elastic constants approach and those obtained from experiments does not exceed 22% with the exception of the shear and Young's moduli of Co, which differ significantly from the experimental values (44% and 43% respectively). The discrepancies between all the computed and experimental values are provided in Appendix D. Overall, the elastic constants approach was found to perform better than the stress-strain approach in predicting the elastic properties of the studied elements and accordingly is used for the calculation of the bulk, shear, and Young's moduli of the alloy SQS in addition to its Poisson's ratio.

The structure of the $\text{CoCrFeNi}_{1.75}\text{Ti}_{0.25}$ SQS was constrained during its relaxation such that the cell angles all remain 90° , which after relaxation resulted in an orthorhombic cell. However, when running the ElaStic setup script, the SQS cell geometry is recognized as triclinic, which has 21 independent elastic constants. The calculated SOECs of the alloy SQS are provided in Appendix D. The calculated bulk, shear, and Young's modulus as well as the Poisson's ratio of the HEA SQS are presented in Fig. 5.2.5 and their evaluation will again be through a comparison with the corresponding weighted average properties of the individual elements.

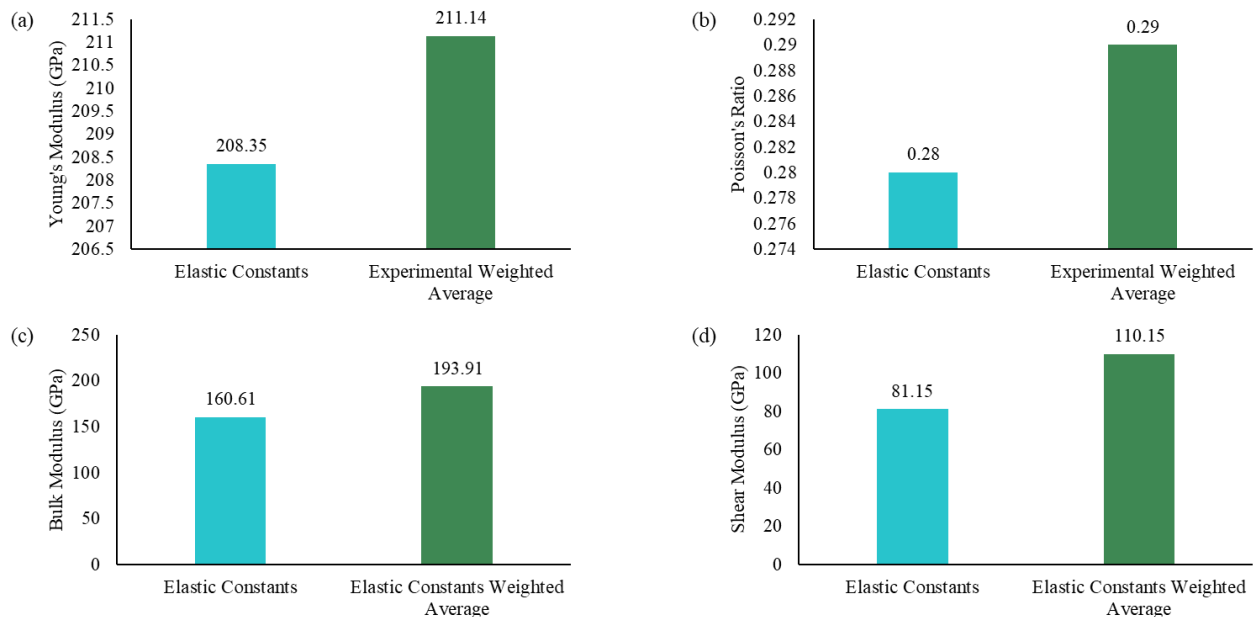


Fig. 5.2.5. Calculated elastic properties of the $\text{CoCrFeNi}_{1.75}\text{Ti}_{0.25}$ HEA SQS: (a) Young's modulus; (b) Poisson's ratio; (c) Bulk modulus; and (d) Shear modulus.

Similar to the ideal strength, the elastic properties of the alloy SQS are consistently lower than the weighted average of the calculated elemental values. This again supports the possibility of unfavorable atom-atom interactions within the alloy, which lead to the lower performance of the alloy. The properties shown in Fig. 5.2.5, however, compare much better to the weighted averages compared to the ideal strength previously shown. A summary of the CoCrFeNi_{1.75}Ti_{0.25} HEA SQS is presented in Table 5.2.3. The present results indicate that a positive cocktail effect was not achieved by the selected composition.

Table 5.2.3. CoCrFeNi_{1.75}Ti_{0.25} Young’s modulus, Poisson’s ratio, and ideal strength determined from the SQS elastic constants analysis and the ideal strength obtained from alloy stress-strain curve

Property	CoCrFeNi _{1.75} Ti _{0.25} SQS	Elemental Weighted Average
Bulk Modulus (GPa)	160.61	193.9
Shear Modulus	81.15	110.147
Young’s Modulus (GPa)	208.35	249.1
Poisson’s Ratio	0.28	0.285
Ideal Strength (GPa)	11.8	28.24

5.2.4. Other HEA Properties from the CoCrFeNi_{1.75}Ti_{0.25} SQS

5.2.4.1. Zero Kelvin Formation Enthalpy (*Enthalpy of Mixing*)

From the energy of the relaxed CoCrFeNi_{1.75}Ti_{0.25} SQS and the energies of the individual elements’ relaxed structures, the alloy formation enthalpy can be calculated. These energies are summarized in Table 5.2.5 and can be substituted into Equation 4.2.1 to calculate the formation enthalpy in Ry, which can then be converted into kJ/mol to facilitate the comparison with the mixing enthalpy calculated previously using CALPHAD.

The zero Kelvin formation enthalpy was calculated for the CoCrFeNi_{1.75}Ti_{0.25} to be 2.149 kJ/mol. On the other hand, the mixing enthalpy calculated for the same alloy at 1500 K using CALPHAD was -1.82 kJ/mol. There is a clear discrepancy between the results produced by each method. However, the lack of finite temperature effects in the zero kelvin DFT calculation can potentially account for the discrepancy. For a sound comparison, temperature dependency of the mixing enthalpy should be evaluated, and finite temperature effects added to the DFT data.

Table 5.2.5. Zero Kelvin energies of the relaxed CoCrFeNi_{1.75}Ti_{0.25} SQS and the individual elements: Co; Cr; Fe; Ni; and Ti; and the calculated zero Kelvin alloy formation enthalpies.

Structure	Concentration (no. of atoms)	Energy (Ry)	Energy/atom (Ry)	0K Formation Enthalpy (Ry)	0K Formation Enthalpy (eV/formula)	0K Formation Enthalpy (kJ/mol)
SQS	-	-21742.49	-			
Co	16	-596.98	-298.49			
Cr	16	-350.99	-175.50	0.131	0.022	2.149
Fe	16	-508.75	-254.37			
Ni	28	-1373.12	-343.28			
Ti	4	-238.50	-119.25			

5.2.4.2. Lattice Distortion

When the 80-atom CoCrFeNi_{1.75}Ti_{0.25} FCC SQS is relaxed, the atom positions change such that the atoms no longer occupy the FCC lattice sites, but rather are shifted. It has already been shown that the structural relaxation results in an orthorhombic cell. This lattice distortion is expected for HEAs and is in fact one of their core effects [37] as discussed earlier. To quantify the lattice distortion, the average displacement of the atoms of a given element in the SQS is calculated. The final orthorhombic structure is used as the reference structure and the initial atom positions were mapped onto it such that they can be compared to the final positions. Equation 4.2.2 was used for the calculations and the results are presented in Fig. 5.2.7. The largest average displacement is observed for Ti at 0.135 Å followed by Cr at 0.09 Å.

George et al. [119] argue in a recent work that the severe lattice distortion effect associated with HEAs is highly dependent on the types of elements added to the alloy rather than the number of alloying elements as previously thought. In addition to which element is added, it is also important to consider which elements it is being added with. It is suggested that this is because of the different size effect that results from each element. These sizes effects will displace atoms from the ideal lattice sites of a given structure, which results in lattice distortion. In our present results, a correlation is observed between the atomic radii of the elements (representing element size) and their average displacement from the ideal sites in the pristine FCC lattice. The results show that the average displacement for the atoms of a given element are directly proportional to their size.

Moreover, for the CoCrFeNi_{1.75}Ti_{0.25} SQS in the present study, the weighted average of the atomic displacement across all elements is approximately 6.6 pm. Due to the lack of additional computational and experimental atomic displacement data for our alloy system, the only available comparison is to that of the Cantor alloy CrMnFeCoNi. The average atomic displacement in CrMnFeCoNi was calculated from first principles to be approximately 5 pm, which was found to be in good agreement with the experimental value [119]. The Cantor alloy consists predominantly of the same elements as CoCrFeNi_{1.75}Ti_{0.05} and both exhibit an average displacement of the same

order of magnitude. Such comparisons across different HEA systems should, however, be considered with caution.

Finally, while it is important to consider the displacements of atoms from their ideal lattice locations, it is not sufficient and a framework for quantifying lattice distortion in HEAs, its *severity*, and its effect on alloy properties is needed [120].

5.2.4.3. Magnetism

The final magnetic moment on each atom of the relaxed SQS was extracted from the structural relaxation output for a basic analysis of the magnetic behavior of each element in the SQS. It should be noted that in the following, only the magnitudes of the magnetic moments are taken into account while their signs are ignored. The average magnetic moment is calculated over all atoms of a given element according to Equation 4.2.4 in addition to the standard deviation. The results are presented in Fig. 5.2.7.

One interesting observation is that the Ti atoms exhibit an average magnetic moment of $0.268 \mu_B$ despite elemental Ti being nonmagnetic. In addition to that of Ni, the average magnetic moment of Ti is the lowest among all elements. On the other hand, Fe exhibits the largest average magnetic moment among the elements at approximately 2.186 bohr magneton. Co and Cr exhibit intermediate values of 1.128 and $1.355 \mu_B$, respectively. The magnetic moment of each element extracted from the relaxation output is also presented in Fig. 5.2.7, which suggest a correlation between the elemental magnetization and the element average magnetization within the alloy. However, Cr deviates from the trend of increasing magnetization within the alloy with increasing elemental magnetization.

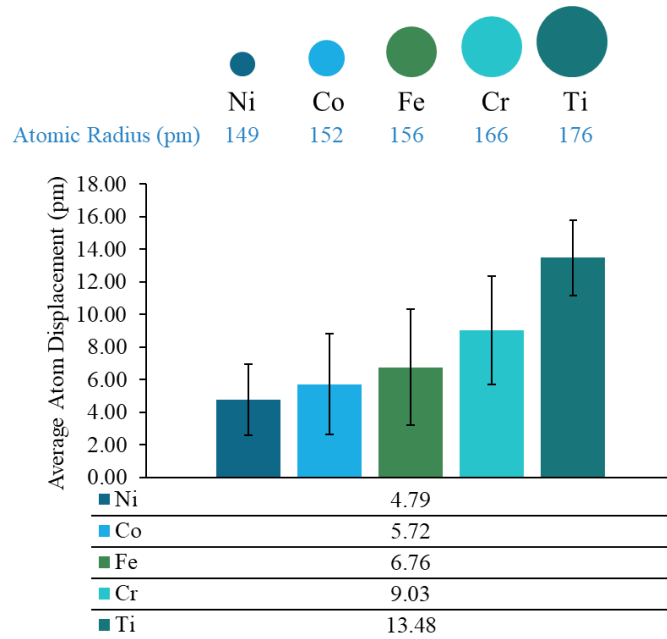


Fig. 5.2.6. Average atom displacement for each element in the $\text{CoCrFeNi}_{1.75}\text{Ti}_{0.25}$ SQS. This is a means of quantifying the lattice distortion in the relaxed SQS cell. The error bars represent standard deviation within a given element.

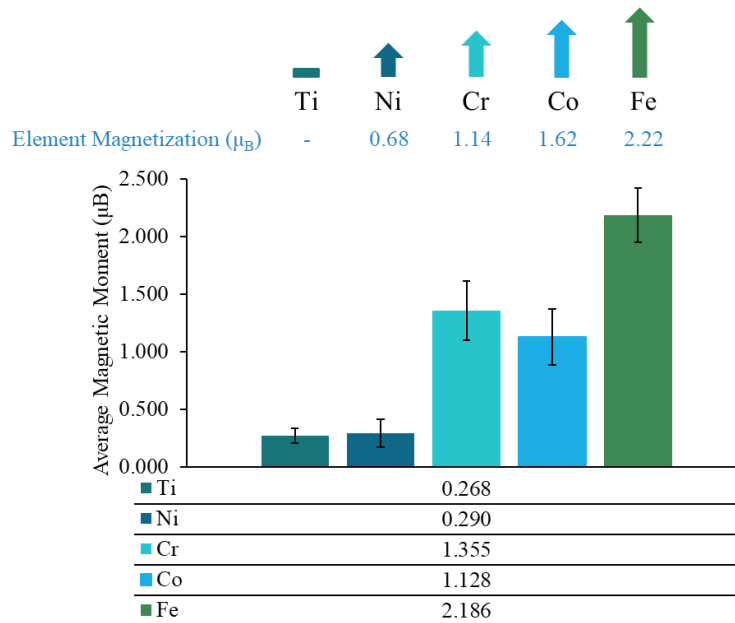


Fig. 5.2.7. The average magnetic moments for the atoms of each element in the $\text{CoCrFeNi}_{1.75}\text{Ti}_{0.25}$ SQS. The error bars indicate the standard deviation within a given element.

Chapter 6. Conclusions and Future Work

6.1. Conclusions

In this study, the CALPHAD method was used to produce phase diagrams of the $\text{CoCrFeNi}_x\text{Ti}_{2-x}$, $\text{Co}_x\text{CrFeNiTi}_{2-x}$, $\text{CoCrFe}_x\text{NiTi}_{2-x}$, and $\text{CoCr}_x\text{FeNiTi}_{2-x}$ systems. The thermodynamic properties, namely ΔH_{mix} and ΔS_{mix} , were also calculated. These were used to explain the phase stabilities of the different systems from a thermodynamic standpoint. Single solid solution phases have been the focus of many studies on HEAs due to their potential for favorable properties. However, there has been much controversy over the development of a theoretical framework for their prediction, which would aid with the design of targeted experimental studies. Accordingly, the different parts of this work were carried out with a focus on gaining further insight into the stabilization of the single FCC solid solution phase. Building on the thermodynamic study carried out, the mechanical properties of a $\text{CoCrFeNi}_{1.75}\text{Ti}_{0.25}$ single FCC solid solution alloy were characterized using first principles DFT and the SQS approach. The main findings are summarized below.

6.1.1. Computational Phase Diagrams

- (i) In their respective systems, Ni, Co, and Fe tend to be FCC phase stabilizers and their phase diagrams exhibit large regions in which a single-phase FCC structure can be stabilized given an appropriate processing method is used.
- (ii) In its system, Cr tends to be a BCC phase stabilizer and only exhibits a small single-phase FCC region.
- (iii) In addition to alloy composition, temperature plays an important role in the stabilization of the single solid solution phase, where it only forms in the high temperature regions in the phase diagrams of the systems studied.
- (iv) The intermetallic phases that form in the systems studied are the delta, η , Laves, and σ phases.
- (v) The phase diagrams and thermodynamic properties of the Ni, Co, and Fe systems indicate that these elements have similar effects on the phase stabilities of the $\text{CoCrFeNi}_x\text{Ti}_{2-x}$, $\text{Co}_x\text{CrFeNiTi}_{2-x}$, and $\text{CoCrFe}_x\text{NiTi}_{2-x}$ alloys.

6.1.2. Thermodynamic Property Calculation

- (i) Considering the overall ΔH_{mix} and ΔS_{mix} rather than those of separate phases can provide vital information regarding the phase stabilities and thermodynamic behavior of HEAs.
- (ii) Calculated ΔH_{mix} values tend to be large and negative for alloys with multi-phase structures, especially near the CoCrFeNiTi equiatomic composition. On the other hand,

they are small and either positive or negative in the concentration range where the single FCC solid solution phase is present.

- (iii) A considerable vibrational entropy contribution is expected in regions where multi-phase structures are stable as indicated by the increase in ΔS_{mix} with increasing temperature.
- (iv) For the single FCC solid solution structure, ΔS_{mix} is nearly independent of temperature, which indicates that it is mostly configurational with a minor vibrational component.
- (v) ΔH_{mix} dominates the ΔG_{mix} in composition ranges where multi-phase structures are present and decreases as the stable structure becomes simpler (eg. solid solution phase + one intermetallic phase) until it becomes smallest in the single FCC phase region, where ΔS_{mix} dominates ΔG_{mix} .
- (vi) The largest deviations of ΔH_{mix} and ΔS_{mix} from ideal solid solution behavior occur near the equiatomic composition in all systems, where multi-phase structures are present. Within the single FCC phase region, the deviation from ideal behavior is smallest.
- (vii) Multi-phase alloys exhibit the following behavior:
 - a. Large, negative ΔH_{mix} values
 - b. ΔH_{mix} dominates ΔG_{mix} rather than ΔS_{mix}
 - c. Large deviations of ΔH_{mix} and ΔS_{mix} from ideal behavior
- (viii) In contrast, single-phase alloys exhibit the following behavior:
 - a. Small, negative or positive ΔH_{mix} values
 - b. ΔS_{mix} dominates ΔG_{mix} rather than ΔH_{mix}
 - c. Small deviations of ΔH_{mix} and ΔS_{mix} from ideal behavior
- (ix) The importance of exploring non-equiatomic compositions of HEAs is emphasized as they can lead to favorable structures in addition to more opportunities for tailoring HEA properties to applications.
- (x) A significant configurational entropy contribution plays a vital role in the stabilization of single solid solution phases, however, it is only capable of doing so when the deviation of the overall thermodynamic behavior does not depart considerably from the ideal solid solution behavior. First Principles Properties

6.1.3. First Principles Alloy Properties

- (i) Based on the elemental study conducted:
 - a. The elastic constants approach for calculating mechanical properties of can better capture the elastic behavior of the studied systems (i.e. at low strain values).

- b. The stress strain approach offers a method of capturing the materials' behavior at high strain values. This approach can also be used to determine the ideal tensile strength, which is a vital material property for understanding failure behavior.
- (ii) The cocktail effect, which is a core effect of HEAs, can have both positive and negative implications, where unfavorable atom-atom interactions can lead to a deterioration of an HEA's mechanical properties.
- (iii) The importance of computationally identifying unfavorable compositions (for example, ones that exhibit a negative cocktail effect) is emphasized. Contrary to the positive notion of the cocktail effect, it is likely that not all HEAs will perform better than the weighted average behavior of their constituent elements.
- (iv) A discrepancy is observed between the enthalpy of formation calculated using DFT and its CALPHAD counterpart, the mixing enthalpy. This can be addressed by further studying the temperature dependency of the enthalpy as well as considering finite temperature effects on the DFT results, which are calculated at 0 K.
- (v) The average displacement of the atoms in the HEA SQS from their ideal FCC lattice sites is one method of quantifying the lattice distortion in the studied SQS. A correlation is observed between element size and the average displacement of atoms of a given element within the HEA SQS, where it was found that larger atoms tend to be displaced more compared to smaller ones.

6.2. Recommendations and Future Work

- (i) Validating phase diagram results by comparison to homogenized alloy structure data as more experimental studies become available.
- (ii) Considering the effect of interstitial elements such as oxygen and carbon, which can be introduced intentionally or unintentionally as the result of specific processing routes, on the phase stabilities and mechanical properties of HEAs. This is especially important when comparing computational results to experimental data for validation. Moreover, attempts to incorporate such effects into the modelling approaches used for HEAs (e.g. the SQS approach) can further improve the utilized methods' ability to more realistically capture the thermodynamic and mechanical behavior of HEAs.
- (iii) Conducting similar studies for other alloy systems of interest to:
 - a. Identify any connections between systems or global thermodynamic criteria for structure prediction.
 - b. Gain system-specific insight into the phase stabilities of important HEA systems.

- (iv) Studying additional non-equiatomic compositions for further tailoring of alloy structure and properties for various application.
- (v) Utilizing machine learning techniques to scan even larger regions of the composition space of different HEA systems to identify compositions that result in favorable structures especially.
- (vi) Carrying out further DFT calculations to determine the individual contributions of the vibrational and electronic entropies and their effect (if any) on the stabilization or destabilization of the single solid solution phase.
- (vii) Calculating vacancy formation energies and evaluating their effect on the diffusion of different elements within the random alloy (the sluggish diffusion effect).

References

- [1] J.-W. Yeh *et al.*, “Nanostructured High-Entropy Alloys with Multiple Principal Elements: Novel Alloy Design Concepts and Outcomes,” *Adv. Eng. Mater.*, vol. 6, no. 5, pp. 299–303, May 2004, doi: 10.1002/adem.200300567.
- [2] B. Cantor, I. T. H. Chang, P. Knight, and A. J. B. Vincent, “Microstructural development in equiatomic multicomponent alloys,” *Materials Science and Engineering: A*, vol. 375–377, pp. 213–218, Jul. 2004, doi: 10.1016/j.msea.2003.10.257.
- [3] J.-W. Yeh and S.-J. Lin, “Breakthrough applications of high-entropy materials,” *Journal of Materials Research*, vol. 33, no. 19, pp. 3129–3137, Oct. 2018, doi: 10.1557/jmr.2018.283.
- [4] R. Schmid-Fetzer, “Phase Diagrams: The Beginning of Wisdom,” *J. Phase Equilib. Diffus.*, vol. 35, no. 6, pp. 735–760, Dec. 2014, doi: 10.1007/s11669-014-0343-5.
- [5] C. Zhang and M. C. Gao, “CALPHAD Modeling of High-Entropy Alloys,” in *High-Entropy Alloys*, Springer, Cham, 2016, pp. 399–444.
- [6] W. Steurer, “Single-phase high-entropy alloys – A critical update,” *Materials Characterization*, vol. 162, p. 110179, Apr. 2020, doi: 10.1016/j.matchar.2020.110179.
- [7] W. H. Liu, T. Yang, and C. T. Liu, “Precipitation hardening in CoCrFeNi-based high entropy alloys,” *Materials Chemistry and Physics*, vol. 210, pp. 2–11, May 2018, doi: 10.1016/j.matchemphys.2017.07.037.
- [8] E. P. George, D. Raabe, and R. O. Ritchie, “High-entropy alloys,” *Nature Reviews Materials*, vol. 4, no. 8, Art. no. 8, Aug. 2019, doi: 10.1038/s41578-019-0121-4.
- [9] T.-T. Shun, L.-Y. Chang, and M.-H. Shiu, “Microstructures and mechanical properties of multiprincipal component CoCrFeNiTi_x alloys,” *Materials Science and Engineering: A*, vol. 556, pp. 170–174, Oct. 2012, doi: 10.1016/j.msea.2012.06.075.
- [10] Z. Fu, W. Chen, H. Xiao, L. Zhou, D. Zhu, and S. Yang, “Fabrication and properties of nanocrystalline Co_{0.5}FeNiCrTi_{0.5} high entropy alloy by MA–SPS technique,” *Materials & Design*, vol. 44, pp. 535–539, Feb. 2013, doi: 10.1016/j.matdes.2012.08.048.
- [11] L. Jiang, Y. Lu, Y. Dong, T. Wang, Z. Cao, and T. Li, “Annealing effects on the microstructure and properties of bulk high-entropy CoCrFeNiTi_{0.5} alloy casting ingot,” *Intermetallics*, vol. 44, pp. 37–43, Jan. 2014, doi: 10.1016/j.intermet.2013.08.016.
- [12] I. Moravcik *et al.*, “Microstructure and mechanical properties of Ni_{1.5}Co_{1.5}CrFeTi_{0.5} high entropy alloy fabricated by mechanical alloying and spark plasma sintering,” *Materials & Design*, vol. 119, pp. 141–150, Apr. 2017, doi: 10.1016/j.matdes.2017.01.036.
- [13] T.-T. Shun, C.-Y. Hsieh, W.-J. Hung, and C.-F. Lee, “Age Heat Treatment of the CoCrFeNiTi_{0.3} High-Entropy Alloy,” *Materials Transactions*, vol. advpub, 2018, doi: 10.2320/matertrans.M2017418.
- [14] B. Han *et al.*, “Composition evolution of gamma prime nanoparticles in the Ti-doped CoFeCrNi high entropy alloy,” *Scripta Materialia*, vol. 148, pp. 42–46, Apr. 2018, doi: 10.1016/j.scriptamat.2018.01.025.
- [15] I. Moravcik *et al.*, “Synergic strengthening by oxide and coherent precipitate dispersions in high-entropy alloy prepared by powder metallurgy,” *Scripta Materialia*, vol. 157, pp. 24–29, Dec. 2018, doi: 10.1016/j.scriptamat.2018.07.034.
- [16] R. K. Mishra and R. R. Shahi, “Novel Co₃₅Cr₅Fe₂₀Ni₂₀Ti₂₀ high entropy alloy for high magnetization and low coercivity,” *Journal of Magnetism and Magnetic Materials*, vol. 484, pp. 83–87, Aug. 2019, doi: 10.1016/j.jmmm.2019.03.129.

- [17] T.-T. Shun, C.-H. Hung, and C.-F. Lee, “Formation of ordered/disordered nanoparticles in FCC high entropy alloys,” *Journal of Alloys and Compounds*, vol. 493, no. 1, pp. 105–109, Mar. 2010, doi: 10.1016/j.jallcom.2009.12.071.
- [18] W. D. Callister and D. G. Rethwisch, *Materials science and engineering: SI version*, 8. ed., SI version. Hoboken, NJ: Wiley, 2011.
- [19] F. Zhang, “Editorial,” *J. Phase Equilib. Diffus.*, vol. 30, no. 3, pp. 219–219, Jun. 2009, doi: 10.1007/s11669-009-9529-7.
- [20] W. F. Smith, *Principles of materials science and engineering*, 3. ed. New York: McGraw Hill, 1996.
- [21] “What Are Metal Alloys? | MATSE 81: Materials In Today’s World.” <https://www.e-education.psu.edu/matse81/node/2141> (accessed May 08, 2020).
- [22] F. C. Campbell, *Phase Diagrams: Understanding the Basics*. Materials Park, UNITED STATES: ASM International, 2012.
- [23] N. Saunders and A. P. Miodownik, *CALPHAD (Calculation of Phase Diagrams): a Comprehensive Guide*. Burlington: Elsevier, 1998.
- [24] S. Furukawa and T. Komatsu, “Intermetallic Compounds: Promising Inorganic Materials for Well-Structured and Electronically Modified Reaction Environments for Efficient Catalysis,” *ACS Catal.*, vol. 7, no. 1, pp. 735–765, Jan. 2017, doi: 10.1021/acscatal.6b02603.
- [25] B. Geddes, H. Leon, and X. Huang, *Superalloys: Alloying and Performance*. Materials Park, UNITED STATES: ASM International, 2010.
- [26] “DoITPoMS - TLP Library Phase diagrams and solidification - Basic terms.” <https://www.doitpoms.ac.uk/tlplib/phase-diagrams/basic.php> (accessed May 08, 2020).
- [27] Y. A. Chang and W. A. Oates, *Materials Thermodynamics*. John Wiley & Sons, 2010.
- [28] “Gibbs Free Energy.” <https://chemed.chem.purdue.edu/genchem/topicreview/bp/ch21/gibbs.php#relation> (accessed May 08, 2020).
- [29] D. B. Miracle and O. N. Senkov, “A critical review of high entropy alloys and related concepts,” *Acta Materialia*, vol. 122, pp. 448–511, Jan. 2017, doi: 10.1016/j.actamat.2016.08.081.
- [30] C. Zhang, F. Zhang, S. Chen, and W. Cao, “Computational Thermodynamics Aided High-Entropy Alloy Design,” *JOM*, vol. 64, no. 7, pp. 839–845, Jul. 2012, doi: 10.1007/s11837-012-0365-6.
- [31] M. Widom, “Modeling the structure and thermodynamics of high-entropy alloys,” *Journal of Materials Research*, vol. 33, no. 19, pp. 2881–2898, Oct. 2018, doi: 10.1557/jmr.2018.222.
- [32] R. A. Swalin, *Thermodynamics of Solids*. Wiley, 1962.
- [33] R.-Z. Zhang and M. J. Reece, “Review of high entropy ceramics: design, synthesis, structure and properties,” *Journal of Materials Chemistry A*, vol. 7, no. 39, pp. 22148–22162, 2019, doi: 10.1039/C9TA05698J.
- [34] C. Oses, C. Toher, and S. Curtarolo, “High-entropy ceramics,” *Nature Reviews Materials*, vol. 5, no. 4, Art. no. 4, Apr. 2020, doi: 10.1038/s41578-019-0170-8.
- [35] S. Riva, A. Tudball, S. Mehraban, N. P. Lavery, S. G. R. Brown, and K. V. Yuseenko, “A novel High-Entropy Alloy-based composite material,” *Journal of Alloys and Compounds*, vol. 730, pp. 544–551, Jan. 2018, doi: 10.1016/j.jallcom.2017.09.274.
- [36] M. C. Gao, J.-W. Yeh, P. K. Liaw, and Y. Zhang, *High-Entropy Alloys Fundamentals and Applications*. Cham: Springer International Publishing, 2016.

- [37] J. W. Yeh, “Recent progress in high-entropy alloys,” *Annales de Chimie. Science des Matériaux (Paris)*, vol. 31, no. no.6, pp. 633–648, 2006.
- [38] B. S. Murty, J.-W. Yeh, and S. Ranganathan, *High-entropy alloys*. Amsterdam Boston Heidelberg: BH, Butterworth-Heinemann, an imprint of Elsevier, 2014.
- [39] B. S. Murty, J.-W. Yeh, S. Ranganathan, and P. P. Bhattacharjee, *High-Entropy Alloys*. Elsevier, 2019.
- [40] A. Manzoor, S. Pandey, D. Chakraborty, S. R. Phillpot, and D. S. Aidhy, “Entropy contributions to phase stability in binary random solid solutions,” *npj Computational Materials*, vol. 4, no. 1, Art. no. 1, Aug. 2018, doi: 10.1038/s41524-018-0102-y.
- [41] Y. Zhang and Y. J. Zhou, “Solid Solution Formation Criteria for High Entropy Alloys,” *Materials Science Forum*, 2007. <http://www.scientific.net/MSF.561-565.1337> (accessed Dec. 03, 2019).
- [42] Y. Zhang, Y. J. Zhou, J. P. Lin, G. L. Chen, and P. K. Liaw, “Solid-Solution Phase Formation Rules for Multi-component Alloys,” *Advanced Engineering Materials*, vol. 10, no. 6, pp. 534–538, doi: 10.1002/adem.200700240.
- [43] S. Guo and C. T. Liu, “Phase stability in high entropy alloys: Formation of solid-solution phase or amorphous phase,” *Progress in Natural Science: Materials International*, vol. 21, no. 6, pp. 433–446, Dec. 2011, doi: 10.1016/S1002-0071(12)60080-X.
- [44] F. Otto, Y. Yang, H. Bei, and E. P. George, “Relative effects of enthalpy and entropy on the phase stability of equiatomic high-entropy alloys,” *Acta Materialia*, vol. 61, no. 7, pp. 2628–2638, Apr. 2013, doi: 10.1016/j.actamat.2013.01.042.
- [45] A. Takeuchi and A. Inoue, “Quantitative evaluation of critical cooling rate for metallic glasses,” *Materials Science and Engineering: A*, vol. 304–306, pp. 446–451, May 2001, doi: 10.1016/S0921-5093(00)01446-5.
- [46] S. Fang, X. Xiao, L. Xia, W. Li, and Y. Dong, “Relationship between the widths of supercooled liquid regions and bond parameters of Mg-based bulk metallic glasses,” *Journal of Non-Crystalline Solids*, vol. 321, no. 1, pp. 120–125, Jun. 2003, doi: 10.1016/S0022-3093(03)00155-8.
- [47] S. Guo, C. Ng, J. Lu, and C. T. Liu, “Effect of valence electron concentration on stability of fcc or bcc phase in high entropy alloys,” *Journal of Applied Physics*, vol. 109, no. 10, p. 103505, May 2011, doi: 10.1063/1.3587228.
- [48] Y. Dong, Y. Lu, L. Jiang, T. Wang, and T. Li, “Effects of electro-negativity on the stability of topologically close-packed phase in high entropy alloys,” *Intermetallics*, vol. 52, pp. 105–109, Sep. 2014, doi: 10.1016/j.intermet.2014.04.001.
- [49] X. Yang and Y. Zhang, “Prediction of high-entropy stabilized solid-solution in multi-component alloys,” *Materials Chemistry and Physics*, vol. 132, no. 2, pp. 233–238, Feb. 2012, doi: 10.1016/j.matchemphys.2011.11.021.
- [50] O. N. Senkov and D. B. Miracle, “A new thermodynamic parameter to predict formation of solid solution or intermetallic phases in high entropy alloys,” *Journal of Alloys and Compounds*, vol. 658, pp. 603–607, Feb. 2016, doi: 10.1016/j.jallcom.2015.10.279.
- [51] M. C. Tropicovsky, J. R. Morris, P. R. C. Kent, A. R. Lupini, and G. M. Stocks, “Criteria for Predicting the Formation of Single-Phase High-Entropy Alloys,” *Phys. Rev. X*, vol. 5, no. 1, p. 011041, Mar. 2015, doi: 10.1103/PhysRevX.5.011041.
- [52] Z. Wang, S. Guo, and C. T. Liu, “Phase Selection in High-Entropy Alloys: From Nonequilibrium to Equilibrium,” *JOM*, vol. 66, no. 10, pp. 1966–1972, Oct. 2014, doi: 10.1007/s11837-014-0953-8.

- [53] J.-O. Andersson, T. Helander, L. Höglund, P. Shi, and B. Sundman, “Thermo-Calc & DICTRA, computational tools for materials science,” *Calphad*, vol. 26, no. 2, pp. 273–312, Jun. 2002, doi: 10.1016/S0364-5916(02)00037-8.
- [54] S.-L. Chen *et al.*, “Calculating phase diagrams using PANDAT and panengine,” *JOM*, vol. 55, no. 12, pp. 48–51, Dec. 2003, doi: 10.1007/s11837-003-0010-5.
- [55] B. Sundman, U. R. Kattner, M. Palumbo, and S. G. Fries, “OpenCalphad - a free thermodynamic software,” *Integrating Materials*, vol. 4, no. 1, p. 1, Jan. 2015, doi: 10.1186/s40192-014-0029-1.
- [56] B. Sundman *et al.*, “The OpenCalphad thermodynamic software interface,” *Comput Mater Sci*, vol. 125, pp. 188–196, Dec. 2016, doi: 10.1016/j.commatsci.2016.08.045.
- [57] “10 Reasons Open Source Is Good for Business | PCWorld.” https://www.pcworld.com/article/209891/10_reasons_open_source_is_good_for_business.html (accessed Jan. 09, 2020).
- [58] B. Sundman, X.-G. Lu, and H. Ohtani, “The implementation of an algorithm to calculate thermodynamic equilibria for multi-component systems with non-ideal phases in a free software,” *Computational Materials Science*, vol. 101, pp. 127–137, Apr. 2015, doi: 10.1016/j.commatsci.2015.01.029.
- [59] K. C. Hari Kumar and P. Wollants, “Some guidelines for thermodynamic optimisation of phase diagrams,” *Journal of Alloys and Compounds*, vol. 320, no. 2, pp. 189–198, May 2001, doi: 10.1016/S0925-8388(00)01491-2.
- [60] “Matcalc - Solid State and Kinetics Precipitation.” <https://www.matcalc.at/index.php/databases/open-databases> (accessed Jan. 09, 2020).
- [61] H. Mao, H.-L. Chen, and Q. Chen, “TCHEA1: A Thermodynamic Database Not Limited for ‘High Entropy’ Alloys,” *J. Phase Equilib. Diffus.*, vol. 38, no. 4, pp. 353–368, Aug. 2017, doi: 10.1007/s11669-017-0570-7.
- [62] M. Hillert, “The compound energy formalism,” *Journal of Alloys and Compounds*, vol. 320, no. 2, pp. 161–176, May 2001, doi: 10.1016/S0925-8388(00)01481-X.
- [63] M.-H. Tsai, K.-Y. Tsai, C.-W. Tsai, C. Lee, C.-C. Juan, and J.-W. Yeh, “Criterion for Sigma Phase Formation in Cr- and V-Containing High-Entropy Alloys,” *Materials Research Letters*, vol. 1, no. 4, pp. 207–212, Dec. 2013, doi: 10.1080/21663831.2013.831382.
- [64] Y. Lu, Y. Dong, L. Jiang, T. Wang, T. Li, and Y. Zhang, “A Criterion for Topological Close-Packed Phase Formation in High Entropy Alloys,” *Entropy*, vol. 17, no. 4, Art. no. 4, Apr. 2015, doi: 10.3390/e17042355.
- [65] M. Hillert, *Phase equilibria, phase diagrams and phase transformations: their thermodynamic basis*. Cambridge, UK; New York: Cambridge University Press, 2008.
- [66] C.-C. Hsieh and W. Wu, “Overview of Intermetallic Sigma (σ) Phase Precipitation in Stainless Steels,” *International Scholarly Research Notices*, 2012. <https://www.hindawi.com/journals/isrn/2012/732471/> (accessed Oct. 23, 2018).
- [67] M.-H. Tsai, K.-C. Chang, J.-H. Li, R.-C. Tsai, and A.-H. Cheng, “A second criterion for sigma phase formation in high-entropy alloys,” *Materials Research Letters*, vol. 4, no. 2, pp. 90–95, Apr. 2016, doi: 10.1080/21663831.2015.1121168.
- [68] C.-C. Tung, J.-W. Yeh, T. Shun, S.-K. Chen, Y.-S. Huang, and H.-C. Chen, “On the elemental effect of AlCoCrCuFeNi high-entropy alloy system,” *Materials Letters*, vol. 61, no. 1, pp. 1–5, Jan. 2007, doi: 10.1016/j.matlet.2006.03.140.

- [69] Y. J. Zhou, Y. Zhang, Y. L. Wang, and G. L. Chen, “Solid solution alloys of AlCoCrFeNiTi_x with excellent room-temperature mechanical properties,” *Applied Physics Letters*, vol. 90, no. 18, p. 181904, Apr. 2007, doi: 10.1063/1.2734517.
- [70] M.-H. Tsai, R.-C. Tsai, T. Chang, and W.-F. Huang, “Intermetallic Phases in High-Entropy Alloys: Statistical Analysis of their Prevalence and Structural Inheritance,” *Metals*, vol. 9, no. 2, p. 247, Feb. 2019, doi: 10.3390/met9020247.
- [71] K. J. Ducki, “Analysis of the Precipitation and Growth Processes of the Intermetallic Phases in an Fe-Ni Superalloy,” *Superalloys*, Nov. 2015, doi: 10.5772/61159.
- [72] A. S. Wilson, “Formation and effect of topologically close-packed phases in nickel-base superalloys,” *Energy Materials*, vol. 11, no. 4, pp. 1108–1118, Dec. 2016, doi: 10.1080/02670836.2016.1187335.
- [73] H. Sugimura, Y. Kaneno, and T. Takasugi, “Alloying Behavior of Ni₃M-Type Compounds with D0_a Structure,” *Materials Transactions*, vol. advpub, pp. 1102281316–1102281316, 2011, doi: 10.2320/matertrans.M2010386.
- [74] “Crystal Lattice Structures: Index by Strukturbericht Designation.” <https://homepage.univie.ac.at/michael.leitner/lattice/struk/index.html> (accessed Feb. 26, 2020).
- [75] W.-J. Hung, T.-T. Shun, and C.-J. Chiang, “Effects of reducing Co content on microstructure and mechanical properties of Co_xCrFeNiTi_{0.3} high-entropy alloys,” *Materials Chemistry and Physics*, vol. 210, pp. 170–175, May 2018, doi: 10.1016/j.matchemphys.2017.07.024.
- [76] T.-T. Shun and C.-H. Chang, “The effects of substitution of Co with Ni on microstructure, mechanical properties, and age hardening of Co_{1-x}CrFeNi_{1+x}Ti_{0.3} high-entropy alloys,” *Materials Science and Engineering: A*, vol. 763, p. 138181, Aug. 2019, doi: 10.1016/j.msea.2019.138181.
- [77] Y.-J. Chang and A.-C. Yeh, “The evolution of microstructures and high temperature properties of Al_xCo_{1.5}CrFeNi_{1.5}Ti_y high entropy alloys,” *Journal of Alloys and Compounds*, vol. 653, pp. 379–385, Dec. 2015, doi: 10.1016/j.jallcom.2015.09.042.
- [78] “Thermodynamic Databases - Thermo-Calc Software.” <https://www.thermocalc.com/products-services/databases/thermodynamic/> (accessed Mar. 05, 2020).
- [79] F. He *et al.*, “Kinetic ways of tailoring phases in high entropy alloys,” *Scientific Reports*, vol. 6, p. 34628, Sep. 2016, doi: 10.1038/srep34628.
- [80] “Sente Software - JMatPro®.” <https://www.sentesoftware.co.uk/jmatpro> (accessed Mar. 05, 2020).
- [81] A. Zunger, S.-H. Wei, L. G. Ferreira, and J. E. Bernard, “Special quasirandom structures,” *Phys. Rev. Lett.*, vol. 65, no. 3, pp. 353–356, Jul. 1990, doi: 10.1103/PhysRevLett.65.353.
- [82] S. Sharma, Ed., “Chapter 2 - Overview of BIOVIA Materials Studio, LAMMPS, and GROMACS,” in *Molecular Dynamics Simulation of Nanocomposites Using BIOVIA Materials Studio, Lammmps and Gromacs*, Elsevier, 2019, pp. 39–100.
- [83] M. C. Gao, C. Niu, C. Jiang, and D. L. Irving, “Applications of Special Quasi-random Structures to High-Entropy Alloys,” in *High-Entropy Alloys: Fundamentals and Applications*, M. C. Gao, J.-W. Yeh, P. K. Liaw, and Y. Zhang, Eds. Cham: Springer International Publishing, 2016, pp. 333–368.
- [84] A. van de Walle, M. Asta, and G. Ceder, “The Alloy Theoretic Automated Toolkit: A User Guide,” *Calphad*, vol. 26, no. 4, pp. 539–553, Dec. 2002, doi: 10.1016/S0364-5916(02)80006-2.

- [85] A. van de Walle *et al.*, “Efficient stochastic generation of special quasirandom structures,” *Calphad*, vol. 42, pp. 13–18, Sep. 2013, doi: 10.1016/j.calphad.2013.06.006.
- [86] Y. Wang *et al.*, “Computation of entropies and phase equilibria in refractory V-Nb-Mo-Ta-W high-entropy alloys,” *Acta Materialia*, vol. 143, pp. 88–101, Jan. 2018, doi: 10.1016/j.actamat.2017.10.017.
- [87] A. J. Zaddach, C. Niu, C. C. Koch, and D. L. Irving, “Mechanical Properties and Stacking Fault Energies of NiFeCrCoMn High-Entropy Alloy,” *JOM*, vol. 65, no. 12, pp. 1780–1789, Dec. 2013, doi: 10.1007/s11837-013-0771-4.
- [88] C. Niu, A. J. Zaddach, C. C. Koch, and D. L. Irving, “First principles exploration of near-equiatomic NiFeCrCo high entropy alloys,” *Journal of Alloys and Compounds*, vol. 672, pp. 510–520, Jul. 2016, doi: 10.1016/j.jallcom.2016.02.108.
- [89] N. Bao, J. Zuo, Z. Du, M. Yang, G. Jiang, and L. Zhang, “Computational characterization of the structural and mechanical properties of Al_xCoCrFeNiTi_{1-x} high entropy alloys,” *Mater. Res. Express*, vol. 6, no. 9, p. 096519, Jul. 2019, doi: 10.1088/2053-1591/ab2b77.
- [90] R. Golesorkhtabar, P. Pavone, J. Spitaler, P. Puschnig, and C. Draxl, “ElaStic: A tool for calculating second-order elastic constants from first principles,” *Computer Physics Communications*, vol. 184, no. 8, pp. 1861–1873, Aug. 2013, doi: 10.1016/j.cpc.2013.03.010.
- [91] R. Hill, “The Elastic Behaviour of a Crystalline Aggregate,” *Proc. Phys. Soc. A*, vol. 65, no. 5, pp. 349–354, May 1952, doi: 10.1088/0370-1298/65/5/307.
- [92] “Matcalc - Solid State and Kinetics Precipitation.” <https://www.matcalc.at/> (accessed May 06, 2020).
- [93] “Draw Freely | Inkscape.” <https://inkscape.org/> (accessed May 05, 2020).
- [94] T. Allison, “JANAF Thermochemical Tables, NIST Standard Reference Database 13.” National Institute of Standards and Technology, 1996, doi: 10.18434/T42S31.
- [95] P. Giannozzi *et al.*, “Quantum ESPRESSO toward the exascale,” *J. Chem. Phys.*, vol. 152, no. 15, p. 154105, Apr. 2020, doi: 10.1063/5.0005082.
- [96] K. Momma and F. Izumi, “VESTA: a three-dimensional visualization system for electronic and structural analysis,” *J Appl Cryst*, vol. 41, no. 3, pp. 653–658, Jun. 2008, doi: 10.1107/S0021889808012016.
- [97] J. P. Perdew, K. Burke, and M. Ernzerhof, “Generalized Gradient Approximation Made Simple,” *Phys. Rev. Lett.*, vol. 77, no. 18, pp. 3865–3868, Oct. 1996, doi: 10.1103/PhysRevLett.77.3865.
- [98] D. Vanderbilt, “Soft self-consistent pseudopotentials in a generalized eigenvalue formalism,” *Phys. Rev. B*, vol. 41, no. 11, pp. 7892–7895, Apr. 1990, doi: 10.1103/PhysRevB.41.7892.
- [99] G. Prandini, A. Marrazzo, I. E. Castelli, N. Mounet, and N. Marzari, “Precision and efficiency in solid-state pseudopotential calculations,” *npj Computational Materials*, vol. 4, no. 1, Art. no. 1, Dec. 2018, doi: 10.1038/s41524-018-0127-2.
- [100] “Welcome to pslibrary,” *Welcome to pslibrary*. <https://dalcorso.github.io/pslibrary/> (accessed Aug. 05, 2020).
- [101] C. Zhang *et al.*, “Understanding phase stability of Al-Co-Cr-Fe-Ni high entropy alloys,” *Materials & Design*, vol. 109, pp. 425–433, Nov. 2016, doi: 10.1016/j.matdes.2016.07.073.
- [102] M. Vaidya, G. M. Muralikrishna, and B. S. Murty, “High-entropy alloys by mechanical alloying: A review,” *Journal of Materials Research*, vol. 34, no. 5, pp. 664–686, Mar. 2019, doi: 10.1557/jmr.2019.37.

- [103] F. Zhang, C. Zhang, S. L. Chen, J. Zhu, W. S. Cao, and U. R. Kattner, “An understanding of high entropy alloys from phase diagram calculations,” *Calphad*, vol. 45, pp. 1–10, Jun. 2014, doi: 10.1016/j.calphad.2013.10.006.
- [104] M. C. Gao *et al.*, “Thermodynamics of concentrated solid solution alloys,” *Current Opinion in Solid State and Materials Science*, vol. 21, no. 5, pp. 238–251, Oct. 2017, doi: 10.1016/j.cossms.2017.08.001.
- [105] H.-W. Luan *et al.*, “Phase stabilities of high entropy alloys,” *Scripta Materialia*, vol. 179, pp. 40–44, Apr. 2020, doi: 10.1016/j.scriptamat.2019.12.041.
- [106] A. Sarkar *et al.*, “High-Entropy Oxides: Fundamental Aspects and Electrochemical Properties,” *Advanced Materials*, vol. 31, no. 26, p. 1806236, 2019, doi: 10.1002/adma.201806236.
- [107] P. Villars and J. L. C. Daams, “Atomic-environment classification of the chemical elements,” *Journal of Alloys and Compounds*, vol. 197, no. 2, pp. 177–196, Jun. 1993, doi: 10.1016/0925-8388(93)90041-K.
- [108] K. Lejaeghere, V. V. Speybroeck, G. V. Oost, and S. Cottenier, “Error Estimates for Solid-State Density-Functional Theory Predictions: An Overview by Means of the Ground-State Elemental Crystals,” *Critical Reviews in Solid State and Materials Sciences*, vol. 39, no. 1, pp. 1–24, Jan. 2014, doi: 10.1080/10408436.2013.772503.
- [109] P. Janthon *et al.*, “Bulk Properties of Transition Metals: A Challenge for the Design of Universal Density Functionals,” *J. Chem. Theory Comput.*, vol. 10, no. 9, pp. 3832–3839, Sep. 2014, doi: 10.1021/ct500532v.
- [110] J. R. Davis, *Nickel, Cobalt, and Their Alloys*. ASM International, 2000.
- [111] A. I. H. Committee, *ASM Handbook, Volume 02 - Properties and Selection: Nonferrous Alloys and Special-Purpose Materials*. ASM International.
- [112] “Properties: An Introduction to Chromium,” *AZoM.com*. <https://www.azom.com/properties.aspx?ArticleID=594> (accessed Aug. 16, 2020).
- [113] G. Welsch, R. Boyer, and E. W. Collings, *Materials Properties Handbook: Titanium Alloys*. ASM International, 1993.
- [114] N. Nagasako, M. Jahnátek, R. Asahi, and J. Hafner, “Anomalies in the response of V, Nb, and Ta to tensile and shear loading: Ab initio density functional theory calculations,” *Phys. Rev. B*, vol. 81, no. 9, p. 094108, Mar. 2010, doi: 10.1103/PhysRevB.81.094108.
- [115] D. Roundy and M. L. Cohen, “Ideal strength of diamond, Si, and Ge,” *Phys. Rev. B*, vol. 64, no. 21, p. 212103, Nov. 2001, doi: 10.1103/PhysRevB.64.212103.
- [116] F. Tian, D. Wang, J. Shen, and Y. Wang, “An ab initio investigation of ideal tensile and shear strength of TiVNbMo high-entropy alloy,” *Materials Letters*, vol. 166, pp. 271–275, Mar. 2016, doi: 10.1016/j.matlet.2015.12.064.
- [117] J.-H. Wang, Y. Lu, X.-L. Zhang, and X. Shao, “The elastic behaviors and theoretical tensile strength of γ -TiAl alloy from the first principles calculations,” *Intermetallics*, vol. 101, pp. 1–7, Oct. 2018, doi: 10.1016/j.intermet.2018.07.001.
- [118] Q. Wang, G. Du, N. Chen, C. Jiang, and L. Chen, “Ideal strengths and thermodynamic properties of W and W-Re alloys from first-principles calculation,” *Fusion Engineering and Design*, vol. 155, p. 111579, Jun. 2020, doi: 10.1016/j.fusengdes.2020.111579.
- [119] E. P. George, W. A. Curtin, and C. C. Tasan, “High entropy alloys: A focused review of mechanical properties and deformation mechanisms,” *Acta Materialia*, vol. 188, pp. 435–474, Apr. 2020, doi: 10.1016/j.actamat.2019.12.015.

[120] I. Toda-Caraballo, J. S. Wróbel, S. L. Dudarev, D. Nguyen-Manh, and P. E. J. Rivera-Díaz-del-Castillo, “Interatomic spacing distribution in multicomponent alloys,” *Acta Materialia*, vol. 97, pp. 156–169, Sep. 2015, doi: 10.1016/j.actamat.2015.07.010.

Appendix A: CALPHAD Files

All CALPHAD calculations were carried out using the OpenCalphad code version 5.0, which can be downloaded from <http://www.opencalphad.com/>. The code was compiled on a Linux Ubuntu 18.04 operating system using the makefiles available in the downloaded package in addition to extended and thorough documentation. We would also like to thank Prof. Bo Sundman for his support in getting started with OpenCalphad.

In the following, the full input and output files for the example in section 4.1.1 are provided. The mc_ni.tdb thermodynamic database is also partially included, and the full version can be downloaded from <https://www.matcalc.at/index.php/databases/open-databases>.

OpenCalphad Input File

```
set echo
r t mcni
co cr fe ni ti
set cond t=1500 p=1e5 x(co)=0.2 x(cr)=0.2 x(fe)=0.2 x(ni)=0.35 n=1
c e
l r 1
exit y
```

OpenCalphad Output File

```
Open Calphad (OC) software version 5.004 , linked 2018-08-01
with command line monitor version 34
```

```
This program is available with a GNU General Public License.
It includes the General Thermodynamic Package, version GTP-3.21,
Hillert's equilibrium calculation algorithm version HMS-2.11,
step/map/plot software version SMP-2.21 for GNUPLOT graphics,
numerical routines extracted from LAPACK and BLAS and
the assessment procedure uses LMDIF from ANL (Argonne, USA)
```

```
Warning, no help file
--->OC5:On? /Y/: --->OC5:... echo: r t mcni
Database has 22 elements: AL B C CO CR CU FE HF LA MN MO N NB NI O S SI TI
V W Y ZR
Give the elements to select, finish with empty line
Select elements /all/:... echo: co cr fe ni ti
Select elements /no more/:Selected 5 elements: CO CR FE NI TI
3E reading a TDB file
```

```
There are 40 bibliographic references
REF:73 '*** Not set by database or user'
REF:0 '*** Not set by database or user'
REF:64 '*** Not set by database or user'
REF:152 '*** Not set by database or user'
REF:79 '*** Not set by database or user'
REF:167 '*** Not set by database or user'
REF:22 '*** Not set by database or user'
REF:11 '*** Not set by database or user'
REF:21 '*** Not set by database or user'
REF:153 '*** Not set by database or user'
REF:SAN15 '*** Not set by database or user'
REF:POV15 '*** Not set by database or user'
REF:POV12 '*** Not set by database or user'
REF:159 '*** Not set by database or user'
REF:23 '*** Not set by database or user'
REF:176 '*** Not set by database or user'
REF:92 '*** Not set by database or user'
```

```

REF:74      '*** Not set by database or user'
REF:20      '*** Not set by database or user'
REF:12      '*** Not set by database or user'
REF:POV09   '*** Not set by database or user'
REF:POV11   '*** Not set by database or user'
REF:137     '*** Not set by database or user'
REF:217     '*** Not set by database or user'
REF:117     '*** Not set by database or user'
REF:91      '*** Not set by database or user'
REF:111     '*** Not set by database or user'
REF:POV13   '*** Not set by database or user'
REF:POV10   '*** Not set by database or user'
REF:POV14   '*** Not set by database or user'
REF:162     '*** Not set by database or user'
REF:156     '*** Not set by database or user'
REF:157     '*** Not set by database or user'
REF:SSH13   '*** Not set by database or user'
REF:16      '*** Not set by database or user'
REF:158     '*** Not set by database or user'
REF:216     '*** Not set by database or user'
REF:62      '*** Not set by database or user'
REF:13      '*** Not set by database or user'
REF:145     '*** Not set by database or user'

```

```

--->OC5:... echo: set cond t=1500 p=1e5 x(co)=0.2 x(cr)=0.2 x(fe)=0.2 x(ni)=0.35 n=1

```

```

--->OC5:--->OC5:... echo: c e

```

```

3Y Constitution of metastable phases set

```

```

3Y Composition set(s) created:

```

```

Gridmin: 12663 points 1.18E-01 s and 109 clockcycles, T= 1500.00

```

```

Phase change: its/add/remove: 5 0 2

```

```

Phase change: its/add/remove: 10 0 23

```

```

Phase change: its/add/remove: 15 0 25

```

```

Phase change: its/add/remove: 24 9 0

```

```

Phase change: its/add/remove: 29 0 24

```

```

Phase change: its/add/remove: 34 0 9

```

```

Equilibrium calculation 39 its, 1.6566E-01 s and 165 clockcycles

```

```

--->OC5:--->OC5:... echo: l r 1

```

```

Output for equilibrium: 1, DEFAULT_EQUILIBRIUM 2020.05.05

```

```

Conditions .....:

```

```

1:T=1500, 2:P=100000, 3:X(CO)=0.2, 4:X(CR)=0.2, 5:X(FE)=0.2, 6:X(NI)=0.35,

```

```

7:N=1

```

```

Degrees of freedom are 0

```

```

Some global data, reference state SER .....:

```

```

T= 1500.00 K ( 1226.85 C), P= 1.0000E+05 Pa, V= 0.0000E+00 m3

```

```

N= 1.0000E+00 moles, B= 5.6291E+01 g, RT= 1.2472E+04 J/mol

```

```

GS= -1.00721E+05 J, GS/N= -1.0072E+05 J/mol, HS= 3.9188E+04 J, S= 932.727 J/K

```

```

Some data for components .....:

```

```

Component name Moles Mole-fr Chem.pot/RT Activities Ref.state

```

```

CO 2.0000E-01 0.20000 -8.4393E+00 2.1619E-04 SER (default)

```

```

CR 2.0000E-01 0.20000 -6.4880E+00 1.5216E-03 SER (default)

```

```

FE 2.0000E-01 0.20000 -8.1347E+00 2.9318E-04 SER (default)

```

```

NI 3.5000E-01 0.35000 -8.0155E+00 3.3031E-04 SER (default)

```

```

TI 5.0000E-02 0.05000 -1.3162E+01 1.9215E-06 SER (default)

```

```

Some data for phases .....:

```

```

Name Status Moles Volume Form.Units Cmp/FU dGm/RT Comp:

```

```

FCC_A1..... E 1.000E+00 0.00E+00 1.00E+00 1.00 0.00E+00 X:

```

```

NI 3.5000E-01 FE 2.0000E-01 CR 2.0000E-01 TI 5.0000E-02

```

```

CO 2.0000E-01

```

```

--->OC5:--->OC5:... echo: exit y

```

Database: mc_ni.tdb v 2.033 [60] (Partial)

```
*****
$
$ mc_ni_v2.033.tdb
$
$*****RELEASE VERSION*****
$
$ MatCalc Ni database, mc_ni_v2.033.tdb, created 2015-08-06
$
$ This database contains a selection of published thermodynamic data
$ for Ni-base superalloys, as well as newly assessed data.
$ Thermodynamic parameters have been assessed at TU Wien
$ by Povoden-Karadeniz Erwin.
$
$#####
$ use with MatCalc version 5.62.0.010 or higher
$
$#####
$ Copyright holder and editor:
$ Erwin Povoden-Karadeniz (erwin.povoden-karadeniz@tuwien.ac.at)
$
$ This database mc_ni_v2.033.tdb is made available under the
$ Open Database License: http://opendatacommons.org/licenses/odbl/1.0/.
$ Any rights in individual contents of the database are licensed under the
$ Database Contents License: http://opendatacommons.org/licenses/dbcl/1.0/.
$
$#####

$ The following assessments are incorporated in this database:
$
$ ... see list of publications in the reference section
$ at the end of this file ...
$
$ The following elements are included in this database:
$
$ Ni, Al, B, C, Co, Cr, Cu, Fe, Hf, La, Mn, Mo, N, Nb, O, S, Si,
$ Ti, V, W, Y, Zr
$
$ This database is especially adapted to the demands of thermo-kinetic
$ precipitation simulations in Ni-base superalloys.
$ Phase equilibria containing gamma, gamma prime, sigma, G-Phase and
$ carbides MX, M6C and M23C6 are optimized in the typical composition range
$ of classical Ni-superalloys, i.e. subsystems of
$ Ni-Al-C-Co-Cr-Fe-Hf-Mo-Nb-Ti-W-Zr.
$ The database has been tested inside the following composition limits
$ (given in wt%):
$ Al<10, B<0.05, C<0.1, Co<20, Cr<20, Fe<20, Hf<2, Mo<8, Nb<6, Ti<4, W<8
$ Solid oxide phases are described with simple models
$ without charge disproportionations or oxygen and cation nonstoichiometries.
$ oxide liquid is NOT included.
$
$ The following phases are included in this database:
$ They are listed in the order of their appearance in
$ part D) Thermodynamic model parameters for phases.
$ For their documentation see part D).
$ Documentation and priority rankings suggested by the editor
$ are visible after reading the database and marking the phase of interest.
$
$ LIQUID (oxide melt not included)
$
$ FCC_A1
$ BCC_A2
$ HCP_A3

$ ALPHA_MN
$ BETA_MN
$ BETA_RHOMBO_B
$ CU_S
$ DIAMOND_A4
```

```

$ GRAPHITE

$ Ordered phases (split model used)
$ BCC_B2

$ Intermetallic phases
$ CHI_A12 CO3MO CO3V CR3MN5 DELTA
$ D_NIMO GAMMA_DP GAMMA_PRIME G_PHASE LAV_C14 LAVES MU_PHASE
$ NIAL NI2CR NI5HF NI7HF2 ETA NITI2 P_PHASE R_PHASE SIGMA
$ FE17Y2 NI5Y

$ Carbides
$ CEMENTITE CR2VC2 K_PHASE KSI_CARBIIDE M3C2 M6C
$ M7C3 M12C M23C6 V3C2 WC
$ NOTE: Composition sets of hcp-type M2C and fcc-type MC can be defined
$ by the User, see section B)

$ Nitrides
$ ALN ALN_EQU BN_HP4 FE4N MN6N4 MN6N5 ZET
$ NOTE: Composition sets of fcc-type MX nitrides can be defined by the User,
$ see section B)

$ Borides
$ CRB CR2B CR5B3 FEB FENBB FE3NB3B4 M2B
$ MOB MOB2 NBB NB3B2 NB5B6 TIB TIB2 TI3B4

$ Carbo-nitrides
$ NOTE: Composition sets of fcc-type MX carbo-nitrides can be defined
$ by the User.

$ Sulfides
$ A_CHALC ANILITE B_CHALC COVELLITE CU2S DIGENITE
$ DISULF DJURLEITE FC_MONO FC_ORTHO FES_P MNS_Q PYRR TIS

$ Carbo-sulfides
$ TI4C2S2
$

$ Oxides
$ Simple oxide models without considering of cation
$ and oxygen nonstoichiometries are used.
$ CORUND HALITE HF102_M HF102_T HF102_C LA203_A LA203_H LA203_C
$ SIO2 SPINEL TI2O3 TIO2 TRID Y2O3_H Y2O3_C
$
$*****
$
$ A) Definition of elements
$ From A. T. Dinsdale, SGTE data for pure elements (REF 0)
$
$*****
$
$Element Standard state mass [g/mol] enthalpy_298 entropy_298
ELEMENT VA VACUUM 0.0 0.00 0.00 !
ELEMENT AL FCC_A1 26.98154 4540.0 28.30 !
ELEMENT B BETA_RHOMBO_B 10.811 1222.0 5.90 !
ELEMENT C HEX_A9 12.011 1054.0 5.7423 !
ELEMENT CO HCP_A3 58.933 4765.567 30.03 !
ELEMENT CR BCC_A2 51.996 4050.0 23.5429 !
ELEMENT CU FCC_A1 63.546 5004.0 33.15 !
ELEMENT FE BCC_A2 55.847 4489.0 27.2797 !
ELEMENT HF HCP_A3 178.49 5845.0 43.56 !
ELEMENT LA DOUBLE_HCP(ABAC) 138.91 6665.1 56.902 !
ELEMENT MN BCC_A12 54.9380 4995.696 32.2206 !
ELEMENT MO BCC_A2 95.94 4589.0 28.56 !
ELEMENT N 1/2_MOLE_N2(G) 14.007 4335.0 95.751 !
ELEMENT NB BCC_A2 92.9064 5220.0 36.27 !
ELEMENT NI FCC_A1 58.69 4787.0 29.7955 !
ELEMENT O 1/2_MOLE_O2(GAS) 15.999 4341.0 102.5200 !
ELEMENT S FC_ORTHORH 32.066 4412.0 32.054 !
ELEMENT SI DIA_A4 28.0855 3217.0 18.81 !
ELEMENT TI HCP_A3 47.88 4824.0 30.72 !
ELEMENT V BCC_A2 50.9415 4507.0 30.89 !
ELEMENT W BCC_A2 183.85 4970.0 32.6176 !
ELEMENT Y HCP_A3 88.9059 5966.384 44.4341 !
ELEMENT ZR HCP_A3 91.224 5566.3 39.181 !

```

Database Benchmarking Example

For benchmarking the performance of the database used, experimental phase data can be compared to the results of single-point equilibrium CALPHAD calculations carried out for the same temperature and composition. One important consideration is the conditions under which the experimental data was produced. For example, it is very important to only consider data for equilibrium or near-equilibrium structures, which can often be difficult to reach in experiments. More homogenized structure data for samples annealed for extended periods of time are becoming available for various HEAs, and these can be used to continually validate the thermodynamic databases used in CALPHAD calculations for HEAs.

Condition¹	Reported Phase¹	CALPHAD Prediction	Notes
Annealed under Ar at 700°C for 48 hours + Air cooling	FCC + η	FCC + η + σ	Additional σ predicted
Annealed under Ar at 900°C for 48 hours + Air cooling	FCC + η	FCC + η	Match
Annealed under Ar at 1000°C for 48 hours + Air cooling	FCC	FCC + η	η phase dissolution predicted at higher temperature

*Additional oxide particles were also found as a result of the oxygen introduced unintentionally by the powder metallurgy (PM) fabrication method, and which was not part of the initial compositions considered.

¹ I. Moravcik et al., “Synergic strengthening by oxide and coherent precipitate dispersions in high-entropy alloy prepared by powder metallurgy,” *Scripta Materialia*, vol. 157, pp. 24–29, Dec. 2018, doi: 10.1016/j.scriptamat.2018.07.034.

Appendix B: Phase Diagram Construction

The scripts and codes developed for the different stages of the phase diagram construction are provided below. First, the bash script used to automate the single-point CALPHAD calculations is presented. This is followed by the C++ which was developed to process the CALPHAD output and then the python plotting tool, which generates the phase diagrams based on the processed CALPHAD output.

Script to automate CALPHAD calculations

```
for ((T=300; T <= 2000; T=T+100)); do
for C in $(seq 0 0.1 0.4); do
cat > inputT$T.C$C.OCM << EOF
set echo
r t mcni
co cr fe ni ti

set cond t=$T p=1e5 x(co)=0.2 x(cr)=0.2 x(ni)=$C x(fe)=0.2 n=1
c e
l r 1
exit y
EOF
/home/geraldine/openalphase-master/macros/oc5A < inputT$T.C$C.OCM > outputT$T.C$C
echo "T = $T and C = $C" >> grandoutput
grep BCC outputT$T.C$C >> grandoutput
grep FCC outputT$T.C$C >> grandoutput
grep ETA outputT$T.C$C >> grandoutput
grep LAV outputT$T.C$C >> grandoutput
grep SIG outputT$T.C$C >> grandoutput
grep DEL outputT$T.C$C >> grandoutput
grep GAM outputT$T.C$C >> grandoutput
grep LIQ outputT$T.C$C >> grandoutput
done
done
```

C++ Code for Output Processing

```
// This program reads the collective CALPHAD output file to determine the phase combinations at a
// given temperature and composition
// Each point is assigned a color corresponding to the combination phases present
#include <iostream>
#include <fstream>
#include <string>
using namespace std;
int main(){
// input file stream and define input file to open
ifstream infile;
infile.open("compiled_output_ni");
//check for error opening input file
if (infile.fail()){
    cerr << "Error Opening File" << endl;
    exit(1);
}
// output file stream and define output file to be created and written to
ofstream outfile;
outfile.open("ni_23_03_20.txt");
//Variable Definition
// variables for reading input file
string line;
string firstword = "start";
string temp;
string comp;
string frac;
double nTemp;
int n = 0;
int ext = 3;
// define variables assigned to each phase, variable name is phase name
// otherPhase is used to determine if an unknown phase is present
int BCC = 0;
int FCC = 0;
int ETA = 0;
int LAV = 0;
int SIG = 0;
int DEL = 0;
int GAM = 0;
int LIQ = 0;
int NIT = 0;
int dummy = 0;
int unknown = 0;
// color assigned to specified phase combination
string color;
// read the file until the word "END" is found
while (firstword != "END"){
// read the next line in the input file and store in "line" then extract first 3 characters in
the line and store in "firstword"
    getline(infile, line);
    firstword = line.substr(0,3);
    if ( firstword == "T ="){
        temp = line.substr(4,4);
        nTemp = stod(temp);
        if (nTemp < 1000){
            comp = line.substr(16,5);
        } else if (nTemp >= 1000) {
            comp = line.substr(17,5);
        }
    } else if ((firstword != "T =") && (firstword != "END") && (firstword != " 3Y")){
        frac = line.substr(35,2);
        n = stoi(frac);
    }
    outfile << nTemp << "," << comp << ",";
// this loop makes sure that all phases are read
// the "|| ((BCC == 0) && (ETA == 0) && (otherPhase == 0)) ..." condition ensures the first
iteration is successful
// the "&& (firstword != "END")" condition ensures the last iteration is successful and helps end
the program
        while ( ((firstword != "T =") || ((BCC == 0) && (FCC ==0) && (ETA == 0) && (LAV
== 0) && (SIG == 0) && (DEL == 0) && (GAM == 0) && (LIQ == 0) && (NIT == 0))) && (firstword !=
"END") ) {
            if (firstword == "T =") {
```

```

        BCC = 0;
        FCC = 0;
        ETA = 0;
        LAV = 0;
        SIG = 0;
        DEL = 0;
        GAM = 0;
        LIQ = 0;
        NIT = 0;
        unknown = 0;
    } else if ((firstword == "BCC") && (n < ext)) {
        BCC = 1;
    } else if ((firstword == "FCC") && (n < ext)) {
        FCC = 1;
    } else if ((firstword == "ETA") && (n < ext)) {
        ETA = 1;
    } else if ((firstword == "LAV") && (n < ext)) {
        LAV = 1;
    } else if ((firstword == "SIG") && (n < ext)) {
        SIG = 1;
    } else if ((firstword == "DEL") && (n < ext)) {
        DEL = 1;
    } else if ((firstword == "GAM") && (n < ext)) {
        GAM = 1;
    } else if ((firstword == "LIQ") && (n < ext)) {
        LIQ = 1;
    } else if (((firstword == "NIT") || (firstword == "NIA")) && (n < ext)) {
        NIT = 1;
    } else if ((firstword == " 3Y") && (n < ext)) {
        dummy = 0;
    }
    getline(infile, line);
    firstword = line.substr(0,3);
    if ( firstword == "T"){
        temp = line.substr(4,4);
        nTemp = stod(temp);
        if (nTemp < 1000){
            comp = line.substr(16,5);
        } else if (nTemp >= 1000) {
            comp = line.substr(17,5);
        }
    }
    } else if ((firstword != "T") && (firstword != "END") && (firstword != "
3Y")){
        frac = line.substr(35,2);
        n = stoi(frac);
    }
}
// test for phase combinations
if ((BCC == 1) && (ETA == 0) && (LAV == 0) && (SIG == 0) && (DEL == 0) && (FCC
== 0) && (GAM == 0) && (NIT == 0) && (LIQ == 0)){
    color = "1";
} else if ((BCC == 1) && (ETA == 0) && (LAV == 0) && (SIG == 0) && (DEL == 0)
&& (FCC == 1) && (GAM == 0) && (NIT == 0) && (LIQ == 0)){
    color = "2";
} else if ((BCC == 1) && (ETA == 0) && (LAV == 0) && (SIG == 0) && (DEL == 1)
&& (FCC == 1) && (GAM == 0) && (NIT == 0) && (LIQ == 0)){
    color = "3";
} else if ((BCC == 1) && (ETA == 1) && (LAV == 0) && (SIG == 1) && (DEL == 1)
&& (FCC == 1) && (GAM == 0) && (NIT == 0) && (LIQ == 0)){
    color = "4";
} else if ((BCC == 1) && (ETA == 0) && (LAV == 0) && (SIG == 1) && (DEL == 1)
&& (FCC == 1) && (GAM == 1) && (NIT == 0) && (LIQ == 0)){
    color = "5";
} else if ((BCC == 1) && (ETA == 0) && (LAV == 0) && (SIG == 1) && (DEL == 1)
&& (FCC == 1) && (GAM == 0) && (NIT == 0) && (LIQ == 0)){
    color = "6";
} else if ((BCC == 1) && (ETA == 1) && (LAV == 0) && (SIG == 0) && (DEL == 0)
&& (FCC == 1) && (GAM == 0) && (NIT == 0) && (LIQ == 0)){
    color = "7";
} else if ((BCC == 1) && (ETA == 1) && (LAV == 1) && (SIG == 0) && (DEL == 0)
&& (FCC == 1) && (GAM == 0) && (NIT == 0) && (LIQ == 0)){
    color = "8";
} else if ((BCC == 1) && (ETA == 1) && (LAV == 1) && (SIG == 0) && (DEL == 0)
&& (FCC == 1) && (GAM == 0) && (NIT == 0) && (LIQ == 1)){
    color = "9";
}

```



```

    } else if ((BCC == 0) && (ETA == 0) && (LAV == 1) && (SIG == 0) && (DEL == 1)
&& (FCC == 0) && (GAM == 1) && (NIT == 1) && (LIQ == 0)){
        color = "85";
    } else if ((BCC == 0) && (ETA == 1) && (LAV == 1) && (SIG == 0) && (DEL == 0)
&& (FCC == 0) && (GAM == 1) && (NIT == 1) && (LIQ == 0)){
        color = "86";
    } else if ((BCC == 0) && (ETA == 1) && (LAV == 1) && (SIG == 0) && (DEL == 0)
&& (FCC == 0) && (GAM == 1) && (NIT == 0) && (LIQ == 1)){
        color = "87";
    } else if ((BCC == 0) && (ETA == 1) && (LAV == 1) && (SIG == 0) && (DEL == 0)
&& (FCC == 0) && (GAM == 1) && (NIT == 0) && (LIQ == 0)){
        color = "88";
    } else if ((BCC == 0) && (ETA == 0) && (LAV == 0) && (SIG == 1) && (DEL == 0)
&& (FCC == 0) && (GAM == 1) && (NIT == 0) && (LIQ == 0)){
        color = "89";
    } else {
        color = "90";
    }
}
// print color corresponding to phase combination
outfile << color << endl;
// reset phase variables for new condition
BCC = 0;
ETA = 0;
LAV = 0;
SIG = 0;
DEL = 0;
FCC = 0;
GAM = 0;
LIQ = 0;
NIT = 0;
}
// close input and output file streams
infile.close();
outfile.close();
return 0;
}

```

Python Code for Plotting and Phase Diagram Generation

```
import matplotlib.pyplot as plt
import numpy as np
x, y, z=np.loadtxt('ni_cut.txt', delimiter=',', unpack=True)
new_z = []
for every_z in z:
    if (every_z == 1):
        comb = 'lightyellow'
    elif (every_z == 2):
        comb = 'mediumpurple'
    elif (every_z == 3):
        comb = 'lemonchiffon'
    elif (every_z == 4):
        comb = 'seagreen'
    elif (every_z == 5):
        comb = 'peachpuff'
    elif (every_z == 6):
        comb = 'lightcoral'
    elif (every_z == 7):
        comb = 'lightgray'
    elif (every_z == 8):
        comb = 'sandybrown'
    elif (every_z == 9):
        comb = 'darkslateblue'
    elif (every_z == 10):
        comb = 'rosybrown'
    elif (every_z == 11):
        comb = 'orchid'
    elif (every_z == 12):
        comb = 'aquamarine'
    elif (every_z == 13):
        comb = 'darkorchid'
    elif (every_z == 14):
        comb = 'darkseagreen'
    elif (every_z == 15):
        comb = 'coral'
    elif (every_z == 16):
        comb = 'plum'
    elif (every_z == 17):
        comb = 'indigo'
    elif (every_z == 18):
        comb = 'orangered'
    elif (every_z == 19):
        comb = 'darkorange'
    elif (every_z == 20):
        comb = 'thistle'
    elif (every_z == 21):
        comb = 'crimson'
    elif (every_z == 22):
        comb = 'lime'
    elif (every_z == 23):
        comb = 'cyan'
    elif (every_z == 24):
        comb = 'grey'
    elif (every_z == 25):
        comb = 'mediumspringgreen'
    elif (every_z == 26):
        comb = 'pink'
    elif (every_z == 27):
        comb = 'sienna'
    elif (every_z == 28):
        comb = 'darkmagenta'
    elif (every_z == 29):
        comb = 'yellow'
    elif (every_z == 30):
        comb = 'lightseagreen'
    elif (every_z == 31):
        comb = 'orange'
    elif (every_z == 32):
        comb = 'lightgreen'
    elif (every_z == 33):
        comb = 'tan'
    elif (every_z == 34):
```

```

        comb = 'mediumvioletred'
elif (every_z == 35):
    comb = 'hotpink'
elif (every_z == 36):
    comb = 'darkkhaki'
elif (every_z == 37):
    comb = 'mistyrose'
elif (every_z == 38):
    comb = 'wheat'
elif (every_z == 39):
    comb = 'goldenrod'
elif (every_z == 40):
    comb = 'm'
elif (every_z == 41):
    comb = 'y'
elif (every_z == 42):
    comb = 'lavender'
elif (every_z == 43):
    comb = 'darkslategrey'
elif (every_z == 44):
    comb = 'r'
elif (every_z == 45):
    comb = 'olivedrab'
elif (every_z == 46):
    comb = 'moccasin'
elif (every_z == 47):
    comb = 'lightcyan'
elif (every_z == 48):
    comb = 'yellowgreen'
elif (every_z == 49):
    comb = 'royalblue'
elif (every_z == 50):
    comb = 'bisque'
elif (every_z == 51):
    comb = 'mediumseagreen'
elif (every_z == 52):
    comb = 'g'
elif (every_z == 53):
    comb = 'slateblue'
elif (every_z == 54):
    comb = 'lawngreen'
elif (every_z == 55):
    comb = 'azure'
elif (every_z == 56):
    comb = 'peru'
elif (every_z == 57):
    comb = 'burlywood'
elif (every_z == 58):
    comb = 'palevioletred'
elif (every_z == 59):
    comb = 'indianred'
elif (every_z == 60):
    comb = 'beige'
elif (every_z == 61):
    comb = 'navy'
elif (every_z == 62):
    comb = 'deepskyblue'
elif (every_z == 63):
    comb = 'palegreen'
elif (every_z == 64):
    comb = 'c'
elif (every_z == 65):
    comb = 'lightskyblue'
elif (every_z == 66):
    comb = 'lightsteelblue'
elif (every_z == 67):
    comb = 'olive'
elif (every_z == 68):
    comb = 'firebrick'
elif (every_z == 69):
    comb = 'steelblue'
elif (every_z == 70):
    comb = 'teal'
elif (every_z == 71):
    comb = 'maroon'

```

```

elif (every_z == 72):
    comb = 'powderblue'
elif (every_z == 73):
    comb = 'khaki'
elif (every_z == 74):
    comb = 'b'
elif (every_z == 75):
    comb = 'paleturquoise'
elif (every_z == 76):
    comb = 'palegoldenrod'

elif (every_z == 77):
    comb = 'darkolivegreen'
elif (every_z == 78):
    comb = 'darkred'
elif (every_z == 79):
    comb = 'midnightblue'
elif (every_z == 80):
    comb = 'dodgerblue'
elif (every_z == 81):
    comb = 'darkcyan'
elif (every_z == 82):
    comb = 'darkviolet'
elif (every_z == 83):
    comb = 'darkgoldenrod'
elif (every_z == 84):
    comb = 'violet'
elif (every_z == 85):
    comb = 'springgreen'
elif (every_z == 86):
    comb = 'darkgreen'
elif (every_z == 87):
    comb = 'chocolate'
elif (every_z == 88):
    comb = 'aliceblue'
elif (every_z == 89):
    comb = 'darksalmon'
elif (every_z == 90):
    comb = 'k'
new_z.append(comb)
plt.scatter(y,x, c=new_z, s=17, edgecolor='none')
plt.xticks(np.arange(0.2, 0.45, 0.01))
plt.yticks(np.arange(300, 2100, 100))
plt.xlabel('Ni fraction (x)')
plt.ylabel('Temperature (K)')
plt.title('CoCrFeNi(x)Ti(2-x) Phase Diagram')
plt.show

```

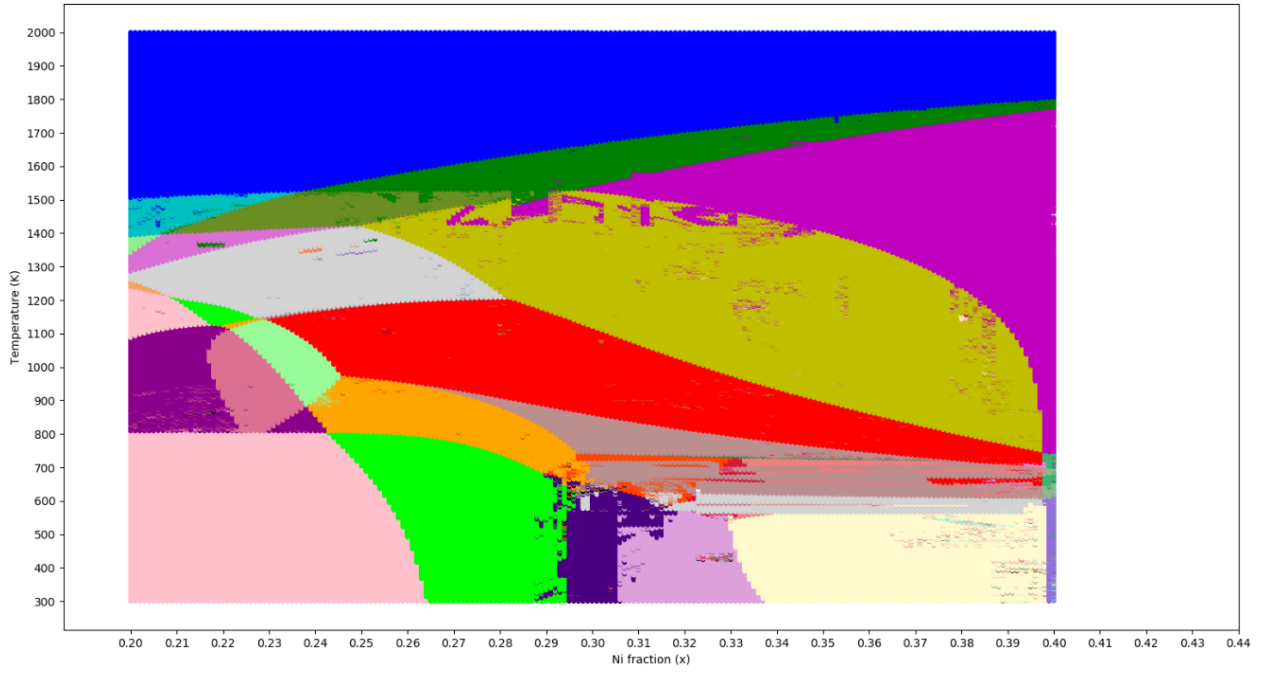
Appendix C: Raw Output

The raw plots from the phase diagram construction procedure are given below. This is the output of the Python plotting code without any intervention. It should be noted that the element fraction shown is the unsimplified mole fraction. For example, in the Ni system, for $x=0.35$ this corresponds to the following composition

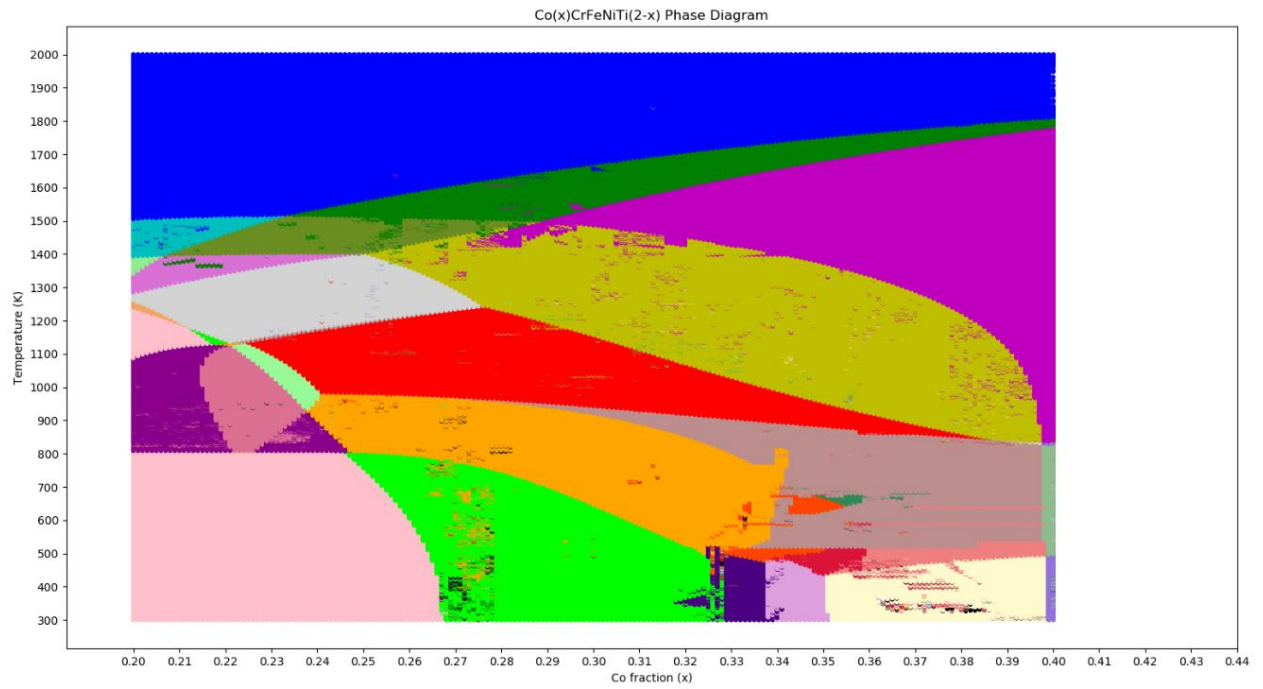
Element	Co	Cr	Fe	Ni	Ti
at.%	20	20	20	35	5

Which corresponds to the $\text{CoCrFeNi}_{1.75}\text{Ti}_{0.25}$ alloy when simplified. The axes in the phase diagrams have been adjusted to reflect the simplified element concentrations.

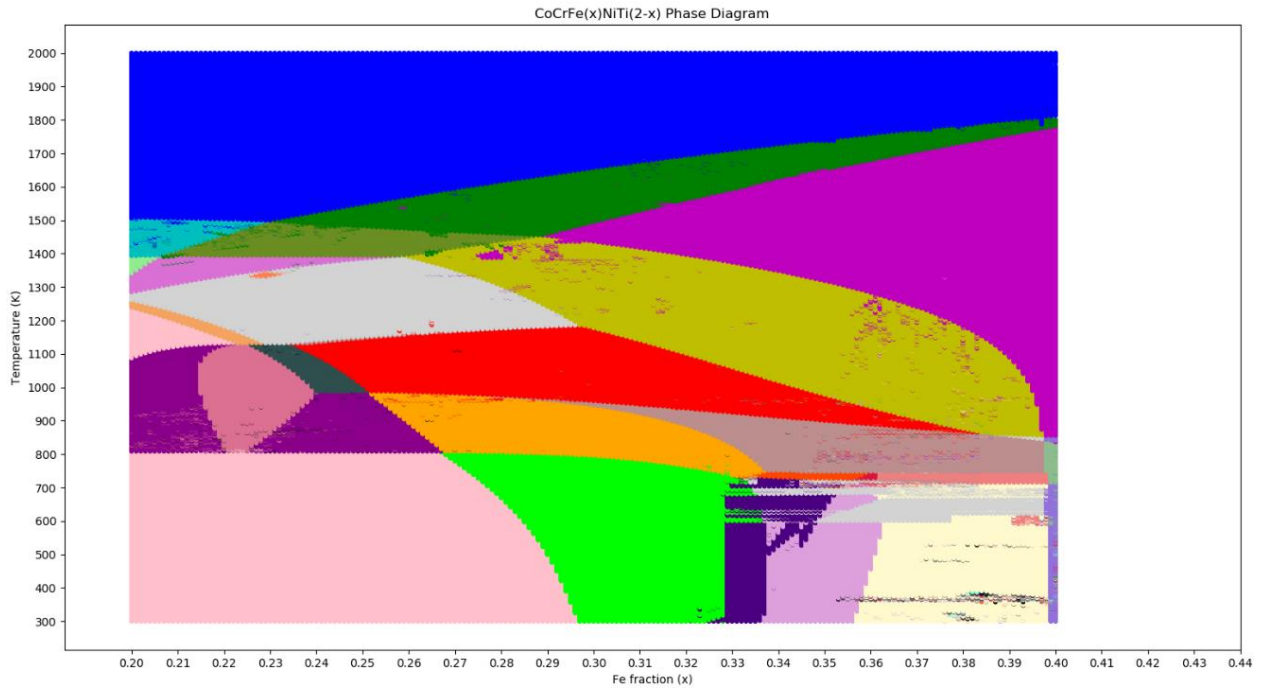
CoCrFeNi_xTi_{2-x}



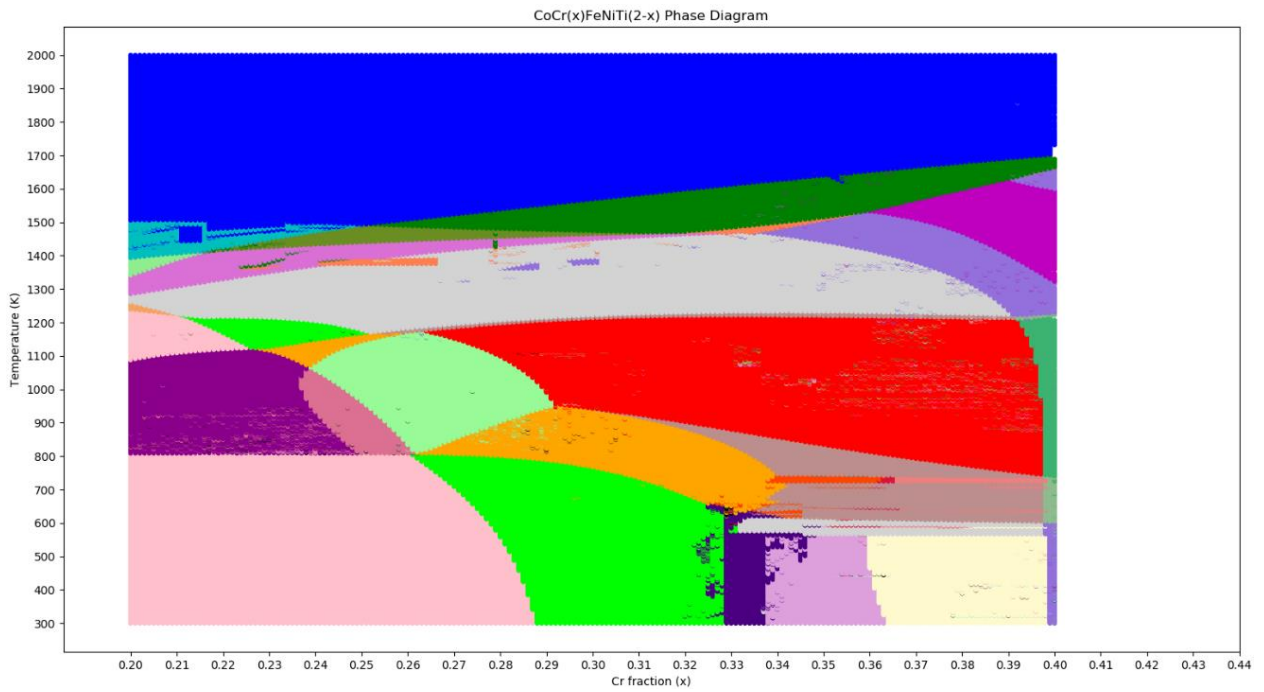
Co_xCrFeNiTi_{2-x}



CoCrFe_xNiTi_{2-x}



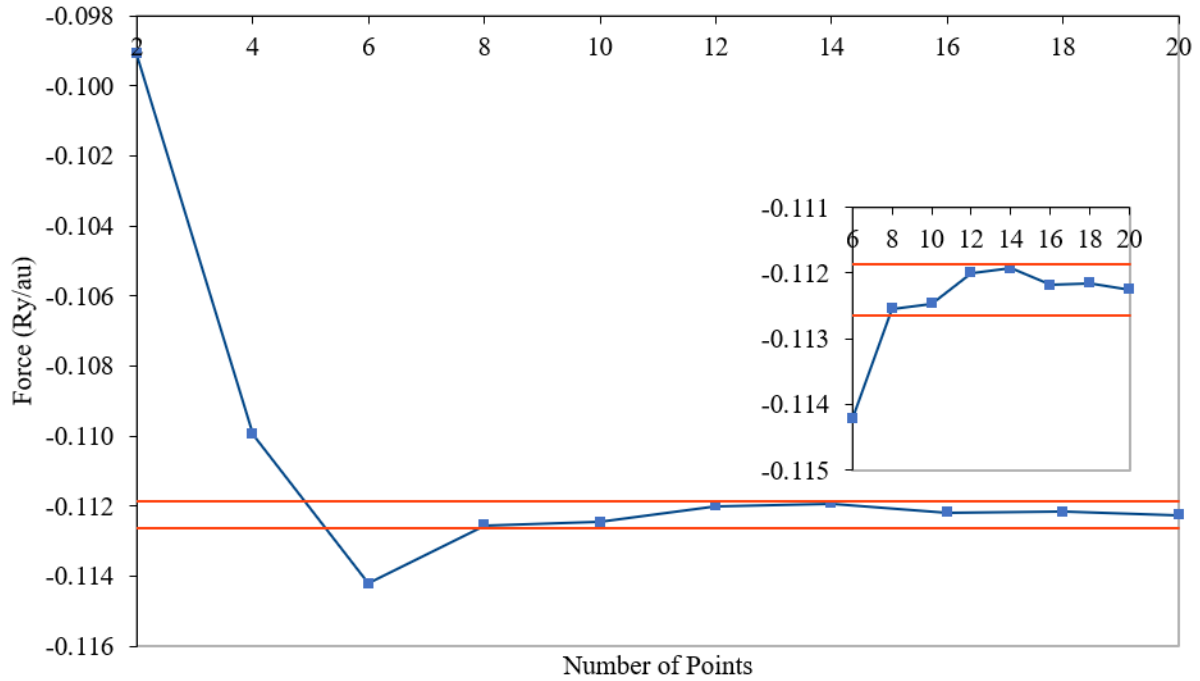
CoCr_xFeNiTi_{2-x}



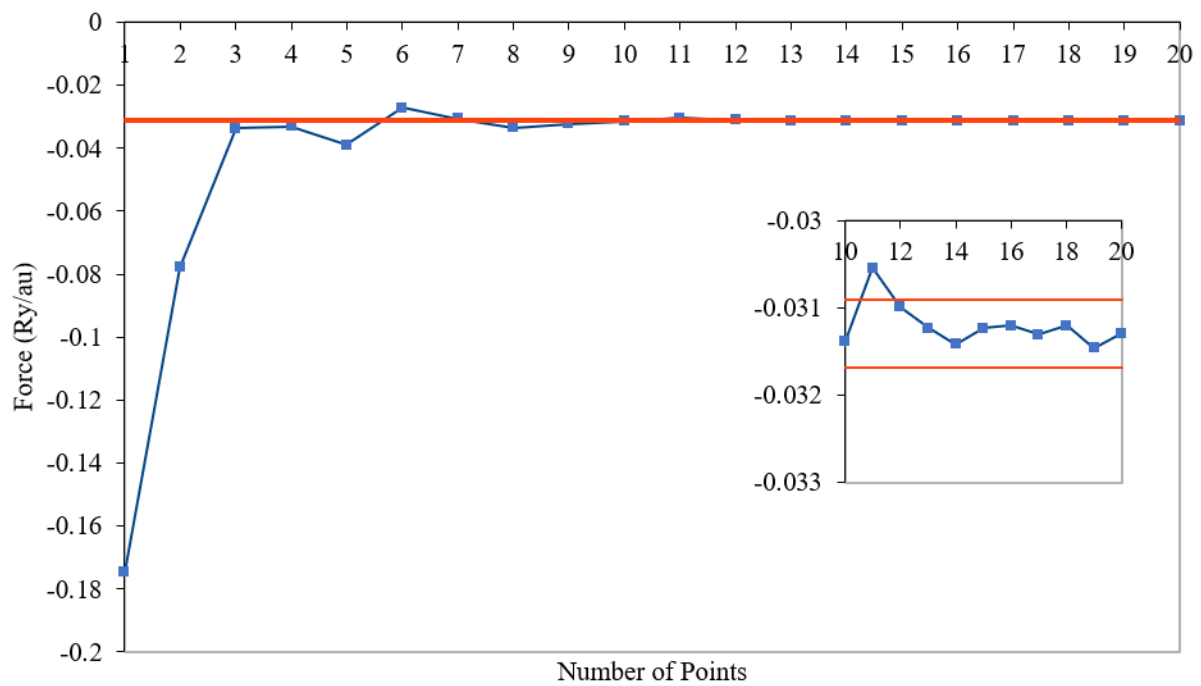
Appendix D: Density Functional Theory Data

K-mesh convergence

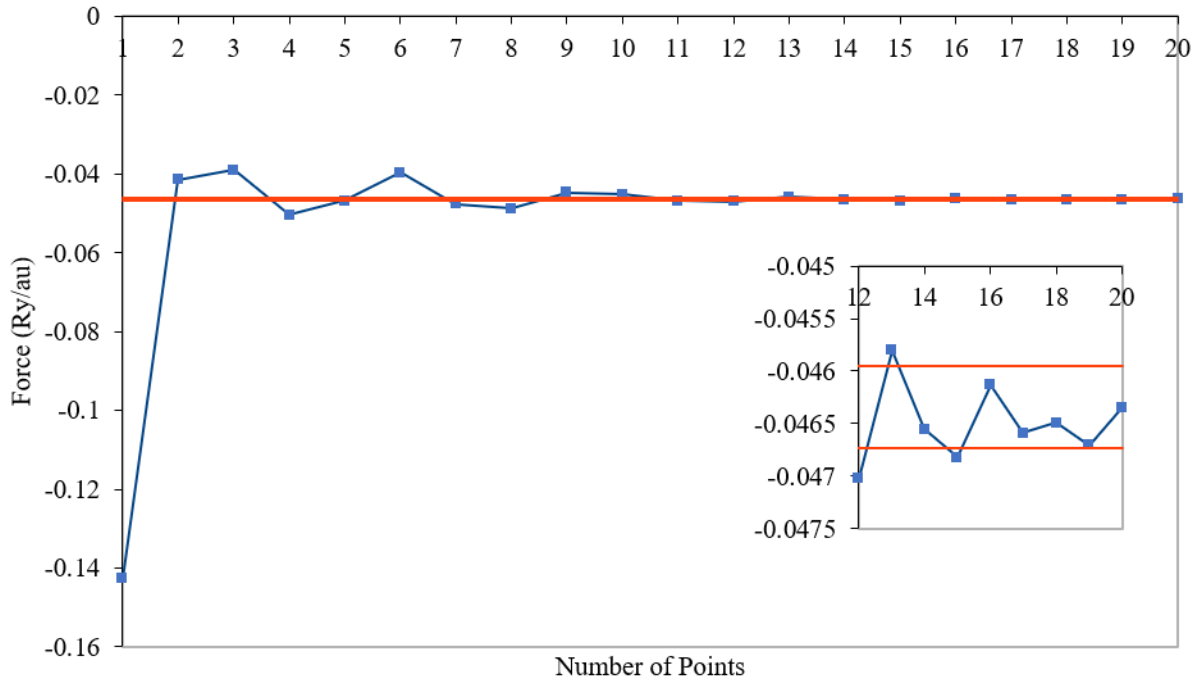
Co - Force vs. k-Point Mesh



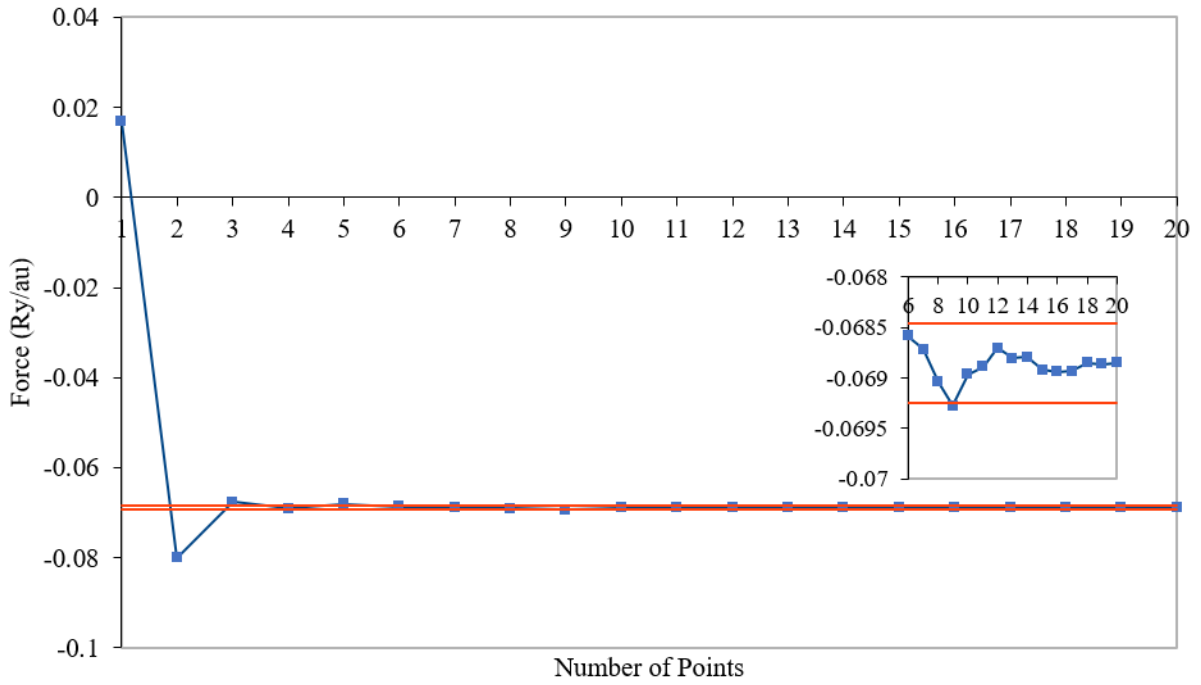
Cr Force vs. k-Point Mesh



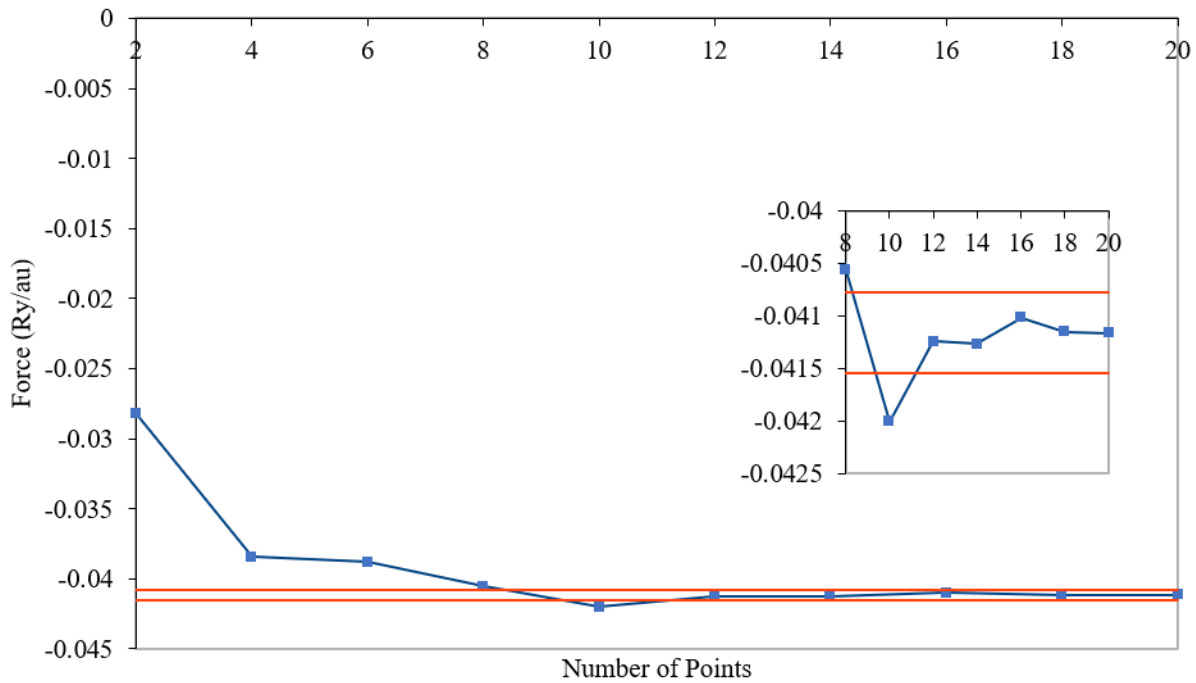
Fe Force vs. k-Point Mesh



Ni - Force vs. k-Point Mesh



Ti - Force vs. k-Point Mesh



CoCrFeNi_{1.75}Ti_{0.25} Special Quasirandom Structure (SQS)

The CoCrFeNi_{1.75}Ti_{0.25} face-centered cubic (FCC) SQS generated using the *mcsqs* code in the Alloy Theoretic Automated Toolkit (ATAT) is provided below. The SQS lattice vectors, unscaled lattice parameters, and the atomic positions and their occupation are presented. This structure was used as the input for the density functional theory (DFT) relaxation, to get the relaxed cell parameters of the CoCrFeNi_{1.75}Ti_{0.25} for use in subsequent property calculations. For the DFT relaxation, the structure was scaled using an initial guess for the lattice constant of 3.6 Å. The final lattice parameters and atomic positions of the relaxed SQS are also provided.

Generated CoCrFeNi_{1.75}Ti_{0.25} SQS (Unrelaxed Structure)

Lattice Vectors	1 0 0				
	0 1 1				
	0 0 1				
Lattice Parameters	5 0 0				
	0 2 0				
	0 0 2				
Atomic Positions	(5.0, 2.0, 2.0) Co	(4.0, 1.0, 2.0) Cr	(2.0, 2.0, 2.0) Fe	(1.0, 2.0, 2.0) Ni	(3.5, 0.5, 2.0) Ni
	(4.0, 2.0, 2.0) Co	(2.0, 2.0, 1.0) Cr	(5.0, 1.0, 2.0) Fe	(1.0, 1.0, 2.0) Ni	(4.5, 0.5, 2.0) Ni
	(5.0, 2.0, 1.0) Co	(4.0, 1.0, 1.0) Cr	(3.0, 0.5, 1.5) Fe	(2.0, 1.0, 2.0) Ni	(1.5, 1.5, 2.0) Ni
	(1.0, 2.0, 1.0) Co	(5.0, 0.5, 0.5) Cr	(4.0, 0.5, 1.5) Fe	(3.0, 1.0, 2.0) Ni	(4.5, 1.5, 2.0) Ni
	(5.0, 1.0, 1.0) Co	(2.0, 0.5, 0.5) Cr	(2.0, 1.5, 1.5) Fe	(3.0, 2.0, 1.0) Ni	(3.5, 1.5, 1.0) Ni
	(2.0, 1.0, 1.0) Co	(5.0, 1.5, 0.5) Cr	(3.0, 1.5, 1.5) Fe	(1.0, 1.0, 1.0) Ni	(4.5, 1.5, 1.0) Ni
	(3.0, 1.0, 1.0) Co	(2.0, 0.5, 1.5) Cr	(0.5, 0.5, 2.0) Fe	(1.0, 0.5, 0.5) Ni	(2.5, 2.0, 0.5) Ni
	(1.0, 1.5, 1.5) Co	(5.0, 1.5, 1.5) Cr	(2.5, 1.5, 2.0) Fe	(3.0, 0.5, 0.5) Ni	(0.5, 1.0, 0.5) Ni
	(4.0, 1.5, 1.5) Co	(0.5, 1.5, 2.0) Cr	(0.5, 0.5, 1.0) Fe	(4.0, 0.5, 0.5) Ni	(4.5, 1.0, 0.5) Ni
	(2.5, 0.5, 2.0) Co	(3.5, 1.5, 2.0) Cr	(1.5, 0.5, 1.0) Fe	(1.0, 1.5, 0.5) Ni	(1.5, 1.0, 1.5) Ni
	(0.5, 1.5, 1.0) Co	(2.5, 0.5, 1.0) Cr	(2.5, 1.5, 1.0) Fe	(2.0, 1.5, 0.5) Ni	(2.5, 1.0, 1.5) Ni
	(1.5, 1.5, 1.0) Co	(4.5, 0.5, 1.0) Cr	(0.5, 2.0, 0.5) Fe	(3.0, 1.5, 0.5) Ni	(3.5, 1.0, 1.5) Ni
	(3.5, 2.0, 0.5) Co	(1.5, 1.0, 0.5) Cr	(4.5, 2.0, 0.5) Fe	(4.0, 1.5, 0.5) Ni	(3.0, 2.0, 2.0) Ti
	(2.5, 1.0, 0.5) Co	(3.5, 1.0, 0.5) Cr	(1.5, 2.0, 1.5) Fe	(5.0, 0.5, 1.5) Ni	(4.0, 2.0, 1.0) Ti
	(3.5, 2.0, 1.5) Co	(0.5, 2.0, 1.5) Cr	(2.5, 2.0, 1.5) Fe	(1.0, 0.5, 1.5) Ni	(3.5, 0.5, 1.0) Ti
	(0.5, 1.0, 1.5) Co	(4.5, 2.0, 1.5) Cr	(4.5, 1.0, 1.5) Fe	(1.5, 0.5, 2.0) Ni	(1.5, 2.0, 0.5) Ti

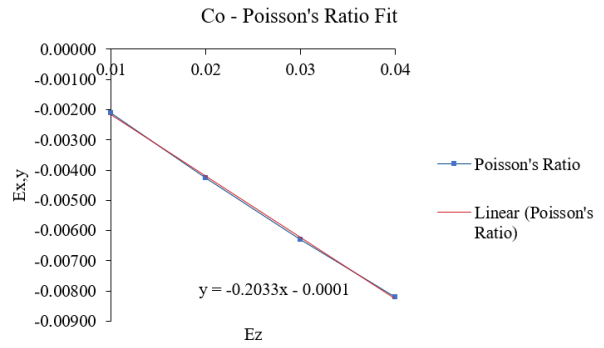
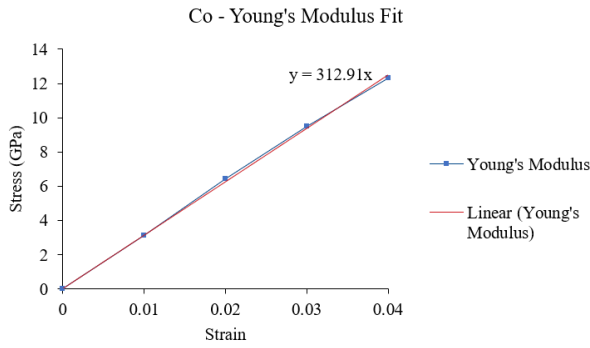
Relaxed Structure of the CoCrFeNi_{1.75}Ti_{0.25} SQS

Final Cell Parameters (Å)											
17.96764	0.00000	0.00000									
0.00000	7.15251	0.00000									
0.00000	0.00000	7.07706									
Final Atom Positions (fractional)											
Co	1.00339	0.99631	0.99835	Fe	0.10125	0.24955	0.99867	Ti	0.59664	1.01025	1.00535
Co	0.79895	1.00227	0.99910	Fe	0.49689	0.74396	1.00315	Ti	0.80169	0.97711	0.50114
Co	0.99975	1.00007	0.50468	Fe	0.09989	0.24747	0.50322	Ti	0.69364	0.25802	0.49215
Co	0.19920	0.99878	0.50481	Fe	0.29673	0.25907	0.50394	Ti	0.29436	0.99340	0.24039
Co	1.00438	0.49104	0.49816	Fe	0.49737	0.74867	0.49524				
Co	0.39993	0.49676	0.50245	Fe	0.10138	0.99365	0.25751				
Co	0.59597	0.50623	0.50364	Fe	0.90543	1.00147	0.24007				
Co	0.19941	0.74635	0.74612	Fe	0.29865	1.00177	0.74901				
Co	0.80248	0.74349	0.76003	Fe	0.49594	1.00642	0.73695				
Co	0.49487	0.26115	0.99587	Fe	0.90055	0.49880	0.74358				
Co	0.09854	0.75054	0.50570	Ni	0.19723	1.00065	0.99549				
Co	0.29775	0.74448	0.50566	Ni	0.19982	0.49760	0.99953				
Co	0.70152	0.99341	0.24492	Ni	0.39636	0.50277	1.00432				
Co	0.50068	0.50251	0.25079	Ni	0.59776	0.50703	0.99760				
Co	0.70086	1.00522	0.75104	Ni	0.60005	0.99960	0.49715				
Co	0.09939	0.50161	0.75232	Ni	0.19722	0.50035	0.50159				
Cr	0.80661	0.49132	0.99358	Ni	0.19836	0.25395	0.25114				
Cr	0.39825	0.99526	0.50422	Ni	0.59650	0.26052	0.24676				
Cr	0.80205	0.51217	0.50549	Ni	0.80235	0.24821	0.25299				
Cr	1.00497	0.24947	0.24238	Ni	0.19856	0.74344	0.25150				
Cr	0.40466	0.25094	0.25388	Ni	0.39845	0.74777	0.25244				
Cr	1.00155	0.75110	0.25095	Ni	0.59896	0.75151	0.24996				
Cr	0.39742	0.26019	0.75758	Ni	0.80427	0.74713	0.24373				
Cr	0.99911	0.73939	0.74575	Ni	1.00121	0.24925	0.75075				
Cr	0.10211	0.74895	0.99255	Ni	0.19908	0.24958	0.74979				
Cr	0.70531	0.74724	0.99801	Ni	0.30032	0.25083	1.00314				
Cr	0.50459	0.25817	0.50057	Ni	0.70172	0.25132	1.00470				
Cr	0.90331	0.25407	0.50139	Ni	0.90383	0.24758	0.99875				
Cr	0.29960	0.49660	0.25979	Ni	0.29791	0.74735	0.99497				
Cr	0.69997	0.51496	0.23474	Ni	0.90214	0.74691	0.99949				
Cr	0.09989	0.99643	0.74503	Ni	0.69956	0.74610	0.50115				
Cr	0.90478	0.99998	0.76517	Ni	0.90371	0.74653	0.49863				
Fe	0.40402	0.99824	0.98985	Ni	0.49726	1.00085	0.25315				
Fe	0.99974	0.50101	0.99992	Ni	0.09986	0.50197	0.24909				
Fe	0.59656	0.26149	0.75492	Ni	0.90134	0.49414	0.25274				
Fe	0.80108	0.25222	0.75762	Ni	0.29731	0.49859	0.74861				
Fe	0.39580	0.74293	0.75036	Ni	0.49788	0.50566	0.75084				
Fe	0.60132	0.75073	0.74632	Ni	0.70080	0.50013	0.75590				

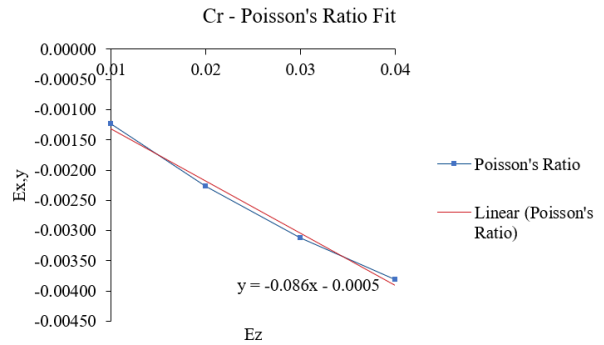
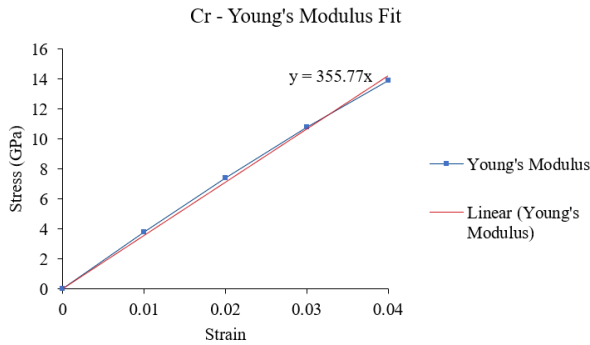
Young's Modulus and Poisson's Ratio Calculation from Computational Stress-Strain Curves

The Young's modulus of a given element was calculated as the slope of a straight line fit to the linear portion of its respective stress-strain curve. For the Poisson's ratio, the lateral strain was computed from the output of the DFT calculation corresponding to a given strain value. A straight line was also fit to a plot of the lateral and longitudinal strain and the Poisson's ratio was calculated as its slope.

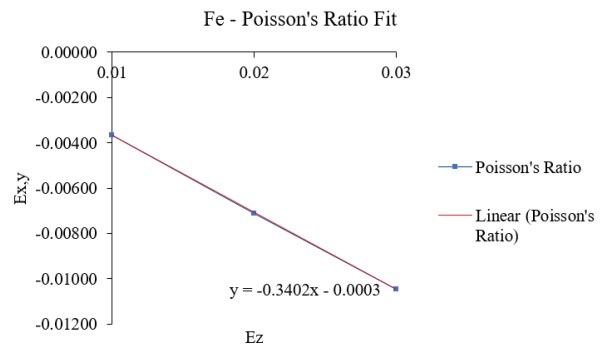
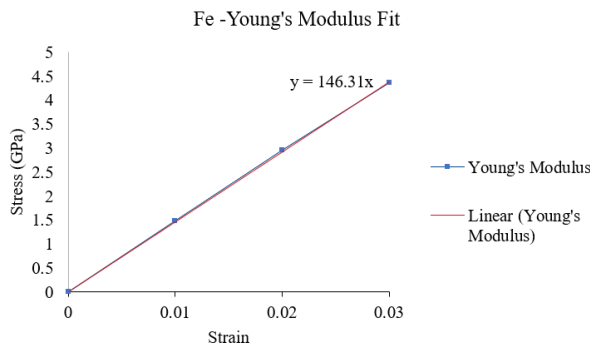
Co



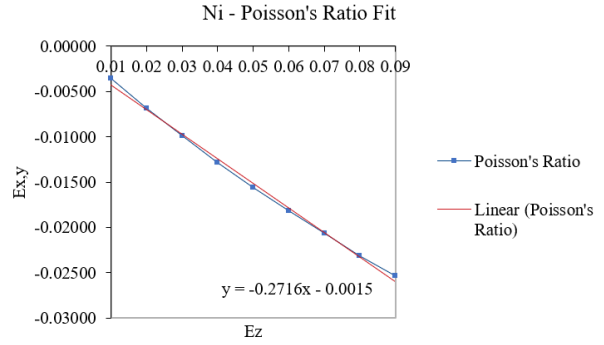
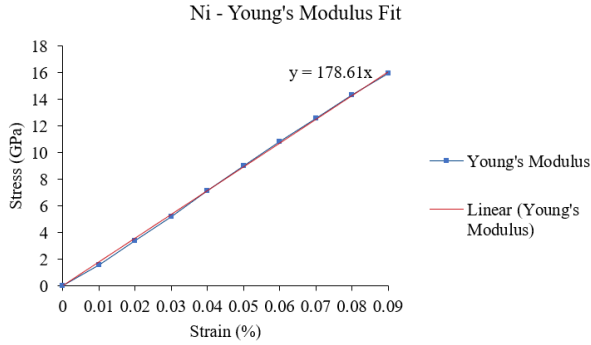
Cr



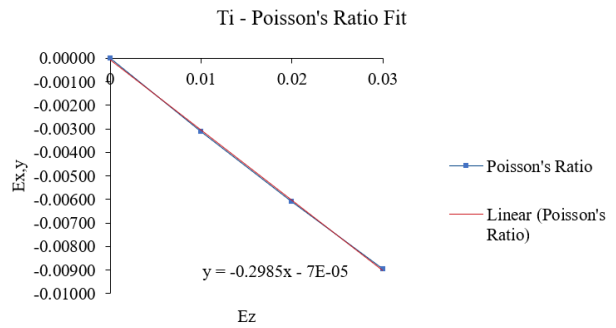
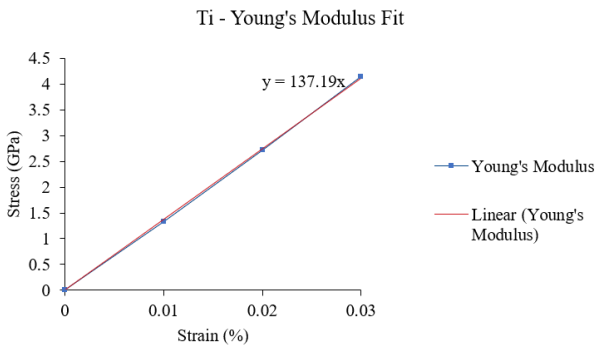
Fe



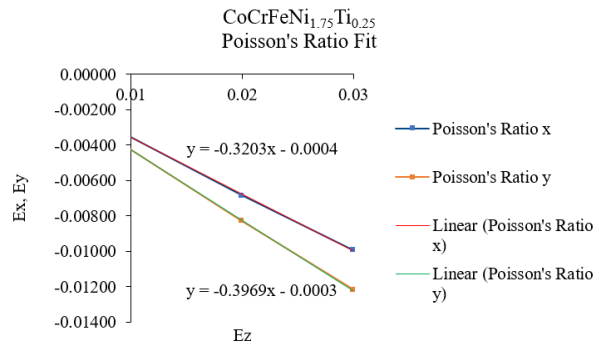
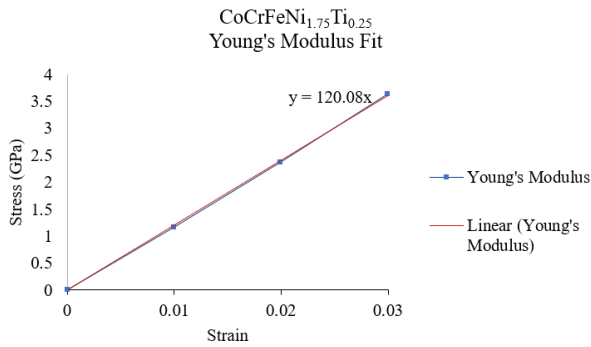
Ni



Ti



CoCrFeNi_{1.75}Ti_{0.25} SQS



For the CoCrFeNi_{1.75}Ti_{0.25} SQS stress-strain calculations, the strains along the x and y directions were found to be unequal. Two values were therefore calculated for the Poisson's ratio and the arithmetic mean of both is reported for the SQS Poisson's ratio.

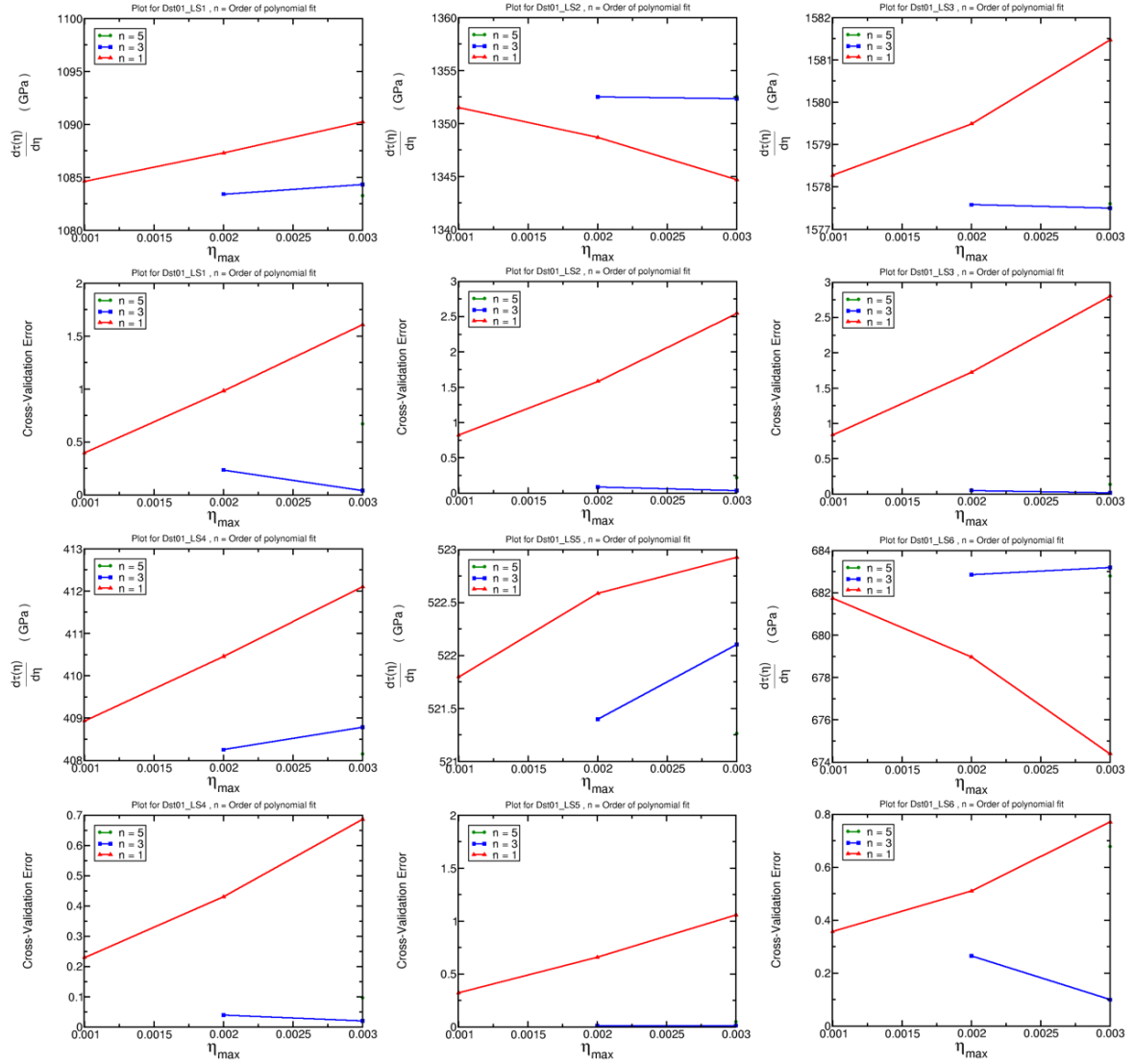
Elastic Constant Analysis

Elemental Study

The ElaStic Package was used for the elastic constant analysis. As explained in Chapter 4, the stress approach was utilized. After the necessary deformations are generated and run using the QUANTUM ESPRESSO (QE) package, the analysis can be carried out using scripts available with downloaded package. The first script used is the *ElaStic_Analyze* script which generates the plots provided below from which η_{\max} and the order of fit can be determined for the *ElaStic_Result* script can be used to calculate the bulk, shear, and Young's modulus in addition to the Poisson's ratio of the desired system. The η_{\max} and the order of fit used for Co, Cr, Fe, Ni, and Ti are summarized in the following table.

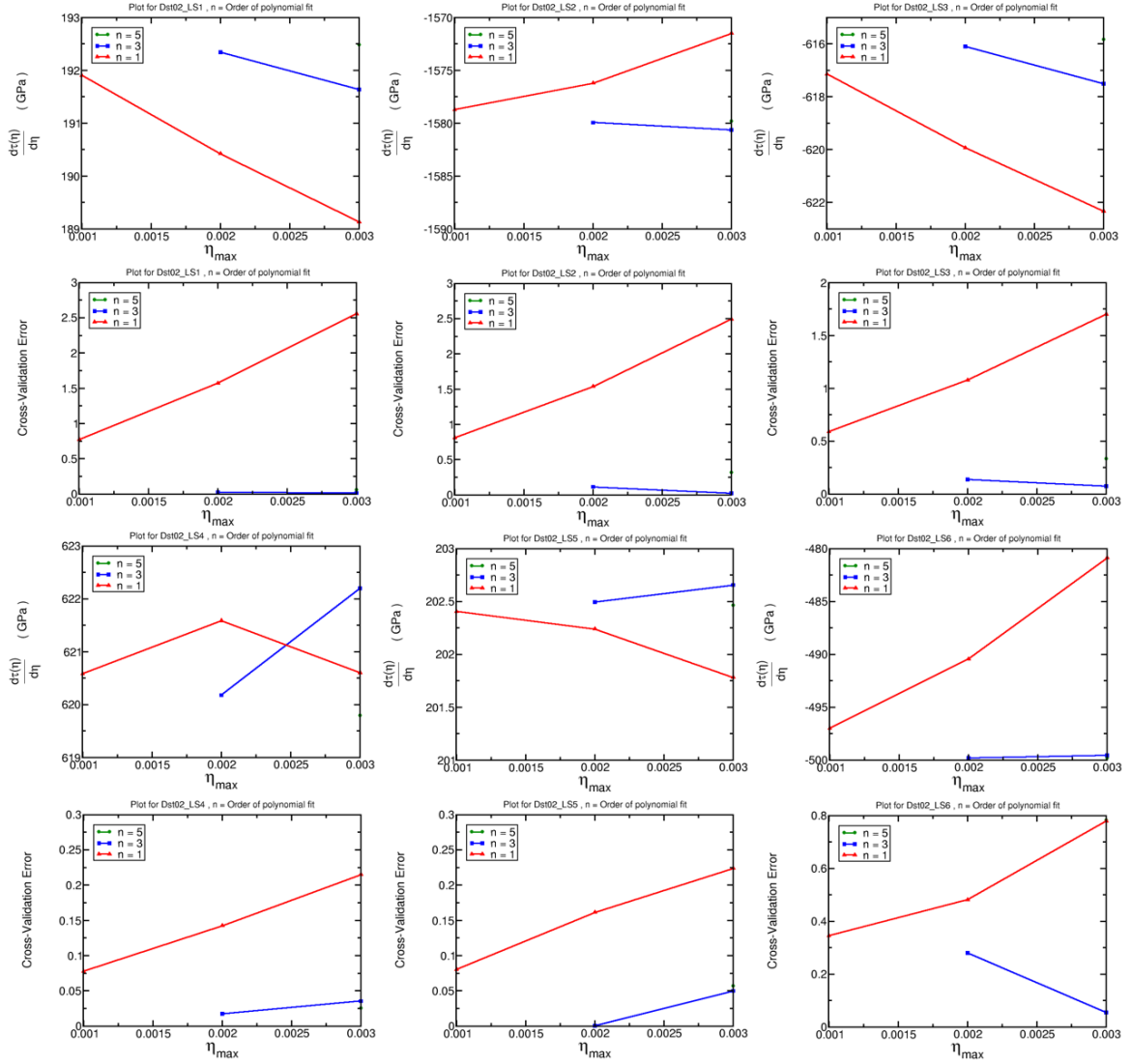
	Co		Cr		Fe		Ni		Ti	
	η_{\max}	fit								
Dst01_01	0.003	3	0.002	3	0.003	3	0.003	3	0.002	3
Dst01_02	0.003	3	0.002	3	0.003	3	0.003	3	0.002	3
Dst01_03	0.003	3	0.002	3	0.002	3	0.003	3	0.003	3
Dst01_04	0.003	3	0.003	3	0.002	3	0.003	3	0.003	3
Dst01_05	0.003	3	0.003	3	0.002	3	0.003	3	0.002	3
Dst01_06	0.003	3	0.002	3	0.003	3	0.003	3	0.002	3
Dst02_01	0.003	3	-	-	-	-	-	-	0.002	3
Dst02_02	0.003	3	-	-	-	-	-	-	0.002	3
Dst02_03	0.003	3	-	-	-	-	-	-	0.003	3
Dst02_04	0.002	3	-	-	-	-	-	-	0.002	3
Dst02_05	0.002	3	-	-	-	-	-	-	0.003	3
Dst02_06	0.003	3	-	-	-	-	-	-	0.002	3

C6



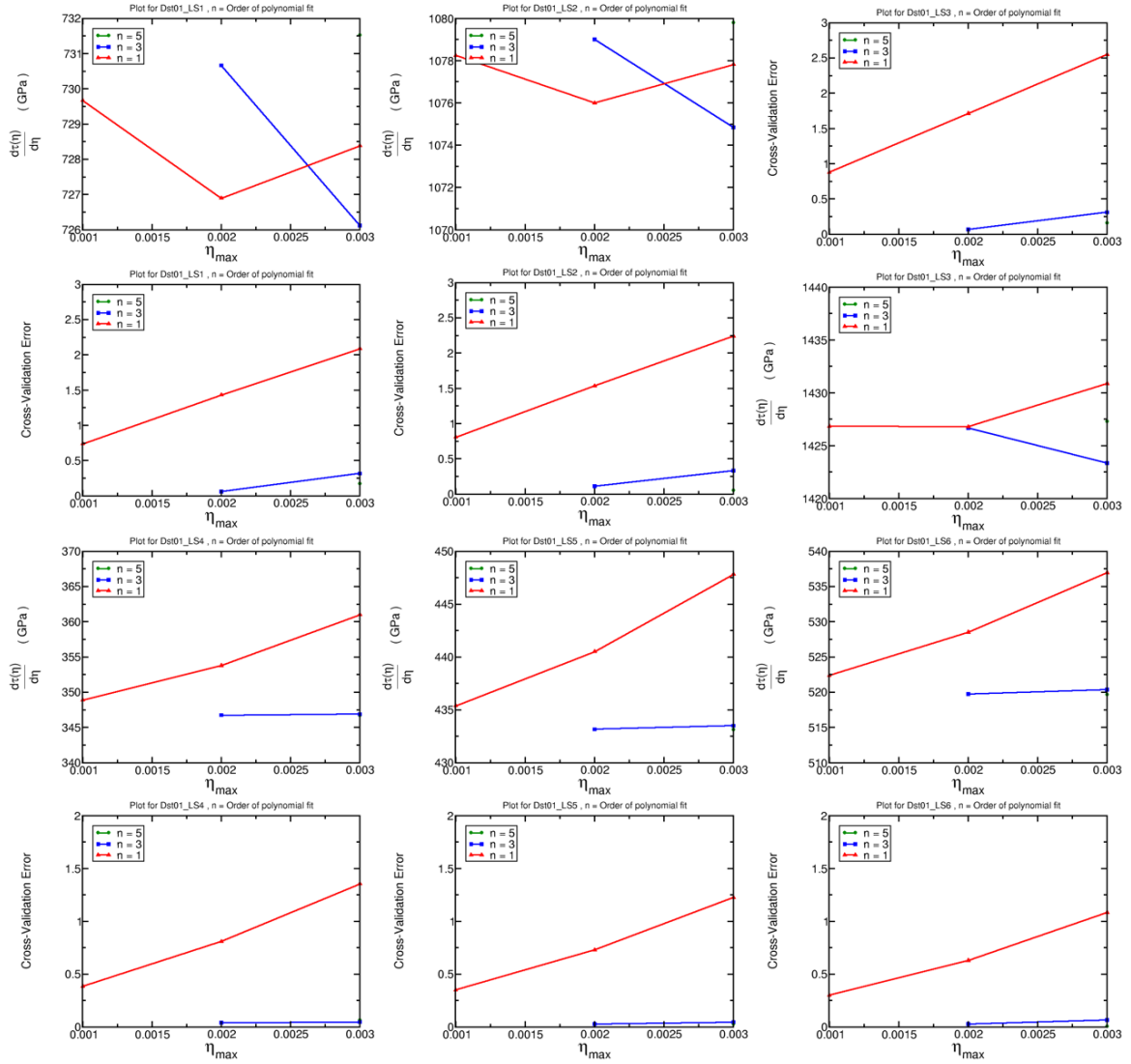
D9

C6

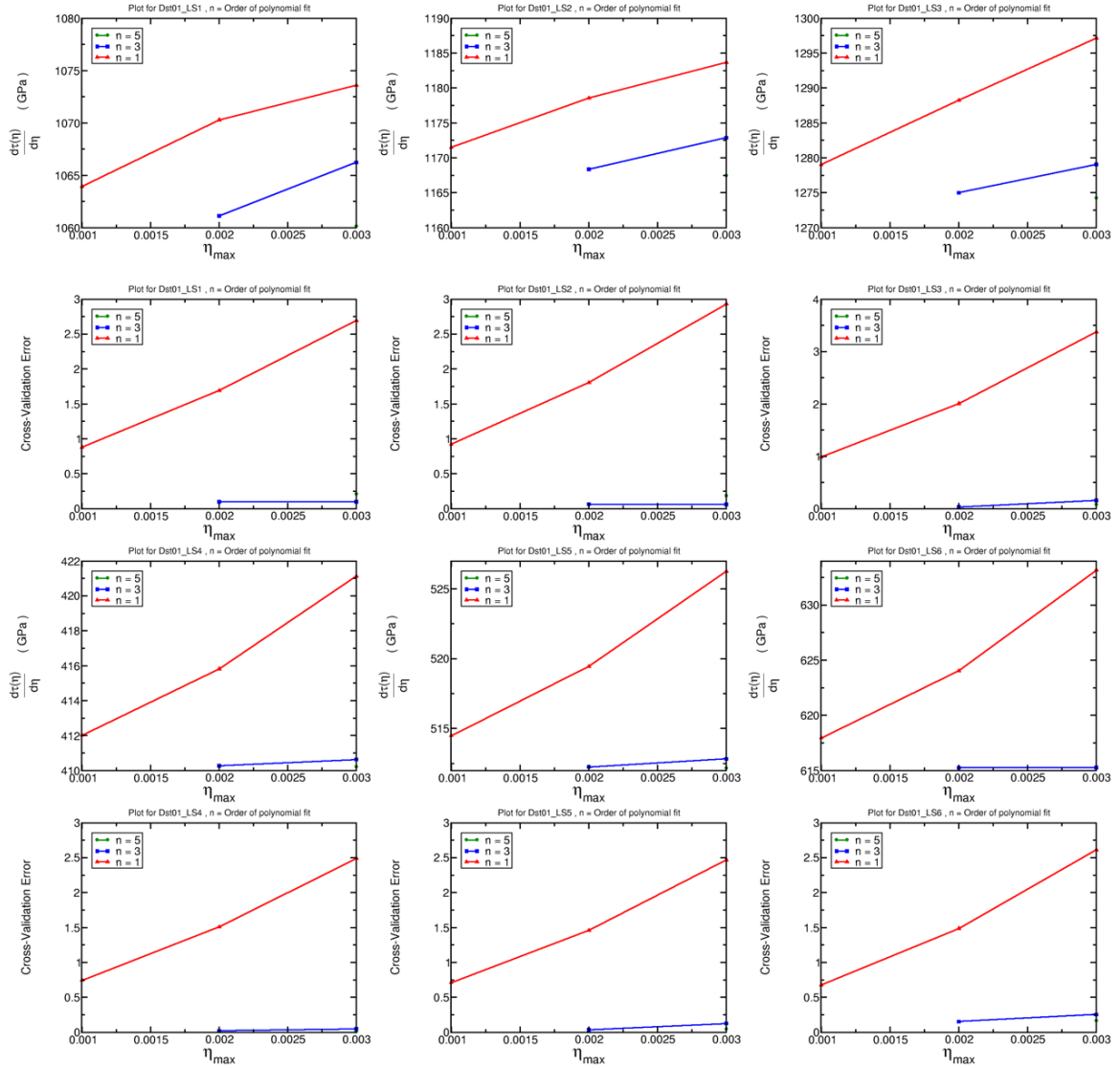


D10

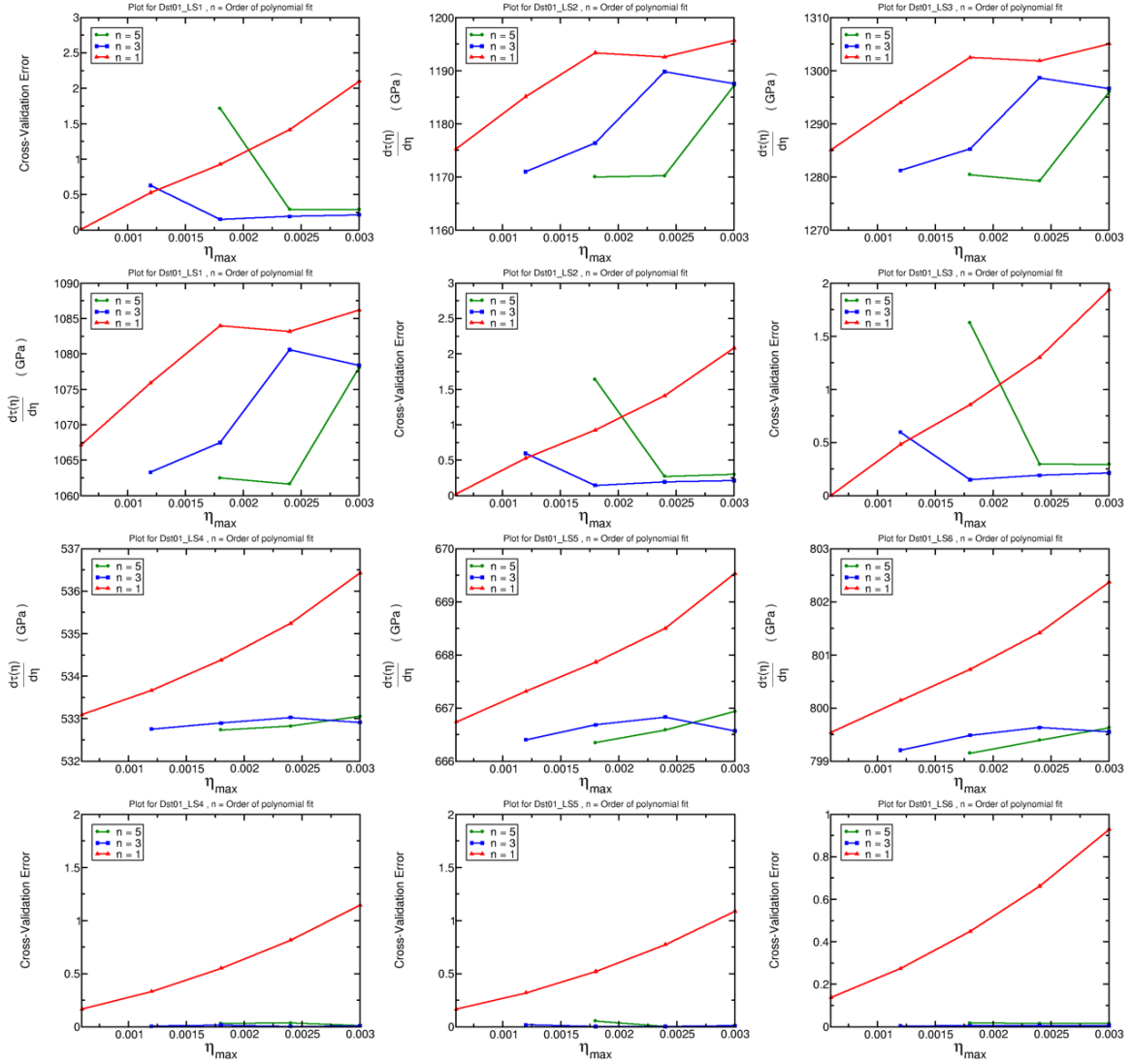
Cr



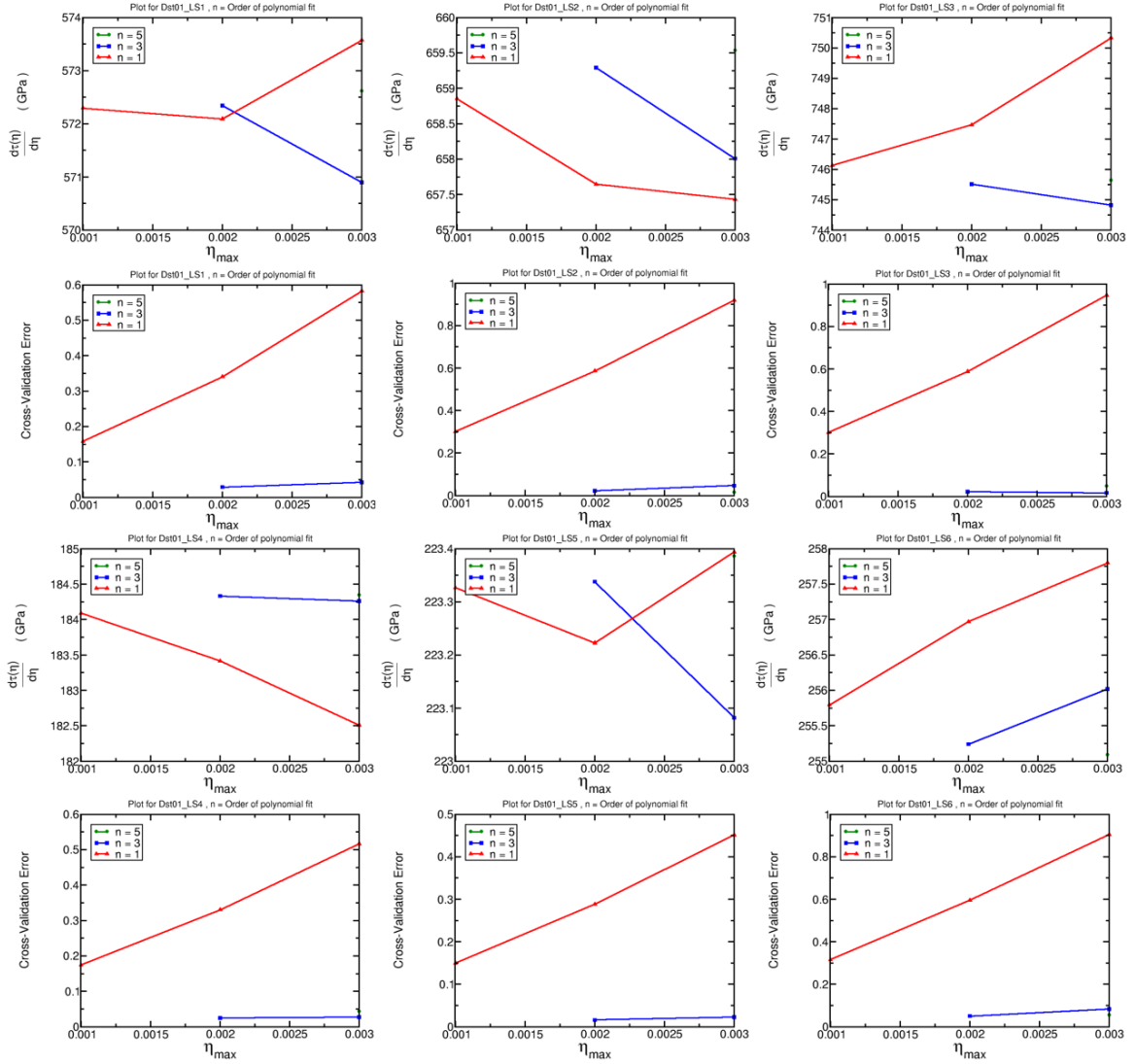
Fe



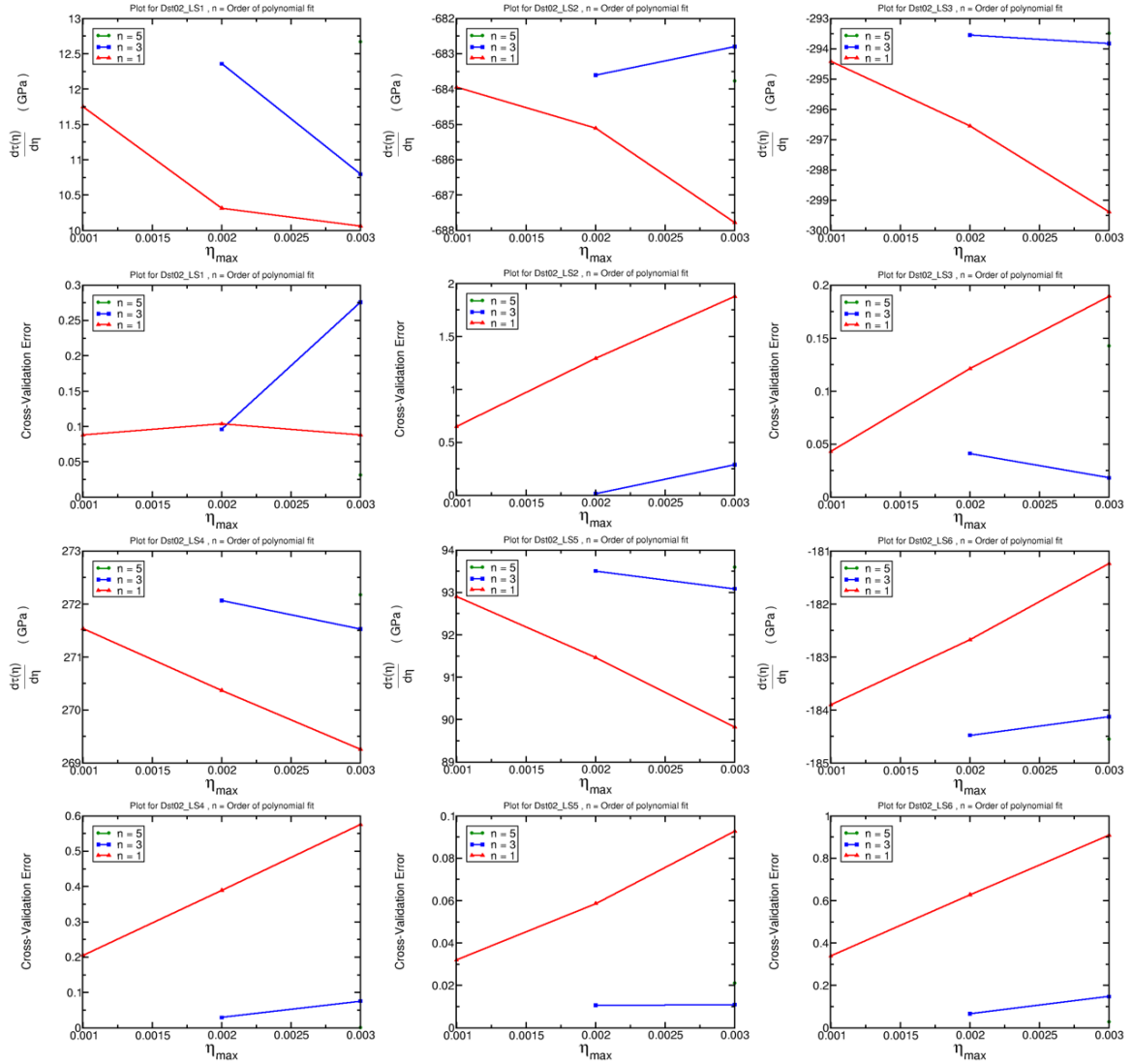
Ni



Ti



Ti



Element Elastic Constants

The second order elastic constants of Co, Cr, Fe, Ni, Ti calculated using the ElaStic package are shown in the table below. The experimental (EXP) values of the SOECs obtained from Nelson et al². are also included.

Element	c11		c12		c44		c13		c33	
	DFT	Exp	DFT	Exp	DFT	Exp	DFT	Exp	DFT	Exp
Co	410	295	184	159	103.4	71	107.5	111	416.8	335
Cr	411.8	348	63.8	67	86.7	100	-	-	-	-
Fe	264.8	230	160.4	135	102.5	117	-	-	-	-
Ni	267.6	249	158.8	152	133.3	124	-	-	-	-
Ti	183.9	160	96.7	90	45.3	46.5	62.8	66	183.7	181

CoCrFeNi_{1.75}Ti_{0.25} Elastic Constants

c11	c12	c13	c14	c15	c16
c12	c22	c23	c24	c25	c26
c13	c23	c33	c34	c35	c36
c14	c24	c34	c44	c45	c46
c15	c25	c35	c45	c55	c56
c16	c26	c36	c46	c56	c66
220.0	121.4	134.5	-4.3	0.2	-0.7
121.4	215.6	138.7	2.4	-1.2	0.8
134.5	138.7	222.3	2.5	2.5	-3.6
-4.3	2.4	2.5	125.2	2.0	-0.4
0.2	-1.2	2.5	2.0	124.2	2.0
-0.7	0.8	-3.6	-0.4	2.0	120.4

² D. F. Nelson, Ed., *Second and Higher Order Elastic Constants*, vol. 29a. Berlin/Heidelberg: Springer-Verlag, 1992.

Absolute discrepancies between calculated elastic constants and properties and experimental values

The absolute differences (in %) between the DFT calculated mechanical properties of Co, Cr, Fe, Ni, and Ti and their experimental values are summarized in the tables below.

(i) Properties from stress-strain data

Element	Property	Discrepancy (%)
Co	Young's Modulus (GPa)	48
	Poisson's Ratio	38
Cr	Young's Modulus (GPa)	44
	Poisson's Ratio	57
Fe	Young's Modulus (GPa)	30
	Poisson's Ratio	17
Ni	Young's Modulus (GPa)	14
	Poisson's Ratio	13
Ti	Young's Modulus (GPa)	31
	Poisson's Ratio	12

(ii) Properties from elastic constants analysis

Element	Property	Discrepancy (%)
Co	Bulk Modulus (GPa)	21
	Shear Modulus (GPa)	44
	Young's Modulus (GPa)	43
	Poisson's Ratio	13
Cr	Bulk Modulus (GPa)	12
	Shear Modulus (GPa)	5
	Young's Modulus (GPa)	15
	Poisson's Ratio	14
Fe	Bulk Modulus (GPa)	20
	Shear Modulus (GPa)	3
	Young's Modulus (GPa)	1
	Poisson's Ratio	10
Ni	Bulk Modulus (GPa)	9
	Shear Modulus (GPa)	22
	Young's Modulus (GPa)	16
	Poisson's Ratio	6
Ti	Bulk Modulus (GPa)	4
	Shear Modulus (GPa)	11
	Young's Modulus (GPa)	20
	Poisson's Ratio	9

(iii) Elastic constants

Element	c11	c12	c44	c13	c33
	Disc. (%)	Disc. (%)	Disc. (%)	Disc. (%)	Disc. (%)
Co	39	16	46	3	24
Cr	18	5	13	-	-
Fe	15	19	12	-	-
Ni	7	4	8	-	-
Ti	15	7	3	5	1